

COMPARISON OF REINFORCED CONCRETE BEAMS AND COR-TUF
BEAMS UNDER IMPACT LOADING

By

DANIEL A. KOCH

A THESIS PRESENTED TO THE GRADUATE SCHOOL
OF THE UNIVERSITY OF FLORIDA IN PARTIAL FULFILLMENT
OF THE REQUIREMENTS FOR THE DEGREE OF
MASTER OF ENGINEERING

UNIVERSITY OF FLORIDA

2012

© 2012 DANIEL A. KOCH

To my loving and supportive family and my always supportive girlfriend

ACKNOWLEDGMENTS

First and foremost, I want to thank my thesis advisor, Dr. Theodor Krauthammer, for all of his invaluable assistance and guidance. I would also like to thank my thesis committee member, Dr. Serdar Astarlioglu for all of his help with the Dynamic Structural Analysis Suite (DSAS) software and writing critiques. Additionally, I want to thank Dr. Long Hoang Bui for his assistance with the finite element software and material models. Furthermore, I would like to acknowledge the sponsors of my work, the Defense Threat Reduction Agency (DTRA) as well as the Engineering Research Development Center (ERDC) for their patience and work to create the test beams for this research. Finally, I would like to acknowledge the support and help of all of my family, friends, peers at the Center for Infrastructure Protection and Physical Security (CIPPS) and my girlfriend, I could not have made it through this lengthy process without you.

TABLE OF CONTENTS

	<u>page</u>
ACKNOWLEDGMENTS.....	4
LIST OF TABLES.....	8
LIST OF FIGURES.....	10
LIST OF ABBREVIATIONS.....	15
ABSTRACT.....	18
CHAPTER	
1 PROBLEM STATEMENT.....	20
1.1 Introduction.....	20
1.2 Objective and Scope.....	23
1.3 Research Significance.....	23
2 BACKGROUND AND LITERATURE REVIEW.....	25
2.1 Introduction.....	25
2.2 Material Background.....	26
2.3 Mix Properties.....	27
2.3.1 Silica Fume.....	27
2.3.2 Superplasticizer.....	28
2.3.3 Fibers.....	29
2.3.4 Cor-Tuf Material Description.....	31
2.3.5 Specimen Preparation and Curing.....	32
2.3.6 Processing, Curing and Preparation of Cor-Tuf.....	33
2.4 Static Strength.....	34
2.4.1 Cor-Tuf Compressive Strength.....	35
2.4.2 Cor-Tuf Tensile Strength.....	37
2.5 Dynamic Testing.....	38
2.5.1 Strain Rate Effects in Ultra High Performance Fiber Reinforced Concrete (UHPFRC).....	38
2.5.2 Split Hopkinson Pressure Bar.....	40
2.5.3 Blast Testing.....	41
2.5.4 Static and Impact Testing of Reinforced Concrete.....	42
2.5.4.1 Static testing of reinforced concrete.....	42
2.5.4.2 Impact testing of reinforced concrete.....	42
2.5.5 Impact Testing of UHPFRC.....	44
2.6 Numerical Simulations.....	47
2.6.1 Finite Element Analysis.....	47
2.6.2 Abaqus Finite Element Analysis Software.....	48

2.6.3	Dynamic Structural Analysis Suite.....	49
3	EXPERIMENTAL INVESTIGATION	83
3.1	Introduction	83
3.2	Test Specimens	83
3.2.1	Cylinders For Static Tests	83
3.2.2	Cylinders For Dynamic Tests	84
3.2.3	Beams For Static and Impact Testing.....	84
3.3	Testing Equipment and Setup.....	85
3.3.1	Static Testing Equipment For Cylinders	85
3.3.2	Static Testing Equipment For Beams	85
3.3.3	Dynamic Testing Equipment For Cylinders	86
3.3.4	Dynamic Testing Equipment For Beams	87
3.4	Instrumentation	87
4	MODEL VALIDATION.....	98
4.1	Introduction	98
4.2	Material Models	98
4.2.1	Modified Hognestad Parabola	99
4.2.2	Hsu Tension Model.....	101
4.2.3	Park and Paulay Steel Model	102
4.3	Abaqus Parameters	104
4.3.1	Concrete Damage Plasticity Model.....	104
4.3.2	Elements	108
4.3.2.1	Element dimensions.....	110
4.3.2.2	Hourglass controls	110
4.3.2.3	Distortion control	111
4.3.3	Model Formulation.....	112
4.3.3.1	Wire parts and embedment.....	112
4.3.3.2	Boundary conditions for supports.....	113
4.3.3.3	Additional constraints	114
4.4	Beam 1-f Model Validation Results	115
4.5	Beam 1-h Model Validation Results	116
5	NUMERICAL PREDICTIONS AND PRELIMINARY TEST RESULTS.....	129
5.1	Introduction	129
5.2	Cor-Tuf Material Model	129
5.3	Static Test Predictions and Test Results	129
5.3.1	B1F.....	129
5.3.2	B2A.....	130
5.3.3	B3F.....	131
5.3.4	B4F.....	131
5.3.5	B5F.....	132
5.3.6	B6F.....	133

5.4 Dynamic Beam Predictions.....	134
5.4.1 Cylinder and Contact Properties.....	134
5.4.2 Gravity.....	135
5.4.3 Hammer Mass and Height.....	135
5.4.4 Predictions.....	136
6 CONCLUSIONS and recommendations.....	157
6.1 Model Validation.....	157
6.2 Static Test Predictions.....	157
6.2.1 B1F.....	157
6.2.2 B2A.....	158
6.2.3 B3F.....	158
6.2.4 B4F.....	159
6.2.5 B5F.....	159
6.2.6 B6F.....	159
6.3 Dynamic Test Predictions.....	160
6.4 Recommendations.....	160
LIST OF REFERENCES.....	162
BIOGRAPHICAL SKETCH.....	166

LIST OF TABLES

<u>Table</u>	<u>page</u>
2-1	Composition of CEMTECmultiscale..... 51
2-2	Composition of compact reinforced concrete (CRC) 52
2-3	Compressive strength (MPa) values with varying percentages of silica fume 53
2-4	Shrinkage for concrete with varying percentages of silica fume 53
2-5	Peak load and fracture energy for cellulose fiber split cylinder tests 53
2-6	Mix proportions for Cor-Tuf concrete 54
2-7	Physical and composition properties of Cor-Tuf2 55
2-8	Unconfined compressive strength for Cor-Tuf cylinders 56
2-9	Mechanical properties of ultra-high performance cement based composite (UHPCC) 56
2-10	Slab reinforcement and charge description 57
2-11	Deflections for slabs subject to blast 57
2-12	Properties of steel in Feldman and Siess beams..... 58
2-13	Concrete properties for Feldman and Siess beams..... 59
2-14	Results for the Habel and Gauvreau drop hammer tests..... 60
2-15	Reactive powder concrete (RPC) mix proportions..... 60
3-1	6" x 12" cylinder quantities and material properties for static testing 89
3-2	4" x 8" cylinder quantities and material properties for static testing 89
3-3	4" x 8" cylinder quantities and material properties for impact testing 89
3-4	6" x 12" cylinder quantities and material properties for impact testing 89
3-5	Beam quantities and materials for static and impact testing..... 89
3-6	Static and impact testing matrix per material..... 90
3-7	Center for Infrastructure Protection and Physical Security (CIPPS) Drop Hammer Specifications..... 90

4-1	Abaqus default concrete damage plasticity parameters	118
4-2	Dynamic increase factors for Dynamic Structural Analysis Suite (DSAS) runs based on strain rate	118
5-1	Summary of Test Results and Numerical Predictions for static beams	137

LIST OF FIGURES

<u>Figure</u>	<u>page</u>
2-1 Early age shrinkage in concrete with varying levels of superplasticizer.....	61
2-2 Compressive strength curve with the addition of fibers	61
2-3 Tensile strength curve with the addition of fibers.....	62
2-4 Impact performance of normal-strength polymer macro-FRC (PFRC)	62
2-5 Impact performance of normal-strength steel FRC (SFRC).....	63
2-6 Fiber protrusion from cracked beam.....	63
2-7 Dramix ZP305 Fiber	64
2-8 Bending tensile stress versus deflection for heat treated and water cured concrete.....	64
2-9 Typical ultra-high performance fiber reinforced concrete (UHPFRC) strength characteristics.....	65
2-10 (a) Three-point bending test setup; (b) Four-point bending test setup.....	65
2-11 Three-point bending results	66
2-12 Four-point bending results	66
2-13 UHPFRC moment-curvature relationship	67
2-14 Triaxial pressure vessel.....	67
2-15 Stress-strain for unconfined compression (UC) test of Cor-Tuf1	68
2-16 Stress-strain for UC test of Cor-Tuf2	68
2-17 Triaxial compression (TXC) test results with confining pressures of 10MPa to 300 MPa (Cor-Tuf1).....	69
2-18 TXC test results with confining pressures of 10MPa to 300 MPa (Cor-Tuf2).....	69
2-19 Stress path from direct pull tests for Cor-Tuf1	70
2-20 Stress path from direct pull tests for Cor-Tuf2	70
2-21 Block-bar device diagram	71

2-22	Modulus of Rupture-stress rate diagram	71
2-23	Uniaxial tensile stress vs. stress rate.....	72
2-24	Dynamic increase factor (DIF) vs. strain rate.....	72
2-25	Stress-strain diagrams for split-hopkinson pressure bar (SHPB) tests with varying fiber percentages	73
2-26	SHPB specimens post-test.....	73
2-27	Reinforcement geometry for blast slabs	74
2-28	Cracking in NRC-3 slab (top); Cracking in UHPFC slab (bottom).....	74
2-29	Feldman and Siess reinforced concrete beam design, front view.....	75
2-30	Feldman and Siess beam 1-f and 1-h, section view	75
2-31	Load vs. Midspan Displacement for Feldman and Siess static tests.	76
2-32	Load time-history for Feldman and Siess Beam 1-f.....	77
2-33	Load-beam system for single degree of freedom (SDOF) calculations	77
2-34	Displacement vs. time for impact of Beam 1H.....	78
2-35	Habel and Gauvreau drop hammer setup	79
2-36	Two mass-spring model	79
2-37	(a) Drop weight force vs. time; (b) Deflection vs. time	80
2-38	Fujikake et al. reactive powder concrete (RPC) beam cross section.....	80
2-39	Fujikake et al. drop hammer test setup	81
2-40	(a) Fujikake et al. drop hammer test from 0.8 m; (b) Drop from 1.2 m.....	81
2-41	Flow process for a physical problem solved with finite element analysis.....	82
3-1	Beam dimensions and details for series B1, B3 and B4 (Table 3-5).....	91
3-2	Beam dimensions and details for series B2 and B6 (Table 3-5).....	92
3-3	Beam dimensions and details for series B5 (Table 3-5)	93
3-4	Gilson MC-250CS Compression Testing Machine	94
3-5	Enerpac RC-5013 hydraulic jack for static testing	94

3-6	Center for Infrastructure Protection Physical Security (CIPPS) Drop Hammer...	95
3-7	CIPPS Data Acquisition System	96
3-8	Supports for beam testing	97
4-1	Concrete compressive stress-strain curves for different compressive strengths.....	119
4-2	Modified Hognestad stress-strain curve for concrete in compression.....	119
4-3	Modified Hognestad curve for Abaqus, $f'_c = 6150$ psi.....	120
4-4	Tensile strength curve of reinforce concrete.....	120
4-5	Modified Hsu tensile curve for Abaqus	121
4-6	Strain hardening material model for steel reinforcement	121
4-7	Uniaxial stress-strain curve for compression in concrete damage plasticity model.....	122
4-8	Tension stress-strain curve in concrete damage plasticity model.....	122
4-9	First order linear 8 node brick element	123
4-10	Example of support conditions for Feldman and Sesis beam 1-h.....	123
4-11	Top node constraint for applying load to Feldman and Siess beams	124
4-12	Beam 1-f Numerical vs. Experimental Results.....	124
4-13	Plot of the plastic strains in deformed Beam 1f.....	125
4-14	Digitized vs. approximated load curves for beam 1-h	126
4-15	Beam 1-h DSAS parametric analysis with DIF	126
4-16	Parametric study of varying strain rates for beam 1-h in Abaqus	127
4-17	Numerical vs. experimental results for beam 1-h.....	127
4-18	Beam 1-h Abaqus deformed plot with plastic strain.....	128
5-1	Material properties for Abaqus runs.....	138
5-2	Pre-test picture of B1F resting on the supports	138
5-3	Mid-test picture of B1F loaded to 27 kips	139

5-4	B1F at failure, a typical compression rebar failure.....	139
5-5	Predicted vs. Experimental Results for B1F NSC Static Test.....	140
5-6	B2A pre-test.....	140
5-7	B2A with 10 kips of load	141
5-8	B2A at failure, due to shear	141
5-9	B2A Predictions vs. Experimental Results.....	142
5-10	B3F pre-test.....	142
5-11	B3F loaded to 35 kips.....	143
5-12	B3F crack at 40 kips	143
5-13	B3F at failure, tension rebar failure.....	144
5-14	B3F Predictions vs. Experimental Results.....	144
5-15	B4F pre-test.....	145
5-16	B4F at 37 kips.....	145
5-17	B4F loaded to 40 kips.....	146
5-18	B4F loaded to failure, buckling of compression rebar.....	146
5-19	B4F Predictions vs. Experimental Results.....	147
5-20	B5F Pre-Test.....	147
5-21	B5F loaded to 20 kips.....	148
5-22	B5F tension failure.....	148
5-23	B5F tension crack at failure	149
5-24	B5F Predictions vs. Experimental Results.....	149
5-25	B6F Pre-Test.....	150
5-26	B6F loaded to 45 kips.....	150
5-27	B6F loaded to 47 kips.....	151
5-28	B6F failure, full tension failure	151

5-29	B6F Predictions vs. Experimental Results	152
5-30	Dynamic beam representation in Abaqus	152
5-31	B1 Numerical impact midspan displacement vs. time results	153
5-32	B2 Numerical impact midspan displacement vs. time results	153
5-33	B3 Numerical impact midspan displacement vs. time results	154
5-34	B4 Numerical impact midspan displacement vs. time results	154
5-35	B5 Numerical impact midspan displacement vs. time results	155
5-36	B6 Numerical impact midspan displacement vs. time results	155
5-37	Load vs. time for hammer impact from 10 ft with 600 lbs	156

LIST OF ABBREVIATIONS

$d\epsilon/dt$	Strain rate
E_c	Elastic modulus, defined by ACI 318 (2011)
E_{cd}	Descending elastic modulus ACI 318 (2011)
E_0	Elastic Young's modulus
E_s	Modulus of elasticity for the steel
f_c	Concrete compressive stress
f_c''	Maximum concrete compressive stress
f_c'	Uniaxial concrete compressive strength under standard test cylinder
f_{cr}	Cracking stress of plain concrete in psi
f_s	Compressive stress at a point on the curve
f_u	Ultimate stress
f_y	Yield strength of the steel
L	Length of the beam
m	Variable of the equation
M_e	Mass concentrated at midspan, equal to 0.971 lb-sec ² per inch for the beams
m_p	Concentrated plate mass
\bar{m}	Mass per unit length of the specimen
n	Distance from the end of the beam to a point of interest
P	Load applied to a beam
pl	Weight of the beam

Q_y	Yield resistance of SDOF system
r	Variable of the equation
$R_p(u_p)$	equivalent static force-deflection response of plates
$R_D(u_{DW} - u_p)$	Force-displacement relationship of plywood
T	Period of natural vibration for a beam
w_c	Density of the concrete in lb/ft ³
Δ_c	Displacement at the center of the beam
Δ_n	Displacement at a specific distance n from the end of the beam
Δ_y	Yield deflection of the SDOF system
$\dot{\Delta}_n$	Velocity at a point n distance from the end of a beam
$\dot{\Delta}_c$	Velocity at the center of the beam
ϵ_c	Total compressive concrete strain
ϵ_{cr}	Cracking strain
ϵ_0	Concrete strain at maximum compressive stress
ϵ_{oc}^{el}	Elastic compressive strain
ϵ_s	Strain at a point on the curve
ϵ_{sh}	Strain when strain hardening begins
ϵ_{su}	Ultimate strain
ϵ_t	Total strain
ϵ_{ot}^{el}	Elastic strain
u_{DW}	Displacement of the drop weight

u_p	Displacement of the plate
σ_c	Concrete compressive stress
σ_t	Concrete tensile stress
σ_{to}	Tensile failure/cracking stress

Abstract of Thesis Presented to the Graduate School
of the University of Florida in Partial Fulfillment of the
Requirements for the Degree of Master of Engineering

COMPARISON OF REINFORCED CONCRETE BEAMS AND COR-TUF BEAMS
UNDER IMPACT LOADING

By

Daniel A. Koch

August 2012

Chair: Theodore Krauthammer
Major: Civil Engineering

Concrete is one of the most widely utilized building materials because of its cost and wide range of applicability. However, as the scale of structures created with concrete has increased dramatically, the need for advanced materials has as well. Ultra high performance concrete (UHPC) is a reactive powder concrete that is denser, stronger and more durable than normal strength concrete (NSC). UHPC is characterized by its use of admixtures, superplasticizers and fibers which help to decrease water content and porosity while increasing durability and ductility. UHPC has superb material characteristics with compressive strengths generally exceeding 150 MPa and tensile strengths reaching up to 20 MPa. Consequently, UHPC has been shown to be far more resilient to dynamic loading than normal strength concrete.

A variety of UHPC mixes have been developed by the commercial and private sectors to fit specific needs. Researchers at the U.S. Army Engineer Research and Development Center (ERDC) developed a UHPC mix entitled Cor-Tuf in two variations, with and without fibers. These mixes have compressive strengths between 190-240 MPa and tensile strengths approaching 8 MPa. As is the case for each new mix

variation, a period of testing and characterization is required to fully understand its properties. The purpose of the research presented in this paper was to explore the dynamic characterization of these Cor-Tuf mixes on the behavior of beams under localized impact. This was accomplished through impact tests performed on cylinders and beams constructed of Cor-Tuf, and comparing the results with identical NSC counterparts. This study was the first to dynamically test full scale UHPC beams and also focuses on the effects of strain rate on Cor-Tuf.

CHAPTER 1 PROBLEM STATEMENT

1.1 Introduction

The evolution of building materials is an ongoing process that began with using mud and straw for building huts. Over time the use of a variety of materials such as wood, stone, brick and normal strength concrete (NSC) helped progress human's structural needs. However, a void existed for some time where larger scale structures were desired. The patent for reinforced concrete (RFC) in 1854 finally helped fill this void, and with it began an explosion in the use of concrete and the scale of structures for which it was used (Tang 2004). Today concrete, and especially reinforced concrete, has become the most utilized building material in the world because of its wide availability, low cost and the limited amount of knowledge necessary for use. Nevertheless, while reinforced concrete helped progress the landscape of modern structures, the nature of the world is to exceed what has already been accomplished; high strength concretes were the next step in the evolution of structural materials.

Beginning in the 1960's and 70's, researchers began looking into reducing the water to cement ratio of concrete to increase strength (Yudenfreud et al. 1972). Their success at reducing the ratio below 0.3 led to the production of high strength concretes (HSC) with compressive strengths between 50 MPa (7.3 ksi) and 120 MPa (17.4 ksi), an improvement over the standard 34.5 MPa (5 ksi) NSC. However, not yet satisfied with the results achieved so far, ultra-high performance concretes (UHPC's) were created, in part forwarded by researchers like Bache (Bache 1987). UHPC is characterized as having compressive strengths exceeding 150 MPa (21.8 ksi) (and capable of reaching 800 MPa (116 ksi)), increased durability, decreased porosity, and

utilizes fibers to improve ductility and strength (Association Française de Génie Civil. (AFGC) 2002). The superior properties of high performance concretes have begun to be incorporated into new structures. An example of this can be seen in the Burj Khalifa located in Dubai, UAE that utilizes a high strength concrete with a compressive strength of 80 MPa (11.6 ksi). Large structures, especially tall buildings, could be attractive targets (e.g. terrorism, etc.) and it is essential to assess the contribution of stronger materials to their survivability.

Ultra High Performance Concrete (UHPC) has emerged as the clear choice to fit the evolving needs of the engineering community. In addition to UHPC's increased compressive strength, it also has been shown to have increased dynamic properties, especially impact resistance (Bindiganavile et al. 2002; Habel and Gauvreau 2008). The drawback to the composition of UHPC mixes are their inherent brittleness. This problem has been addressed through the use of fiber reinforcement, generally either steel or some form of polymer fiber. Testing with fibers has shown vast improvements in the ductility and flexural strength of the UHPC mix when fibers are included (Habel and Gauvreau 2008; Millard et al. 2010). These mixes are referred to as Ultra High Performance Fiber Reinforced Concrete (UHPRFC); however, since all UHPC materials are brittle and thus require fiber reinforcement, UHPC usually refers to concretes with fiber reinforcement.

Protective design in structural engineering has become more prevalent over the last few decades. As incidences of terrorism, military action, and even accidents have increased, so has the need for more versatile structures capable of withstanding these threats. While the motives may vary for these incidences, the consequences generally

remain the same. Between the years of 1993 to 1997, there were more than 8,000 bombings in the US alone, accounting for 101 deaths and 513 injuries with property damage approaching US \$1 Billion (Theodor Krauthammer 2008). While the focus of protective design has been focused on military applications, the attacks on the World Trade Center and Pentagon in 2001 have led to a broader investigation into protective design for civilian structures as well.

The face of the threats facing civilians and structures has drastically changed since WWII. The additional increase in explosive power deliverable by military and even homemade devices complicates the jobs of those analyzing new and existing structures for threats. The need for structures that are capable of withstanding blast and impact both in the United States and abroad is an important realization in the engineering community (Theodor Krauthammer 2008).

Researchers at the US Army Engineer Research and Development Center (ERDC) developed a UHPC (and UHPFRC) mix known as Cor-Tuf. Cor-Tuf has shown similar strength parameters to other UHPC mixes (Williams et al. 2009). The developments at ERDC included 23 mechanical property tests to begin characterizing Cor-Tuf; however, many tests still remain before Cor-Tuf can be properly utilized. While there has been much work performed thus far with UHPFRC and impact testing, each mix design requires its own set of tests as they affect the characteristics of the specimens created from them. The impact performance of Cor-Tuf and structural elements made with Cor-Tuf are of great interest as its mechanical properties have shown its outstanding strength capabilities and show promise for its use in protective design.

1.2 Objective and Scope

The objective of this research is to begin characterizing the dynamics properties of the Cor-Tuf cylinder and beam specimens through impact testing. The process of characterizing the impact capabilities will require modeling, impact testing, and thorough analysis of the test data that is acquired. Additionally, it will be desirable to begin implementing this data into modeling scenarios for later design purposes. To accomplish these goals, the following steps will be taken:

1. Conduct a literature review of related work.
2. Numerical simulations performed with single degree of freedom and multi-degree of freedom analysis software.
3. Impact testing of NSC concrete and Cor-Tuf cylinders as well as reinforced concrete and Cor-Tuf beams using an instrumented drop hammer.
4. Analysis and comparison of the accumulated data to develop the Cor-Tuf constitutive models.
5. Incorporate these models into dynamic structural analysis suite (DSAS).

Due to the large scope of this work, the first two steps will be the focus of the work shown here. In addition, the preliminary results of the static tests that were completed during the writing of this research will be included as well. Future reports will discuss the testing and post-processing of the data from the dynamic testing.

1.3 Research Significance

Before Cor-Tuf can be properly utilized, especially for protective design purposes, the dynamic characteristics of the Cor-Tuf mixes must be investigated. Impact resistance of Cor-Tuf beams is only the first of many dynamic tests that will be performed with Cor-Tuf, but it is one of the most important. The goal of this research is to discover the peak dynamic flexural strength of Cor-Tuf beams. This research will be

an essential stepping stone as well as the future tests including penetration, Split-Bar Hopkinson and blast. Additionally, a comprehensive parametric study of varying drop heights will be necessary if the strain-rate effects in Cor-Tuf are to be understood. Once it has been fully characterized, Cor-Tuf can be effectively utilized both for protection and general construction with confidence.

CHAPTER 2 BACKGROUND AND LITERATURE REVIEW

2.1 Introduction

UHPFRC is a reactive powder concrete (RPC) that is denser, stronger, and more durable than normal strength concrete (NSC) and its predecessor high performance concrete (HPC). UHPFRC is a cementitious material with superb material characteristics with compressive strengths generally exceeding 150 MPa (21.8 ksi) and tensile strengths between 15 and 20 MPa (2.2 and 2.9 ksi) (Association Française de Génie Civil. (AFGC) 2002). Additionally, UHPFRC has shown great resiliency in dynamic loading scenarios as will be seen later on.

UHPFRC is a recent advance in the concrete industry that belongs to the Advanced Cementitious Materials (ACM) category. It is characterized by having a low permeability, higher compressive and tensile strengths, increased impact resistance, high ductility, and increased durability when compared to normal concrete (BA Graybeal 2006; Habel 2004). As explained by Semioli (2001), high performance concretes are those that require nonconventional constituents, mixing, placing, and curing practices. These mixes are generally designed for special applications and environments and they generally meet most, if not all, of the following requirements: ease of placement, compaction without segregation, early-age strength, long term strength, low permeability, high density, toughness, and long life in severe conditions. It is for these reasons that research into UHPFRC is of great interest when pertaining to nuclear containment, infrastructure, high rise structures, and protective design. Many proprietary concrete mixes exist, currently there are several that are being commercially developed: Ductal[®] developed jointly by Lafarge, Bouygues and Rhodia; DENSIT[®] produced by ITW

(Illinois Tool Works Inc.); and CERACEM[®] (formerly BSI – Béton Spécial Industriel) developed by Eiffage. Other UHPFRC mixes exist such as CEMTEC multiscale[®], Cor-Tuf and compact reinforced concrete (CRC), however these are currently not commercially available.

This chapter will provide a thorough background on UHPFRC and its constituents, with a focus on the properties of Cor-Tuf. Additionally, dynamic testing of existing UHPFRC mixes will be presented. Lastly, the experimental tests on which the current testing is based along with the numerical processes that will be utilized for validation and prediction will be presented as well.

2.2 Material Background

The search for a higher performance concrete began long ago, in the 1970's with the work of Brunauer, Odler and Yudenfreud to find high strength pastes that utilize low water to cement ratios below 0.3 (Yudenfreud et al. 1972). Their studies lead to the discovery of concretes with compressive strengths up to 200 MPa. These strength values were further enhanced by Roy in 1972 with the use of hot pressing techniques, which is similar to heat treatment (see Specimen Preparation and Curing), except it also utilizes pressure, to create cement past with compressive strengths approaching 680 MPa.

In the 1980's with the development of superplasticizers and pozzolanic admixtures, new concrete mixes began to emerge with more compact matrices than those found in normal. While these mixes showed improved characteristics, they still had issues with permeability and creep. Bache (1987) developed a way to interact the superplasticizers and silica fume to decrease porosity and increase strength. The final step taken to enhance this new material was to reduce the brittleness, thereby

increasing its ductility and flexural response. This was accomplished through the addition of steel, polymer, or organic fibers. Since the late 1990's, the focus of UHPFRC research has been on fully characterizing its mechanical properties and searching for methods to reduce its production costs (Rong et al. 2010).

2.3 Mix Properties

As mentioned previously, UHPFRC generally consists of cement, sand, silica fume, superplasticizer, water, and fibers. The key to a high performance concrete has shown to be the uniformity of the constituents and its homogeneity. The dense packing of the aggregates accounts for the concrete's increased strength and low porosity. Typically, UHPFRC mixes have a water to cement ratio lower than 0.3 and contain at least 20% silica fume. Fine quartz sand with a 600 μm or smaller diameter has produced some of the best results; however, the use of natural sands has also produced decent results with a greatly reduced cost (Rong et al. 2010). Compositions of two different UHPFRC mixes are provided below. In Table 2-1 is the composition for CEMTEC_{multiscale} and in Table 2-2 is the composition of CRC. The material properties of Cor-Tuf can be found in Table 2-6.

2.3.1 Silica Fume

Silica fume is one of the key ingredients of UHPFRC. It optimizes the particle packing density and increases strength through its reaction with calcium hydroxide (Habel et al. 2006; Millard et al. 2010). Silica fume helps the porosity of the UHPFRC by filling the voids between the cement grains. While the optimum silica fume content appears to be around 25% (Habel 2004), the prohibitive cost of silica fume leads most manufacturers to stay below 15%. Mazloom et al. (2004) carried out experiments testing the effects of varied percentages of silica fume. Their testing showed that the

compressive strength of concrete with 15% silica fume was 21% higher than that of the control concrete at 28 days, as can be seen in Table 2-3 (the percentage of silica fume used is the number to the left of SF in Table 2-3). The concretes containing silica fume also showed lower susceptibility to swell and shrinkage. The total shrinkage values can be seen in Table 2-4. Silica fume also has the added advantage of protecting against chlorides.

2.3.2 Superplasticizer

Superplasticizers play several important roles in ultra-high performance concretes. They attach themselves to aggregate surfaces and improve fluidity by reducing the aggregate interaction (interaction of charges on their surfaces) (Association Française de Génie Civil. (AFGC) 2002). This increased fluidity also helps in early age shrinkage as the constituents can easily slip by each other and self-compact; evidence of this phenomenon can be seen in Figure 2-1. This is one of the main reasons why UHPC mixes are generally referred to as self-compacting as they do not require any external forces.

The small reactive particles (diameter $< 0.5 \mu\text{m}$) that make up the superplasticizers help fill in the tiny voids between the larger particles of cement, silica fume, and sand. The addition of superplasticizers also reduces the necessary amount of water needed to unite the particles in the concrete matrix (Morin et al. 2001). A typical value for superplasticizer is 1.4% weight of cement; however, the content can range between 0 and 2% depending on the mix design (Association Française de Génie Civil. (AFGC) 2002).

2.3.3 Fibers

Concrete is generally considered a very brittle material with poor tensile strength when compared to materials like steel. Reinforced concrete was developed to improve the tensile capabilities of concrete and is now one of the most popular building materials in the world with its use of steel rebars to increase flexural performance. High performance concretes are even more susceptible to brittleness due to their stronger material matrix. Fiber reinforced concrete (FRC) and even UHPC mixes emerged in the 1980's, as is the case with CRC (Bache 1987).

Fibers improve concrete ductility by bridging the microcracks that form as a concrete specimen begins experiencing stresses exceeding the internal tensile capacity of the matrix. The fibers, that generally have hooked, flattened, or crimped ends to ensure they are properly anchored; in the case of steel fibers, they add the tensile strength that is not inherent in the concrete alone. Figure 2-2 and Figure 2-3 from Fehling et al. (2004) illustrate the benefits afforded by adding fibers to concrete. The slope and area of the descending portion of the curve are influenced by fiber percentage, geometry, length, stiffness and orientation.

While steel fibers are the most predominant among both industrial and experimental high performance concretes, other options such as polymer or organic fibers are available. Polymer fibers are still an attractive option due to their low cost of production, especially with varying properties depending on their application. An additional benefit of polymer fibers is their resistance to corrosive chemicals. Bindiganavile and Banthia (2002) compared the impact characteristics of beams that utilized polypropylene or steel fibers. Their testing showed that while the steel fibers showed better performance in quasi-static situations and low stress rate conditions, the

polypropylene outperformed in high stress rate dynamic situations. Figure 2-4 shows the results from each drop height for the polypropylene reinforced concrete (PFRC) and Figure 2-5 shows the results for the steel fiber reinforced concrete (SFRC).

Experimentation with organic fibers has been much more limited than with polymer and steel fibers. Peters (Peters 2009) performed a series of experiments using cellulose fibers (derived from wood) added to the Cor-Tuf mix. The advantages of cellulose fibers are that they have a high elastic modulus (60 GPa), they are hydrophilic, and their small diameter helps them create a tightly packed matrix. The downside of using an organic material such as cellulose fibers is the potential for deterioration. The primary risk to the fibers is the permeability of the concrete leading to chemicals contacting the fibers and causing deterioration. Therefore, UHPC is a good material in which to test these types of environmentally sensitive fibers due to its low permeability.

Table 2-5 shows the peak load and fracture energy (averaged) for 8mm split cylinder tests. The data clearly shows almost a two fold increase in fracture energy for the 3% micro fiber over the baseline sample. While organic fibers offer a reduced production cost, their performance does not yet match that of polymer and steel fiber reinforced concretes.

Fibers are subject to two types of failure: pullout or fracture. While fracture is a possibility in severe loading conditions, pullout is generally the primary mode of fiber failure (Bindiganavile and Banthia 2001a). This is due to the fact that the fiber to cement bond and fiber to cement friction force combined are still weaker than the fiber itself. Evidence that pullout is the failure mode of fibers is clear in Figure 2-6, (Kang et al. 2010). Logically, if the fibers were fracturing, the location of the crack would be cleaner

with fewer fibers protruding from it. The work performed by Bindiganavile and Banthia (2001a; b) reaffirmed that polymer fibers, with the correct geometries, can outperform steel fibers at higher strain rates.

The area of greatest contention regarding fiber reinforcement is fiber orientation, which is difficult to control and hard to predict. While fibers tend to orientate in the direction of flow (Association Française de Génie Civil. (AFGC) 2002), factors like gravity, proximity to the formwork, and contact with any aggregate during the pouring of the mix will have varying effects. The importance of performing multiple strength tests and ensuring quality control of the production of UHPFRC cannot be stressed enough. While careful production techniques can ensure a degree of uniformity among the specimens created, there will still be variance in the fiber orientation and thus the characteristics of each specimen. The need for effective characterization through thorough testing and factors of safety are the only way to ensure that the fiber orientation is accounted for, as is true for the other constituents in the concrete.

2.3.4 Cor-Tuf Material Description

UHPC and UHPFRC concretes are not cost effective due to the sensitive nature of the mixture proportions necessary and the subsequent necessity for materials with impeccable quality control. Cor-Tuf was designed to utilize more local materials than other specialized concretes in an effort to reduce production costs. Cor-Tuf is a UHPC mix designed by GSL, ERDC with compressive strengths ranging from 190 MPa up to 244 MPa (27.6 ksi to 35.4 ksi) (Williams et al. 2009). It is a reactive powder concrete (RPC) with fine aggregates and pozzolanic powders and no coarse aggregates. The maximum particle size of Cor-Tuf, 0.6 mm (0.024 inches), belongs to the foundry grade Ottawa silica sand. Cor-Tuf has a water to cement ratio of 0.21 achieved by using a

polycarboxylate superplasticizer to decrease the need for water and to improve workability. The full mix proportions can be found in Table 2-6 including product descriptions for each constituent.

Cor-Tuf exists in two forms as mixes with and without fibers named Cor-Tuf1 and Cor-Tuf2, respectively. Cor-Tuf1 contains 3.6% steel fibers by volume. The Dramix® ZP305 fibers produced by the Bekaert Corporation measure 30 mm (1.18 in) in length with a diameter of 0.55 mm (0.022 in) and are hooked at each end, as can be seen in Figure 2-7. The tensile strength of these steel fibers, reported by the manufacturer, is 1,100 MPa (159.5 ksi). The fibers come bonded together with a water-soluble adhesive for easy dispersion when added to the Cor-Tuf mix.

2.3.5 Specimen Preparation and Curing

Concrete curing is the period of time in which concrete strengthens. Many methods exist to aid this process including water curing, heat treatment, and pressure treatment. Heat treatment and water curing have become the most popular among UHPFRC methods and heat treatment is the method recommended by the Association Française de Génie Civil (AFGC) (2002). Heat treatment is the process of using heat in conjunction with either high humidity or water submersion to speed up the hydration process. Hydration comprises the chemical processes during which concrete strengthens as the cement and aggregates bond together. Heat treatment has three main effects (Association Française de Génie Civil. (AFGC) 2002): faster strengthening of concrete, delayed shrinkage, creep effects are reduced, and overall durability is improved. When curing Ductal® the specimens are put inside of a steam box for 24 hours at 90 °C; the steam ensures that the relative humidity (RH) does not drop below a critical level.

Rossi et al (2005) carried out tests on the CEMTEC_{multiscale} composite that included a comparison of specimens cured by water curing and heat treatment. The water cure simply required the placing of specimens inside of room temperature water (usually in the range of 20 to 25 °C). In this case, the specimens were kept in the water until they were tested. The heat treatment took place for four days in a drying oven at 90 °C, two days after being removed from their mold. The two days also applies to the water cure as this time is necessary to ensure that the concrete has set into its form. Figure 2-8 illustrates the improvement in strength for heat treated specimens.

2.3.6 Processing, Curing and Preparation of Cor-Tuf

Williams et al (2009) have a strictly controlled regime for the production of Cor-Tuf. A high-shear batch plant with a 1 m³ capacity was used at 60% capacity to mix the concrete. The dry portions of the mix are measured, loaded into the mixer, and blended for five minutes. The water and superplasticizer, which are measured and combined beforehand, are then added to the mixer and mixed for approximately 15 minutes. Mixing time was based on the goal of achieving a flowing paste and varied slightly. In the case of Cor-Tuf1, the fibers were added to the mixer with an additional 10 minutes of mixing time. Cor-Tuf2 was also mixed for an extra ten minutes, at this point, to ensure that both concretes endured the same amount of mix time. A variety of specimens geometries were cast from Cor-Tuf1 and Cor-Tuf2. Their dimensions and unconfined compressive strengths are shown in Table 2-8.

The curing regime for Cor-Tuf was also strictly controlled. After the concrete was poured into the molds, the specimens spent 24 hours in a 22 °C and 100% humidity controlled environment. Subsequently, the specimens were removed from their molds and remained in the open air till the 7-day age. At this point, the specimens were then

inserted in a water bath for four days and kept at a constant 85 °C. The final step after the bath was to dry them in an oven for two days again maintained at 85 °C. The specimens were then removed at a cumulative age of 13 days ready to begin testing.

2.4 Static Strength

As stated previously, UHPFRC has impressive mechanical properties that can exceed those of structural steel. Quasi-static stress-strain curves for compression and tension of typical UHPFRC can be found in Figure 2-9, included in these diagrams are typical results for NC concrete (denoted as NSC).

Habel and Gauvreau (2008) performed three and four-point bending tests on UHPFRC plates. The plates utilized for these tests, and the dynamic tests to be discussed later, measured 600 mm (23.6 in) long, 145 mm (5.7 in.) wide and 50 mm (2.0 in.) thick. The concrete chosen for these tests was the CEMTECmultiscale developed by Rossi et al., for the composition see Table 2-1. No special heat or pressure treatments were utilized, only moist curing at 23 °C. The concrete cylinders from this mix had an average strength of 132 MPa (19.1 ksi) at 90 days, the age of the youngest plates tested.

Expected and actual results for the three and four-point bending tests can be seen in Figure 2-11 and Figure 2-12. A finite element model was run for the two types of tests that modeled the crack localization as hinges, the resultant curves are shown in these figures as well. The expected results calculations were based on the moment-curvature relationships derived in Figure 2-13. The actual results for both sets of tests had a high variance; in the case of the three-point bending test it approached 25%. These high values are believed to be a result of poorer mixing techniques used and the subsequent unpredictability in the fiber matrix.

The mechanical properties of Cor-Tuf are notable when compared to other UPFRC mixes. Prior to performing the mechanical testing, Williams et al. performed ultrasonic pulse-velocity measurements on each test specimen. The test works by propagating P-waves (compression) and S-waves (shear) through one end of the specimens and measuring their velocity at the opposite end. Additionally, composition property tests were performed to ascertain values for wet density, posttest water content, dry density porosity, and other compositional properties. These values for Cor-Tuf2 along with the pulse-velocity measurements are listed in Table 2-7. The collection of this data is significant as it allows for correlations to be developed between the physical and mechanical properties of Cor-Tuf. The correlations could then allow for further refining of the mix design and curing techniques if enhancement were desired.

2.4.1 Cor-Tuf Compressive Strength

Several tests were performed to ascertain the compressive strength of Cor-Tuf. The first of the tests to be performed were unconfined compressive tests on cylinders that were cored from large tub specimens. The use of a “tub” specimen promotes composition conformity among the specimens that are cored since all of the samples come from the same location. The cores were tested based on the American Society of Testing and Materials (ASTM) C 39 (Williams et al. 2009); the results of which can be seen in Table 2-8. The unconfined tests were performed using a manually controlled axial loader with a peak load of 750,000 lb. In addition to testing the standard Cor-Tuf1 and Cor-Tuf2 mixes, cylinders were tested from the Cor-Tuf1 batch that did not contain fibers. Testing of these cylinders allowed for ample comparison between Cor-Tuf with and without fibers as the composition of Cor-Tuf1 varies slightly from Cor-Tuf2 due to the inclusion of fibers.

Cor-Tuf specimens were also tested to determine their triaxial compressive strength. A 600 MPa capacity pressure vessel was utilized to carry out the triaxial tests; a diagram is shown in Figure 2-14. As shown in this figure, the load was supplied by an 8.9 MN loader that delivered its load through the loading piston. The load, pressure, and axial displacement of the loader were all controlled by the data acquisition system. This allowed the user to control these values to achieve the desired stress and strain. Measurements were taken from a pressure transducer immersed in the confining liquid, lateral deformeters to measure the radial deflection, load cells to measure the applied load, and linear variable differential transformers (LVDTs) to measure the displacement of the specimens. To ensure the specimens were not deteriorated by the confining fluid, all triaxial compression test specimens were coated in two layers of a latex membrane and an Aqua seal membrane. The confining-pressure fluid use was a mixture of kerosene and hydraulic fluid. Additionally, the specimens were placed between hardened steel top and base cap (Williams et al. 2009).

Unconfined compression tests and triaxial compression tests with confining pressure were performed with and without shear. The shear phase of the triaxial tests is created by increasing the axial load after reaching a constant confining pressure. Figure 2-15 depicts the stress-strain responses of two Cor-Tuf1 specimens during an unconfined compression test. The slope of the stress-strain diagram of the test is the Young's modulus, E . The unconfined compression results for Cor-Tuf2 are shown in Figure 2-16. Triaxial compression tests were performed for the specimens with the addition of confining pressures starting at 10 MPa up to 300 MPa. Figure 2-17 contains

the results for all of these tests for Cor-Tuf1. The results of similar tests for Cor-Tuf2 are shown in

Figure 2-18. From the unconfined compression test, the average unconfined compression of Cor-Tuf1 and Cor-Tuf2 were determined as 237 MPa and 210 MPa, respectively. Additionally, from the triaxial compression tests with a confining pressure of 300 MPa the mean normal stress of Cor-Tuf1 and Cor-Tuf 2 were 536 MPa and 525 MPa, respectively. However, the specimens had not yet reached full saturation or void closure and likely could have endured higher stresses. These stress-strain plots illustrate the brittle (below 200 MPa) and ductile (above 200 MPa) nature of Cor-Tuf. The results from the remainder of the triaxial compression tests and the hydrostatic compression tests are located in Williams et al. (2009).

2.4.2 Cor-Tuf Tensile Strength

The tensile strength of the Cor-Tuf specimens was determined through direct pull (DP) tests which were conducted by attaching end caps to the specimens using epoxy. The end caps were attached to the direct pull apparatus that pulled vertically on the caps during testing. Figure 2-19 and Figure 2-20 show the results of the direct pull test for Cor-Tuf1 and Cor-Tuf2, correspondingly. The values of principal stress difference at failure were -5.58 MPa and -8.88 MPa for Cor-Tuf1 and Cor-Tuf2, respectively. These values of tensile strength represent 2.4% and 4.2% of their respective compressive strengths. Normally tensile strengths are between 10% and 15% of the compressive strength of concrete (American Concrete Institute 2011). A strange phenomenon here is that Cor-Tuf1 with fiber reinforcement has a lower tensile strength than Cor-Tuf2. There are many possible explanations for this; it is possible the fibers were oriented

perpendicular to the direction of the force. However, it is believed that the flexural strength of Cor-Tuf1 will outperform that of Cor-Tuf2.

2.5 Dynamic Testing

The focus of this section will be the dynamic testing of UHPFRC and other related dynamic testing to the work that will be done. UHPFRC has excellent dynamic characteristics that have been tested in a variety of different experiments. In the sections that follow, a summary of each type of dynamic experiments that have been performed on UHPFRC will be provided.

2.5.1 Strain Rate Effects in Ultra High Performance Fiber Reinforced Concrete (UHPFRC)

An increase in strain rate due to the load being applied has been shown to create a corresponding increase in the apparent strength of the concrete being tested, which appears to hold true for UHPFRC as well. AFGC (2002) suggests that for ultra-high performance concrete experiencing 10^{-3} and 1 s^{-1} strain rates the increase in compressive and tensile strength is 1.5 and 2 times greater than its normal strength, respectively. The recent work by Parant et al. (2007) clearly illustrates the rate sensitive nature of UHPFRC.

Parant et al. (2007) studied strain rate effects on multi-scale fiber-reinforced cement-based composite (MSFRCC) using four-point bending tests and a block bar device on thin slabs. MSFRCC belongs to the UHPFRC class of concrete and contains 11% fiber by volume. The maximum fiber length used was 20 mm (0.79 in.). MSFRCC has a compressive strength of 220 MPa after 4 days of heat treatment at 90 °C, and it also has a modulus of rupture under four-point bending of 46 MPa. The slab specimens tested measured 600 mm (23.62 in.) in length, 200 mm (7.87 in.) in width and 40 mm

(1.57 in.) thickness. These slab dimensions favored an orthotropic fiber orientation due to the thickness of the slab and length of the fibers.

A diagram of the block-bar device setup is provided in Figure 2-21, no diagram was provided for the four point bending test. The four point bending tests were quasi-static with loading rates of: 3.3×10^{-3} mm/s, 3.3×10^{-1} mm/s, and 3.3 mm/s. The impact tests carried out in the block-bar device had stress rates of: 1.25×10^{-4} GPa/s, 1.25×10^{-2} GPa/s, and 1.25 GPa/s. The device uses a compressed-air gun to propel masses of up to 300 kg (661.39 lb) to velocities of up to 70 km/h (43.4 mph). For the experiment performed here, a 50 kg (110.23 lb) impactor was utilized. The increases of strength with increased strain rate are evident in Figure 2-22. The increase for MSFRCC represents an increase of 1.5 MPa/ \log_{10} unit (1.5 psi/ \log_{10} unit). However, it is noted that this rate is much higher than that seen in other UHPC mixes. Also for the purposes of comparison, Figure 2-23 contains a comparison of the results of UHP matrix (without fibers) to MSFRCC (with fibers) strengths versus stress rate.

Ngo et al. (2007), in addition to testing blast effects on ultra-high strength concrete (UHSC) panels, also tested strain rate effects in RPC cylinders measuring 50 mm (1.97 in) diameter cylinders. The RPC concrete cylinders had a compressive strength of 160 MPa and were tested at strain rates between $3 \times 10^{-5} \text{ s}^{-1}$ (quasi-static) up to 267.4 s^{-1} (dynamic). Testing showed that RPC is less strain-rate sensitive than NSC as can be seen in Figure 2-24. The dynamic increase factor (DIF) is the ratio of dynamic maximum stress to static maximum stress for a concrete specimen. Ngo et al. developed the following equations to calculate the DIF based on the strain-rate applied to specimens as well as predict the dynamic maximum stress based on the expected strain rate:

$$DIF = \frac{f'_{cd}}{f'_{cs}} = \left(\frac{\dot{\varepsilon}}{\dot{\varepsilon}_s} \right)^{1.026\alpha} \quad \text{for } \dot{\varepsilon} \leq \dot{\varepsilon}_1 \quad (2-1)$$

$$DIF = \frac{f'_{cd}}{f'_{cs}} = A_1 \ln(\dot{\varepsilon}) - A_2 \quad \text{for } \dot{\varepsilon} > \dot{\varepsilon}_1 \quad (2-2)$$

2.5.2 Split Hopkinson Pressure Bar

Rong et al. (2010) studied the effects of Split Hopkinson pressure bar (SPHB) tests on ultra-high performance cement based composite (UHPCC). The strength characteristics at 60 days for UHPCC appear in Table 2-9, the subscript of V represents the percent volume of fibers in the mix. SPHB tests consist of an incident and a transmitter pressure bar with the short specimen residing between them. When the striker contacts the specimen, three waves are generated: an incident compressive pulse, a reflected tensile pulse, and a transmitted compression wave. Based on one-dimensional stress-wave theory, Rong et al. provides the equations for stress, strain rate, and strain for the specimens:

$$\sigma = E \varepsilon_T(t) \frac{A}{A_0} \quad (2.3)$$

$$\dot{\varepsilon} = -\frac{2C_0}{l_0} \varepsilon_R(t) \quad (2.4)$$

$$\varepsilon = \int_0^t \dot{\varepsilon} dt \quad (2.5)$$

Figure 2-25 shows the results of the SHPB tests for each percentage of fiber (0%, 3% and 4%). These tests once again illustrate the strain-rate effect on UHPFRC; increasing strain rates yield higher stresses. Additionally, the strength and toughness

increased with fiber percentage, while the strain decreased. Toughness represents the area beneath the stress-strain curves. These results demonstrate the advantages produced by utilizing fiber reinforcement. Figure 2-26 shows the state of the samples post-test. The specimen with no fibers appears to have sustained brittle failure.

2.5.3 Blast Testing

A series of blast tests were performed by Wu et al. (2009) on NSC and UHPFRC slabs. Four of the slabs were reinforced normal concrete (RC) with a compressive strength of 39.5 MPa; these slabs were reinforced in both tension and compression and used as the control for the testing. Additionally, two UHPFRC slabs were created for blast testing. The UHPFRC slab contained fiber reinforcement, but no rebar; while the RUHPFRC contains fibers and the same reinforcement pattern as the RC slabs. The UHPFRC used for these two slabs had an average compressive strength of 151.6 MPa. All of the slabs that were tested measured 2000 mm (78.74 in.) long, 1000 mm (39.37 in.) wide and 100 mm (3.94 in.) thick, however the effective span of the slabs mounted in the support system was 1800 mm (70.87 in.). A diagram of the reinforcement geometry of the RC and RUHPFRC slabs are shown in Figure 2-27. The details for each slab including the type of charge used as well as scaled distance are found in Table 2-10.

Deflection results for all of the specimens are shown below in Table 2-11. While the NRC slabs performed adequately, the utility of UHPFRC became clear through these tests. For instance, the scaled distance for NRC-3 was almost twice that of the UHPFRC slab; however, they sustained almost identical deflections. A comparison of the cracking in both slabs is shown in Figure 2-28. The RUHPFRC experienced complete flexural failure as well as a deflection of over 100 mm (3.94 in.). However, considering

that this slab was subjected to a charged weight more than twice that of the other slabs in addition to a closer standoff distance, its performance was impressive.

2.5.4 Static and Impact Testing of Reinforced Concrete

2.5.4.1 Static testing of reinforced concrete

In addition to the impact tests that were performed, and are discussed below, Feldman and Siess performed static tests on beams with the same design as those used for the impact tests shown in

Figure 2-29 and Figure 2-30. The tests utilized the same simply supported system as the impact tests with a 106 inch clear span. Material properties for the concrete and reinforcement in the beam are provided in Table 2-12 and Table 2-13. The results of the static experiment can be seen in Figure 2-31 and Figure 2-32. The beam reached a peak load of approximately 30 kips and a maximum midspan deflection of 9 inches.

2.5.4.2 Impact testing of reinforced concrete

Feldman and Siess (1956, 1958) performed some of the first impact tests using advanced instrumentation (at the time). Their approach utilized a pneumatic loading system to dynamically load reinforced concrete beams they designed that are described in detail below. The velocity and force of the loading system were controlled by the type of gas, volume of gas, and height of travel necessary. The loader was supplied gas from a bottle and regulated by a manifold. The loading could produce 60 kips in either tension or compression within 10 milliseconds.

In addition to the existing instrumentation such as strain and deflection gauges, they also designed their own load cells to measure the reactions of the supports; moreover, the supports themselves were instrumented with strain gauges. These supports were fully anchored to the floor to prohibit movement. The entire system of

gauges and the loader were all controlled by a sequence control unit capable of sampling at 1 kilosample/sec.

The purpose of the Feldman and Siess experiments were to test the impact capabilities of reinforced concrete beams. The design of these beams can be seen in

Figure 2-29 and Figure 2-30 where L, the clear span, is 106 inches. The reinforcement was outfitted with strain gauges. In order to accomplish this, gages were attached to the steel before pouring the concrete and ensure they were water tight. The gauges were fitted at one-sixth intervals of the clear span (106 in). Furthermore, deflection gages were placed at the same locations to create an accurate picture of the deflection along the beams. Additionally, a 500 g accelerometer was placed at the center of each beam to back up the results of the rest of the instrumentation, and vice versa. Details of the reinforcing regiment utilized appear in Table 2-12 and Table 2-13 provides the details of the concrete mixture used for the beams including the strength characteristics.

At the time of these experiments, computers were only just coming into existence. Their capabilities were limited and only allowed for the simplest of work in modern terms. Feldman and Siess utilized an ILLIAC computer to analyze the beams as a single degree of freedom (SDOF) system. The following equation was utilized to calculate the natural period of vibration of the beam:

$$T = 2\pi \sqrt{\frac{M_e \Delta_y}{Q_y}} \quad (2- 6)$$

A representation of the load-beam system appears in Figure 2-33. The following equations were used to calculate the displacement at n and the velocity at n , respectively:

$$\Delta_n = \frac{3nL^2 - 4n^3}{L^3} \Delta_c \quad (2-7)$$

$$\dot{\Delta}_n = \frac{3nL^2 - 4n^3}{L^3} \dot{\Delta}_c \quad (2-8)$$

The SDOF solution calculated by the ILLIAC computing system relied on these equations, equations to calculate the kinetic energy of the beam and Newmark- β method (Feldman and Siess 1956). Furthermore, Newmark- β method is used to calculate displacements and velocities and specify time steps that allow for a detailed picture of the beam behavior. The results of the experiment can be seen in Figure 2-34 where the beam, after being subjected to approximately 35 kips for 50 milliseconds, experienced a maximum midspan deflection of 8.5 inches. The applied load will be presented and discussed further in the chapter on model validation.

2.5.5 Impact Testing of UHPFRC

Drop hammer testing offers in depth looks at the dynamic capabilities of specimens without the necessary facilities and equipment needed for blast loading conditions. For this reason, it has become popular for testing of concrete specimens, especially UHPFRC. Drop hammer testing is also flexible and allows for a variety of testing situations that vary in loading, loading rate, number of impacts, and type of specimen. The drop hammers used in the following research papers were all fully

instrumented including photo eye sensors, linear variable differential transformers (LVDT's), accelerometers, potentiometers, and strain gauges.

Habel and Gauvreau (2008) performed drop hammer tests on a series of plates with varying loads and a fixed drop height. The CEMTEC_{multiscale} (Rossi et al. 2005) plates tested measured 600 mm (23.6 in) long, 145 mm (5.7 in.) wide and 50 mm (2.0 in.) thick and had a 90 day strength of 132 MPa (19.1 ksi). A diagram and photo of the test setup are shown in Figure 2-35. For these tests, weights of 10.2 and 20.6 kg (22.5 and 45.4 lbs) were used from a constant drop height of 1050 mm (41.3 in.). From this height, the high-speed camera measured the velocity of the hammer as 4.2 m/s (13.8 ft/s) for the 10.3 kg weight and 4.3 m/s (14.1 ft/s) for the 20.6 kg weight. A small section of plywood was placed where the striker was meant to hit the plates to reduce vibration.

The mass-spring model depicted in Figure 2-36 was used to predict the performance of the plates during impact loading. A shape function (Φ) was determined for the UHPFRC plate and it was approximated as a concentrated mass (m_p), and this shape function was based on the deflected shape of the specimen. The following equation was used to calculate the concentrated mass of the plate:

$$m_p = \int_0^l \bar{m} \Phi^2(x) dx \quad (2.9)$$

The springs, R_p and R_D , represented in Figure 2-36 are nonlinear. The equations below are the mathematical formulation of the model, including inertial effects:

$$m_{DW} \left(\frac{d^2 u_{DW}}{dt^2} - \frac{d^2 u_p}{dt^2} \right) + R_D(u_{DW} - u_p) = 0 \quad (2.10)$$

$$m_p \frac{d^2 u_p}{dt^2} + R_p(u_p) - R_D(u_{DW} - u_p) = 0 \quad (2.11)$$

Table 2-14 contains the results for the drop hammer tests with the weight variation and the number of drops indicates the number required for complete fracture of the specimen. The variation of results seen here, as in the quasi-static tests previously mentioned, is attributed to the disparity in fiber distribution. The table indicates a maximum strain rate of 2 s^{-1} , which is equivalent to the impact of a vehicle. These tests had a maximum deflection of -4.1 and -5.7 mm (-0.16 in. and -0.22 in.), respectively. Figure 2-37 shows the graphical results for maximum drop weight and maximum deflection of the plates which can be compared to the results in Figure 2-11. By comparing the peak forces, a 50% increase can be seen for the plates.

Fujikake et al. (2006) performed drop hammer tests on reactive power concrete (RPC) I-beams, a cross sectional view is shown in Figure 2-38. The composition of the RPC utilized for these beams can be seen in Table 2-15. The RPC specimens were cured for two days at $90 \text{ }^{\circ}\text{C}$ and had a compressive strength of 215 MPa (31.2 ksi). The three longitudinal bars in the beams are 13 mm (0.5 in) in diameter with an effective depth of 170 mm (6.7 in.), equating to a reinforcement ratio of 2.6%. The drop hammer test setup shown in Figure 2-39 utilized a 400 kg mass dropped from heights of 0.8, 1.0, 1.2, 1.4 and 1.6 meters to impact the RPC beams. The RPC beams were 1700 mm (5.6 ft) long with a clear span of 1200 mm (3.9 ft).

The results of two drop test heights, 0.8 m and 1.2 m, are shown in Figure 2-40. The loading for each height varied slightly; however, the deflection increased steadily with greater drop heights. The residual load curve for these beams was created by statically loading each beam after performing the impact test. This type of test is rare and is good information for designers to know. When designing for blast loads, this

information can be utilized to plan for blast events and the necessary residual strength to ensure the integrity of the structure.

2.6 Numerical Simulations

2.6.1 Finite Element Analysis

Finite Element Analysis (FEA), also known as the Finite Element Method (FEM) is a numerical method for solving field problems (Cook et al. 2002). Field problems, as defined by Cook, are utilized to determine the spatial distribution of one or more dependent variables that can be such things as temperatures, stresses or displacements in the object being modeled. Due to this wide applicability, FEA is utilized in all aspects of engineering.

Field problems are described mathematically by differential equations or integrals. In order to solve these problems, the spatial distribution must be determined for the dependent variables. The variables are separated into two classes: primary variables such as displacement or temperatures and secondary variables such as forces or stresses that are derived from primary variables. The flow process shown in Figure 2-41 from (Bathe 1995) details the methodology for solving FEA problems.

In order to solve an FEA problem, it is vital to properly define the physical phenomena and behavior of the problem. The mathematical model created from these definitions is idealized for a simple solution and is therefore based on any assumptions from the definition. Finite element models are approximations and require comparison to experimental results in order to be properly validated. Proper validation of the models will allow for confidence in the solution created; consequently, for each new finite element solution, validation will need to be performed.

The process behind the finite element method involves estimating the solution of a complex problem by replacing it with a simpler model. The problem is divided into a mesh of finite sized elements. The variation of displacement in each element is determined by simple polynomial shape functions and nodal displacements. The secondary variables are calculated then from these nodal displacements. These equations of equilibrium are placed into matrix form for easy solution by computer codes. With the boundary conditions accounted for, the nodal displacements can be solved for by solving the stiffness matrix. The stress, strains and other values are then determined from these values. This simplification of complex problems allows for the finite element code to solve a wide variety of physical problems.

2.6.2 Abaqus Finite Element Analysis Software

The FEA code utilized for the research performed here is the Abaqus v6.11 (Simulia 2011). Abaqus is available in three products: Abaqus/Standard, Abaqus/Explicit and Abaqus/CFD. Abaqus/Standard and Abaqus/Explicit are the two products used mainly for structural modeling. Abaqus has the ability to model both linear and non-linear problems. Additionally, Abaqus has comprehensive library of material models and element properties to choose from. The software also allows for modeling of a wide variety of other scenarios including heat transfer, acoustic, soil mechanics and many other problems.

Abaqus/Standard can be used for both static and dynamic solutions. The solutions are implicit: for a static problem the product solves a series of equation at each “increment”, for a dynamic problem it solves equations of motion at each time step. From this, the global stiffness matrix is formed and the solutions are derived from the inversion of the stiffness matrix. Abaqus/Explicit uses explicit integration where the

equations of motion are satisfied at t_i , the current time step, and extrapolated to determine the solution of t_{i+1} , the next time step. The time step increments need to be small due to the extrapolation results in order to ensure accuracy of the solutions. Abaqus/Explicit is therefore appropriate for modeling fast and transient dynamic events such as blast, impact and contact problems.

The implicit integration analysis utilized by Abaqus/Standard requires the full stiffness matrix to be inverted in order to obtain a solution. This is computationally expensive since equilibrium must be satisfied at each time step. On the other hand, explicit integration analysis does not require matrix inversion to solve the problem. Despite the small time step required to guarantee accurate results, the explicit integration analysis is normally computationally cheaper than implicit. Additionally, explicit analysis is more suitable to non-linear analysis since the small time step allows for the capture of the transition between linear and non-linear behavior.

Zineddin (2002) utilized the Abaqus/Explicit code to model the behavior of slabs under impact. The results gathered from this experiment compared favorably to the simulations performed in Abaqus/Explicit.

2.6.3 Dynamic Structural Analysis Suite

Dynamic Structural Analysis Suite (DSAS) is a software package that has been under continuous development by Krauthammer since the late 1970s for analyzing a variety of structural members in both static and dynamic cases (Astarlioglu and Theodor Krauthammer 2009). The software is based on SDOF methods and allows for a quick analysis of a scenario, with runs generally not exceeding five seconds. The software allows for the analysis of beams, columns, slabs and even user defined shapes that utilize steel or concrete as well as longitudinal and shear reinforcement. The program

has also been designed to incorporate options for UHPC based on the results from testing of Ductal. Furthermore, the software allows for the addition of DIFs as well as damping, variation in support conditions, inclusion of diagonal shear and a variety of other features. The software cannot provide the in depth analysis data of an FEA simulation; however, for fast analyses DSAS provides accurate results with low computational cost, especially for highly dynamic cases. DSAS will be utilized not only for model validation, but also for predictions of the experimental work to be performed.

DSAS calculates individual dynamic increase factors (DIF) for concrete in compression, concrete in tension and the reinforcement. The methodologies for calculating the DIFs for the concrete in compression, tension and the reinforcement were derived from CEB-FIB 1990 (1993), Ross et al. (1989) and Soroushian and Obaseki (1986), respectively. DSAS calculates the DIFs based on either specified strain rates or can estimate the strain rates based on the loading rate.

Table 2-1. Composition of CEMTEC_{multiscale} (Rossi, P., Arca, A., Parant, E., and Fakhri, P. (2005). "Bending and compressive behaviours of a new cement composite." *Cement and Concrete Research*, 35(1), 27-33.)

Formulation of CEMTEC _{multiscale} (kg/m ³)	
Cement	1050.1
Silica Fume	268.1
Sand	514.3
Water	180.3
Superplasticizer	44
Steel Fibers	858
Water/cement = 0.201	
Water/binder = 0.16	
Air entrained = 20 1	

Table 2-2. Composition of compact reinforced concrete (CRC) (Bindiganavile, V., Banthia, N., and Aarup, B. (2002). "Impact Response of Ultra-High-Strength Fiber-Reinforced Cement Composite." *ACI Materials Journal*, (99-M55), 543-548.)

Composite	Cement	Water	Silica Fume	High-range water-reducing admixture	Ingredient, kg/m ³		Concrete Sand	9.5 mm coarse aggregate	Fiber V _f
					Quartz sand Size range, mm	Quantity			
CRC	750	150	179	21	0.00 to 0.25	189	----	----	457
					0.25 to 1	383			
					1 to 4	613			

Table 2-3. Compressive strength (MPa) values with varying percentages of silica fume (Mazloom, M., Ramezaniapour, a. a., and Brooks, J. J. (2004). "Effect of silica fume on mechanical properties of high-strength concrete." *Cement and Concrete Composites*, 26(4), 347-357.)

Concrete mixes	Age (days)						
	7	14	28	42	90	365	400
OPC	46	52	58	62	64	73	74
SF6	50.5	58	65	69	71	73	73
SF10	52	61	67.5	71	74	74	73
SF15	53	63	70	73	76	75	76

Table 2-4. Shrinkage for concrete with varying percentages of silica fume (Mazloom, M., Ramezaniapour, a. a., and Brooks, J. J. (2004). "Effect of silica fume on mechanical properties of high-strength concrete." *Cement and Concrete Composites*, 26(4), 347-357.)

Kind of shrinkage	Concrete mixes			
	OPC	SF6	SF10	SF15
Total	532	528	523	512
Autogenous	198	231	264	297
Drying	334	297	259	215

Table 2-5. Peak load and fracture energy for cellulose fiber split cylinder tests (Peters, S. J. (2009). "Fracture toughness investigations of micro and nano cellulose fiber reinforced ultra high performance concrete." The University of Maine.)

	No. of Specimens	Peak Load (N)	COV	Fracture Energy (mJ)	COV
Baseline	34	2050	0.26	90	0.22
1% Micro Fiber	36	1800	0.24	100	0.27
1% Nano Fiber	32	1800	0.19	100	0.4
3% Micro Fiber	40	2100	0.24	170	0.28
3% Nano Fiber	30	1950	0.43	57	0.5
Hybrid	30	2400	0.32	80	0.34

Table 2-6. Mix proportions for Cor-Tuf concrete (Williams, E. M., Graham, S. S., Reed, P. A., and Rushing, T. S. (2009). *Concrete With and Without Steel Fibers Geotechnical and Structures Laboratory Concrete With and Without Steel Fibers*. Vicksburg, MS.)

Material	Product	Proportion by Weight
Cement	Lafarge, Class H, Joppa, MO	1.00
Sand	US Silica, F55, Ottawa, IL	0.967
	US Silica, Sil-co-Sil 75, Berkeley Springs, WV	
Silica flour		0.277
Silica fume	Elkem, ES 900 W	0.389
Superplasticizer	W.R. Grace, ADVA 170	0.0171
Water (tap)	Vicksburg, MS Municipal Water	0.208
Steel Fibers ¹	Bekaert, Dramix ® ZP305	0.31

¹ Steel fibers used in Cor-Tuf1 material only

Table 2-7. Physical and composition properties of Cor-Tuf2 (Williams, E. M., Graham, S. S., Reed, P. A., and Rushing, T. S. (2009). *Concrete With and Without Steel Fibers Geotechnical and Structures Laboratory Concrete With and Without Steel Fibers*. Vicksburg, MS.)

Test Number	Type of Test	Wet Density Mg/m ³	Posttest Water Content %	Dry Density Mg/m ³	Porosity %	Degree of Saturation %	Volume of Air %	Volume of Water %	Volume of Solids %	Axial P-wave Velocity km/s	Radical P-wave Velocity km/s	Axial S-wave Velocity km/s	Radical S-wave Velocity km/s
1	HC	2.343	1.36	2.312	16.55	19	13.4	3.14	83.45	5.05	4.97	3.14	3.25
2	UX	2.347	3.99	2.257	18.51	48.66	9.5	9.01	81.49	5.11	4.96	3.21	3.26
3	HC	2.32	1.46	2.286	17.46	19.12	14.12	3.34	82.54	5.03	4.95	3.16	3.25
4	UX	2.324	3.97	2.235	19.3	45.97	10.43	8.87	80.7	5.05	4.96	3.18	3.24
5	TXC/10	2.322	2.39	2.267	18.14	29.87	12.72	5.42	81.86	5.07	4.97	3.17	3.22
6	TXC/10	2.31	3.01	2.243	19.04	35.46	12.29	6.75	80.96	5.05	4.94	3.2	3.25
7	TXC/20	2.319	2.78	2.257	18.54	33.84	12.26	6.27	81.46	5.03	4.97	3.13	3.23
8	TXC/20	2.337	2.16	2.287	17.42	28.35	12.48	4.94	82.58	5.1	4.98	3.18	3.29
9	TXC/50	2.314	2.93	2.248	18.83	34.99	12.24	6.59	81.17	5.08	4.99	3.17	3.26
10	TXC/50	2.341	3.56	2.261	18.38	43.8	10.33	8.05	81.62	5.09	4.99	3.19	3.26
11	TXC/100	2.334	3.53	2.255	18.6	42.79	10.64	7.96	81.4	5.02	4.99	3.16	3.24
13	UX/CV	2.335	3.96	2.246	18.9	47.06	10.01	8.9	81.1	5.04	4.98	3.17	3.22
14	UX/CV	2.335	3.96	2.246	18.9	47.06	10.01	8.9	81.1	5.04	4.98	3.17	3.22
15	UX	2.32								5.03	4.96	3.15	3.24
16	UX/CV	2.317								5.07	4.95	3.18	3.26
17	TXC/100	2.321	3.27	2.248	18.85	39	11.5	7.35	81.15	5.04	4.97	3.17	3.26
18	TXC/200	2.335	4.28	2.239	19.17	49.98	9.59	9.58	80.83	5.07	4.97	3.17	3.23
19	TXC/200	2.332	4.34	2.235	19.31	50.25	9.61	9.7	80.69	5	4.98	3.16	3.23
20	TXC/300	2.329	4.17	2.236	19.28	48.36	9.96	9.32	80.72	5.07	4.98	3.16	3.24
21	TXC/300	2.327	4.52	2.227	19.61	51.32	9.55	10.07	80.39	5.02	4.97	3.17	3.23
23	UC	2.336	3.58	2.256	18.57	43.48	10.5	8.08	81.43	5.08	4.99	3.17	3.23
24	UC	2.318	3.66	2.236	19.26	42.5	11.08	8.19	80.74	5	4.98	3.16	3.24
26	DP	2.33	1.1	2.304	16.81	15.08	14.27	2.53	83.19	5.04	4.99	3.16	3.26
N		23	21	21	21	21	21	21	21	23	23	23	23
Mean		2.328	3.24	2.256	18.54	38.85	11.26	7.28	81.46	5.05	4.97	3.17	3.24
Stdv		0.01	1.023	0.023	0.838	11.061	1.541	2.261	0.838	0.03	0.014	0.017	0.018
Max		2.347	4.52	2.312	19.61	51.32	14.27	10.07	83.45	5.11	4.99	3.21	3.29
Min		2.31	1.1	2.227	16.55	15.08	9.5	2.53	80.39	5	4.94	3.13	3.22

Table 2-8. Unconfined compressive strength for Cor-Tuf cylinders (Williams, E. M., Graham, S. S., Reed, P. A., and Rushing, T. S. (2009). *Concrete With and Without Steel Fibers Geotechnical and Structures Laboratory Concrete With and Without Steel Fibers*. Vicksburg, MS.)

Cor-Tuf1 UC Strength, Mpa			Cor-Tuf 2 UC Strength, Mpa
75-by 150-mm Cylinder	100-by 200-mm Cylinder	75-by 150-mm Cylinder Without Steel Fibers	75-by 100-mm Cylinder
237	216	216	228
231	219	208	225
243	226	206	209
233	228		190
238	229		225
244			209

Table 2-9. Mechanical properties of ultra-high performance cement based composite (UHPCC) (Rong, Z., Sun, W., and Zhang, Y. (2010). "Dynamic compression behavior of ultra-high performance cement based composites." *International Journal of Impact Engineering*, Elsevier Ltd, 37(5), 515-520.)

Number	Compressive strength (MPa)	Peak value of strain ($\times 10^{-3}$)	Elastic modulus (GPa)	Toughness index		
				η_{c5}	η_{c10}	η_{c30}
UHPCC(V ₀)	143	2.817	54.7	2.43	2.43	2.43
UHPCC(V ₃)	186	3.857	57.3	3.59	5.08	5.57
UHPCC(V ₄)	204	4.165	57.9	4.57	6.32	7.39

Table 2-10. Slab reinforcement and charge description (Wu, C., Oehlers, D. J., Rebentrost, M., Leach, J., and Whittaker, a. S. (2009). "Blast testing of ultra-high performance fibre and FRP-retrofitted concrete slabs." *Engineering Structures*, Elsevier Ltd, 31(9), 2060-2069.)

Blast	Slab name	Description	Rebar ratio (%)	Standoff distance (m)	Scaled distance (m/kg ^{1/3})	Explosive mass (g)
NRC-1	1A	RC	1.34	3	3	1007
NRC-2	1A	RC	1.34	3	1.5	8139
NRC-3	1B	RC	1.34	1.4	0.93	3440
NRC-4	1A	RC	1.34	1.5	0.75	8213
RET-1a	3A	RCCCFRP	1.34	1.5	1.5	1044
RET-2a	3B	RCCCFRP	1.34	0.92	0.54	5083
UHPFC	D1B	UHPFC	—	0.75	0.5	3433
RUHPFC	D3A	RUHPFC	1.34	1	0.37	20101

Table 2-11. Deflections for slabs subject to blast (Wu, C., Oehlers, D. J., Rebentrost, M., Leach, J., and Whittaker, a. S. (2009). "Blast testing of ultra-high performance fibre and FRP-retrofitted concrete slabs." *Engineering Structures*, Elsevier Ltd, 31(9), 2060-2069.)

Blast	Charge weight (kg)	Standoff distance from PT1 (m)	Scaled distance (m/kg ^{1/3})	Max. Deflection (mm)	Permanent deflection (mm)
NRC-1	1	3	3	1.5	0
NRC-2	8	3	1.5	10.5	— ^a
NRC-3	3.4	1.4	0.93	13.9	— ^a
NRC-4	8	1.5	0.75	38.9	— ^a
RET-1	1	1.5	1.5	3.3	0
RET-2	5	0.92	0.54	50.6	7.6
UHPFC	3.4	0.75	0.5	13.2	4.1
RUHPFC	20	1	0.37	>100	— ^b

^a LVDT debonded from the concrete and the permanent deflection was not recorded.

^b LVDT was destroyed by the test.

Table 2-12. Properties of steel in Feldman and Siess beams (Feldman, A., and Siess, C. P. (1958). *Investigation of Resistance and Behavior of Reinforced Concrete Members Subjected to Dynamic Loading - Part II*. Urbana, Illinois.)

Beam	Tension Reinforcement					Compression Reinforcement					Shear
	f_y ksi.	E_s ksi.	ϵ_y in./in.	ϵ_o in./in.	α	f'_y ksi.	E'_s ksi.	ϵ'_y in./in.	ϵ'_o in./in.	α	f_w ksi.
1-c	46.08	29520	.0016	.0144	.0271	46.70	---	---	---	---	---
1-d	46.25	---	---	---	---	47.16	---	---	---	---	48.8
1-e	46.75	---	---	---	---	47.16	---	---	---	---	47.5
1-f	46.83	---	---	---	---	47.27	---	---	---	---	---
1-g	47.75	---	---	---	---	48.30	---	---	---	---	49.5
1-h	47.17	34900	.0014	.0125	.0229	47.61	32280	.0015	.0150	.0226	46.9
1-i	47.00	32600	.0014	.0150	.0254	47.95	---	---	---	---	49.6
1-j	47.42	---	---	---	---	48.86	29560	.0016	.0120	.0338	---

Table 2-13. Concrete properties for Feldman and Siess beams (Feldman, A., and Siess, C. P. (1958). *Investigation of Resistance and Behavior of Reinforced Concrete Members Subjected to Dynamic Loading - Part II*. Urbana, Illinois.)

For all beams: b = 6 in., h = 12 in., d = 10 in., d' = 8.5 in., Span = 106 in. Tension reinforcement: 2 - No. 7 bars = 1.20 sq. in. p = 2.00% Compression reinforcement: 2 - No. 6 bars = 0.88 sq. in. p' = 1.46% Stirrups: No. 3 at 7 in. r = 0.524%									
PART A CONCRETE MIXES									
Beam	Batch	Sand Cement by weight	Gravel Cement by weight	Cement Water by weight	Slump in.	Compressive Strength, f'_c psi.	Modulus of Rupture, f_r psi.	Modulus of Elasticity, E_c ** psi. x 10^6	Age at Test days
1-c	1	2.93	3.53	1.46	2	5670	900	3.88	275
	2	2.93	3.53	1.48	3 1/2	6000	733	4.00	
1-d	1	2.98	3.50	1.72	2	6010	750	3.90	280
	2	3.00	3.51	1.67	5	6060	667	4.00	
1-e	1	2.90	3.50	1.44	7	5870	758	---	476
	2	2.92	3.52	1.70	5	6165	742	4.08	
1-f	1	2.95	3.48	1.63	4	6320	825	4.27	221
	2	2.96	3.50	1.69	5	6550	817	4.27	
1-g	1	2.98	3.50	1.72	2	6210	1000	4.59	298
	2	3.00	3.52	1.72	4	6565	950	4.59	
1-h	1	2.95	3.46	1.51	6	6150	935	4.45	302
	2	2.96	3.48	1.55	7	5775	935	4.45	
1-i	1	2.95	3.50	1.63	6	6500	850	4.73	303
	2	2.96	3.53	1.66	6	6475	860	4.73	
1-j	1	2.94	3.50	1.59	5 1/2	6090	935	3.89	297
	2	2.95	3.53	1.58	6 1/2	5910	860	4.39	

* Strength of concrete in a beam is considered to be strength of batch 2.

** Initial Tangent Modulus

Table 2-14. Results for the Habel and Gauvreau drop hammer tests (Habel, K., and Gauvreau, P. (2008). "Response of ultra-high performance fiber reinforced concrete (UHPFRC) to impact and static loading." *Cement and Concrete Composites*, Elsevier Ltd, 30(10), 938-946.)

Specimen name (-)	Drop weight (kg)	Number of drops (-)	First Drop			
			Max. f_1 (mm)	Max. F_{DW} (kN)	Max. F_{SU} (kN)	Max. $d\varepsilon/dt$ (s^{-1})
10kg_1	10.3	4	-4.1	23	24.5	2.5
10kg_2	10.3	5	-4.2	23.4	25.3	2.6
10kg_3	10.3	5	-4.6	22.8	26.4	3
10kg_4	10.3	3	-5.1	23.5	18.5	2.4
10kg_5	10.3	3	-5.1	21.6	16.7	2.8
10kg_6	10.3	3	-5.2	21.5	14.8	1.9
10kg_7	10.3	3	-5.7	23.3	20.9	2.7
20kg_1	20.6	2	-6.5	26.3	30.7	2.3
20kg_2	20.6	2	-12.2	23.4	19.7	3.1
20kg_3	20.6	1	— ^a	23	14.3	3.5
20kg_4	20.6	1	— ^a	23.8	13.3	3.4
20kg_5	20.6	1	— ^a	23.8	17.1	3.3
20kg_6	20.6	1	— ^a	22.8	16.5	2.9

^a Not applicable due to complete failure of the specimen at first drop

Table 2-15. Reactive powder concrete (RPC) mix proportions (Fujikake, K., Senga, T., Ueda, N., Ohno, T., and Katagiri, M. (2006). "Study on Impact Response of Reactive Powder Concrete Beam and Its Analytical Model." *Journal of Advanced Concrete Technology*, 4(1), 99-108.)

Fiber volume fraction V_f (%)	2.0
Water-cement ratio W/C (%)	22.0
Water*1 (kg/m^3)	180
Pre-blended powders [Ductal] (kg/m^3)	2254
Steel fiber (kg/m^3)	157
Superplasticizer (kg/m^3)	25

*1 including superplasticizer

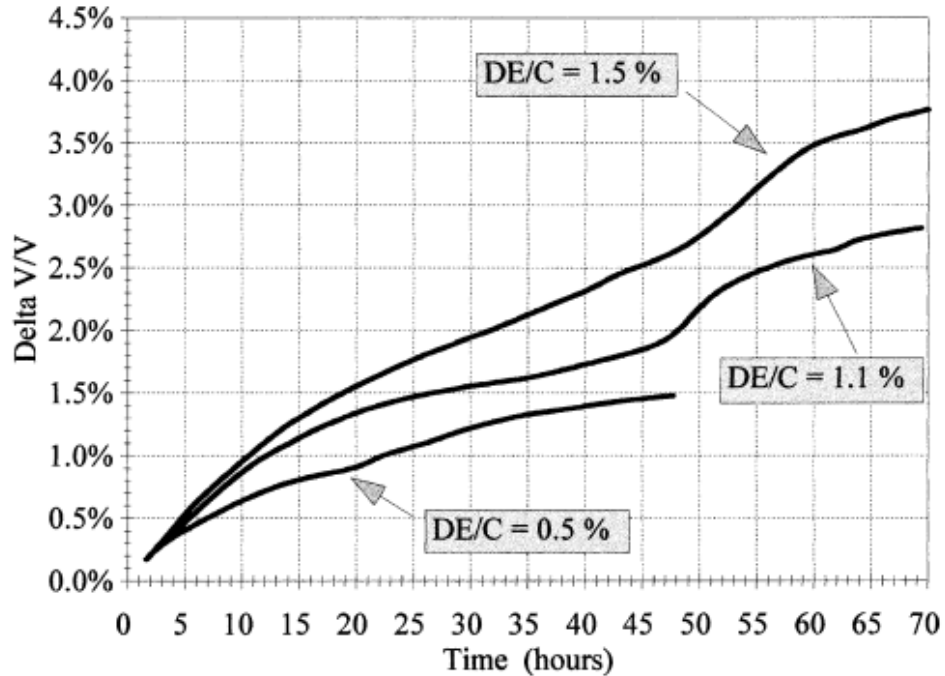


Figure 2-1. Early age shrinkage in concrete with varying levels of superplasticizer (Morin, V., Cohen Tenoudji, F., Feylessoufi, a., and Richard, P. (2001). "Superplasticizer effects on setting and structuration mechanisms of ultrahigh-performance concrete." *Cement and Concrete Research*, 31(1), 63-71.)

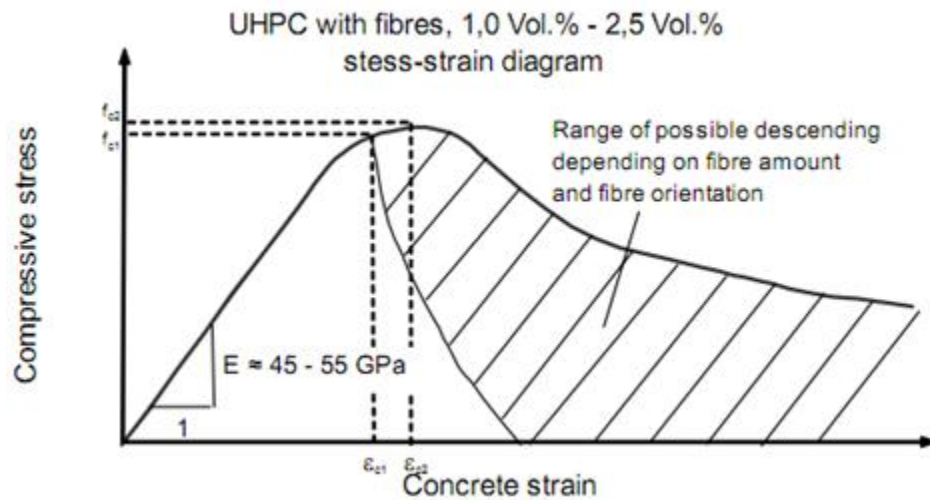


Figure 2-2. Compressive strength curve with the addition of fibers (Fehling, E., Bunje, K., and Leutbecher, T. (2004). "Design relevant properties of hardened Ultra High Performance Concrete." *International Symposium on Ultra High Performance Concrete*, Kassel, Germany, 327-338.)

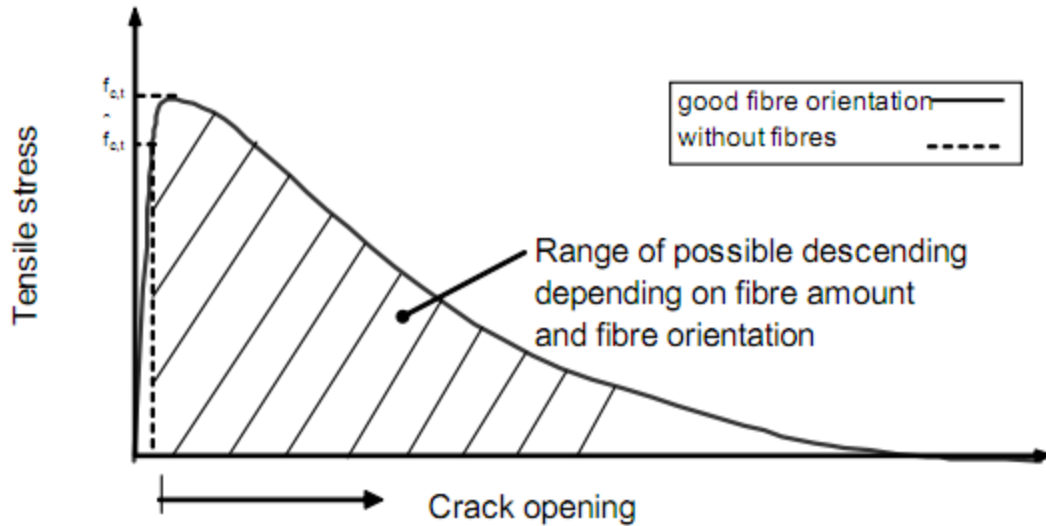


Figure 2-3. Tensile strength curve with the addition of fibers (Fehling, E., Bunje, K., and Leutbecher, T. (2004). "Design relevant properties of hardened Ultra High Performance Concrete." *International Symposium on Ultra High Performance Concrete*, Kassel, Germany, 327-338.)

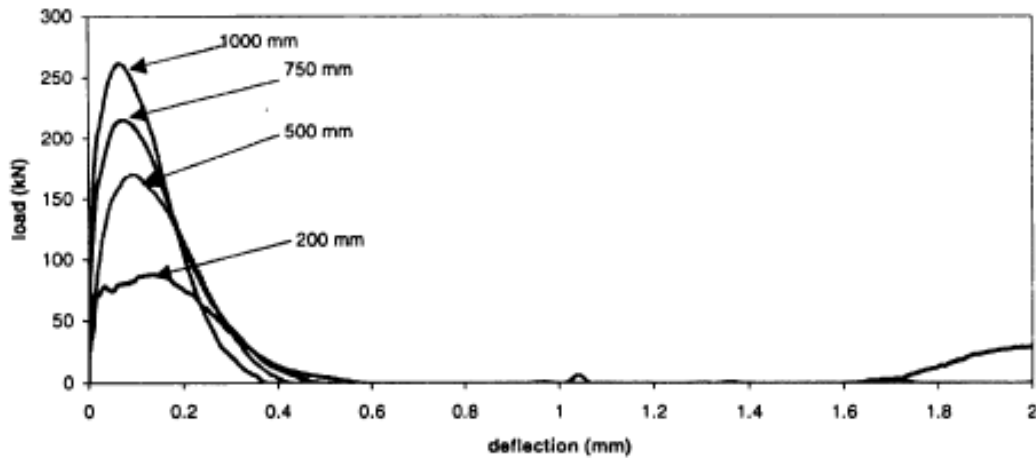


Figure 2-4. Impact performance of normal-strength polymer macro-FRC (PFRC) (Bindiganavile, V., Bantia, N., and Aarup, B. (2002). "Impact Response of Ultra-High-Strength Fiber-Reinforced Cement Composite." *ACI Materials Journal*, (99-M55), 543-548.)

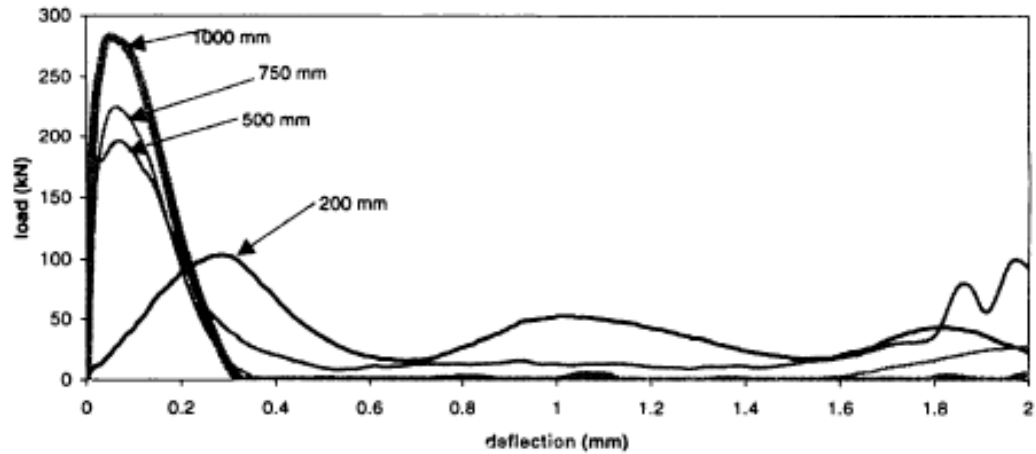


Figure 2-5. Impact performance of normal-strength steel FRC (SFRC) (Bindiganavile, V., Banthia, N., and Aarup, B. (2002). "Impact Response of Ultra-High-Strength Fiber-Reinforced Cement Composite." *ACI Materials Journal*, (99-M55), 543-548.)

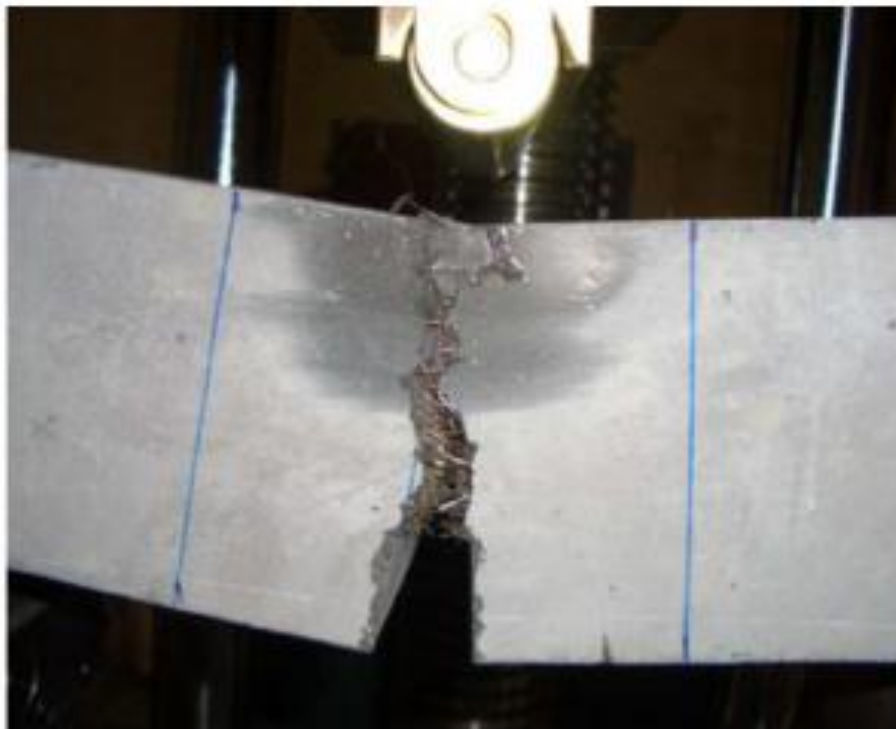


Figure 2-6. Fiber protrusion from cracked beam (Kang, S., Lee, Y., Park, Y., and Kim, J. (2010). "Tensile fracture properties of an Ultra High Performance Fiber Reinforced Concrete (UHPFRC) with steel fiber." *Composite Structures*, Elsevier Ltd, 92(1), 61-71.)

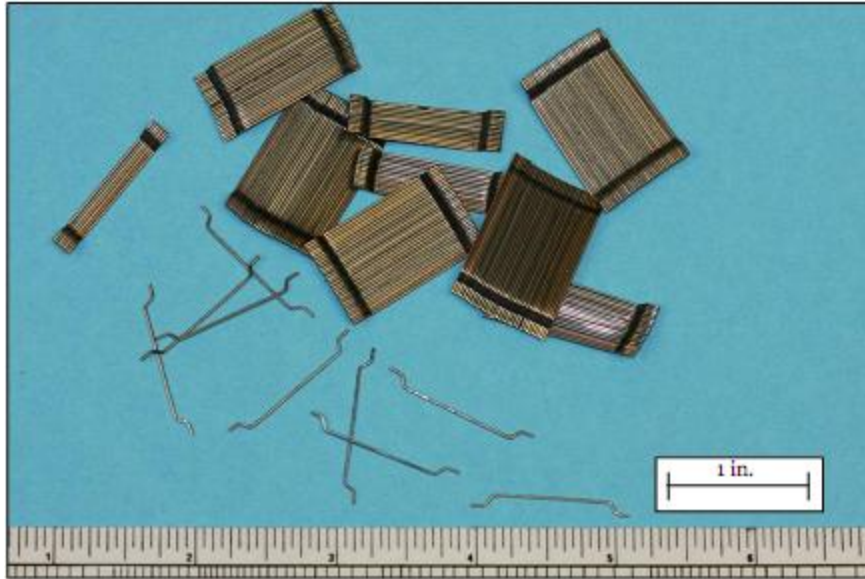


Figure 2-7. Dramix ZP305 Fiber (Williams, E. M., Graham, S. S., Reed, P. A., and Rushing, T. S. (2009). *Concrete With and Without Steel Fibers Geotechnical and Structures Laboratory Concrete With and Without Steel Fibers*. Vicksburg, MS.)

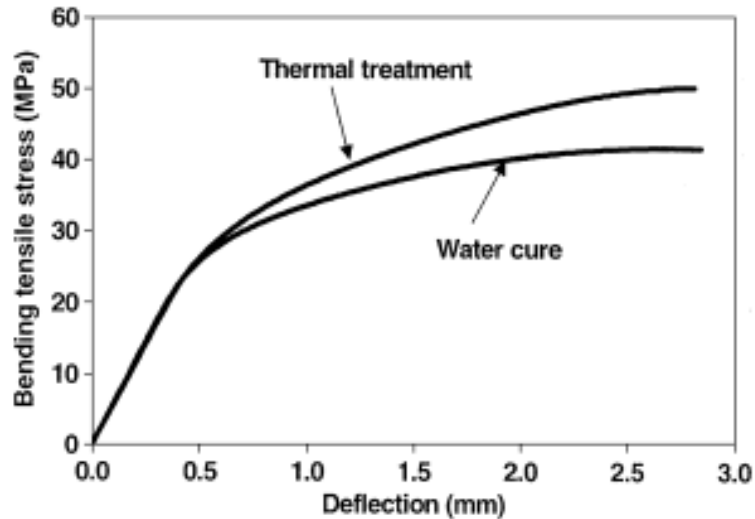


Figure 2-8. Bending tensile stress versus deflection for heat treated and water cured concrete (Rossi, P., Arca, A., Parant, E., and Fakhri, P. (2005). "Bending and compressive behaviours of a new cement composite." *Cement and Concrete Research*, 35(1), 27-33.)

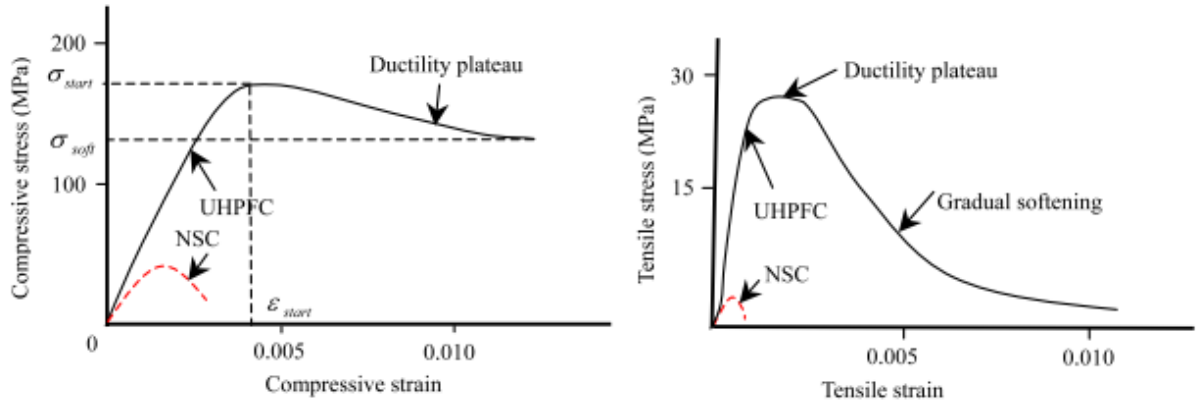


Figure 2-9. Typical ultra-high performance fiber reinforced concrete (UHPFRC) strength characteristics (Wu, C., Oehlers, D. J., Rebertost, M., Leach, J., and Whittaker, a. S. (2009). "Blast testing of ultra-high performance fibre and FRP-retrofitted concrete slabs." *Engineering Structures*, Elsevier Ltd, 31(9), 2060-2069.)

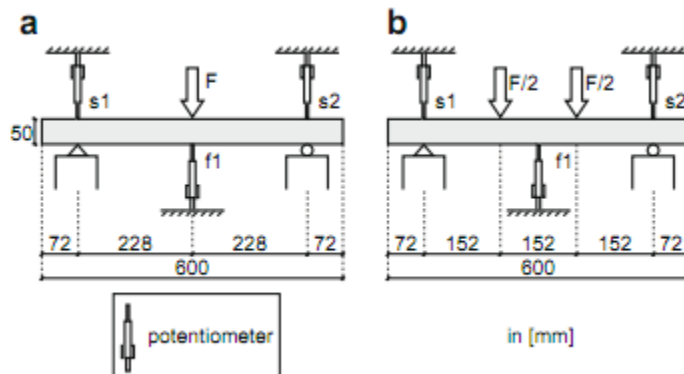


Figure 2-10. (a) Three-point bending test setup; (b) Four-point bending test setup (Habel, K., and Gauvreau, P. (2008). "Response of ultra-high performance fiber reinforced concrete (UHPFRC) to impact and static loading." *Cement and Concrete Composites*, Elsevier Ltd, 30(10), 938-946.)

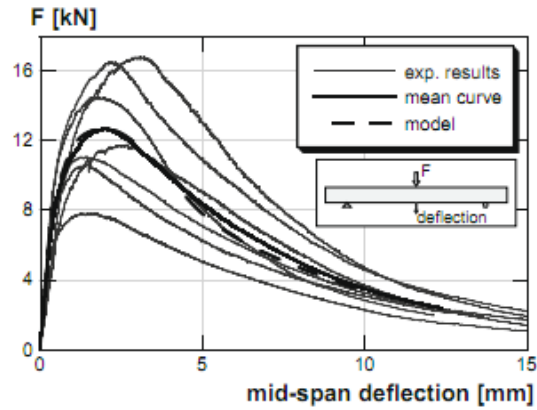


Figure 2-11. Three-point bending results (Habel, K., and Gauvreau, P. (2008). “Response of ultra-high performance fiber reinforced concrete (UHPFRC) to impact and static loading.” *Cement and Concrete Composites*, Elsevier Ltd, 30(10), 938-946.)

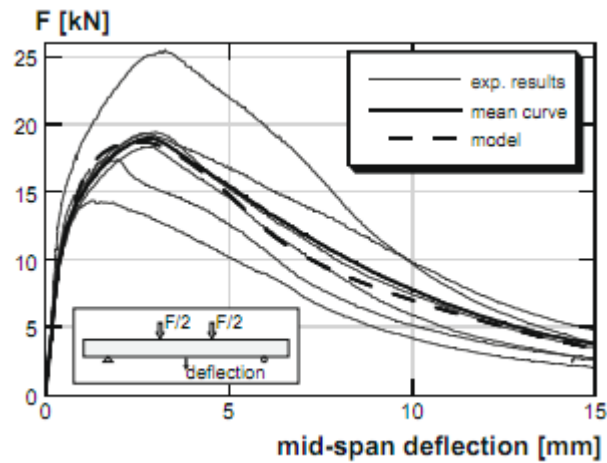


Figure 2-12. Four-point bending results (Habel, K., and Gauvreau, P. (2008). “Response of ultra-high performance fiber reinforced concrete (UHPFRC) to impact and static loading.” *Cement and Concrete Composites*, Elsevier Ltd, 30(10), 938-946.)

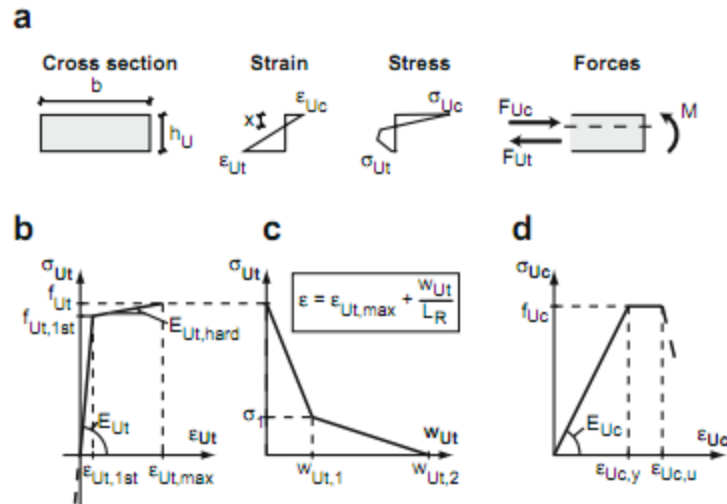


Figure 2-13. UHPFRC moment-curvature relationship (Habel, K., and Gauvreau, P. (2008). "Response of ultra-high performance fiber reinforced concrete (UHPFRC) to impact and static loading." *Cement and Concrete Composites*, Elsevier Ltd, 30(10), 938-946.)

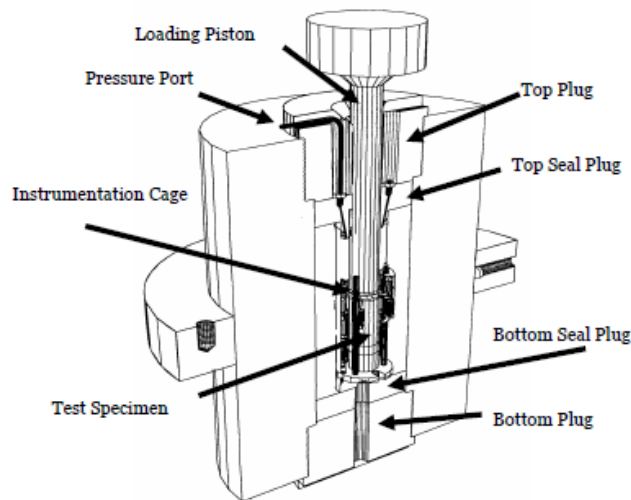


Figure 2-14. Triaxial pressure vessel (Williams, E. M., Graham, S. S., Reed, P. A., and Rushing, T. S. (2009). *Concrete With and Without Steel Fibers Geotechnical and Structures Laboratory Concrete With and Without Steel Fibers*. Vicksburg, MS.)

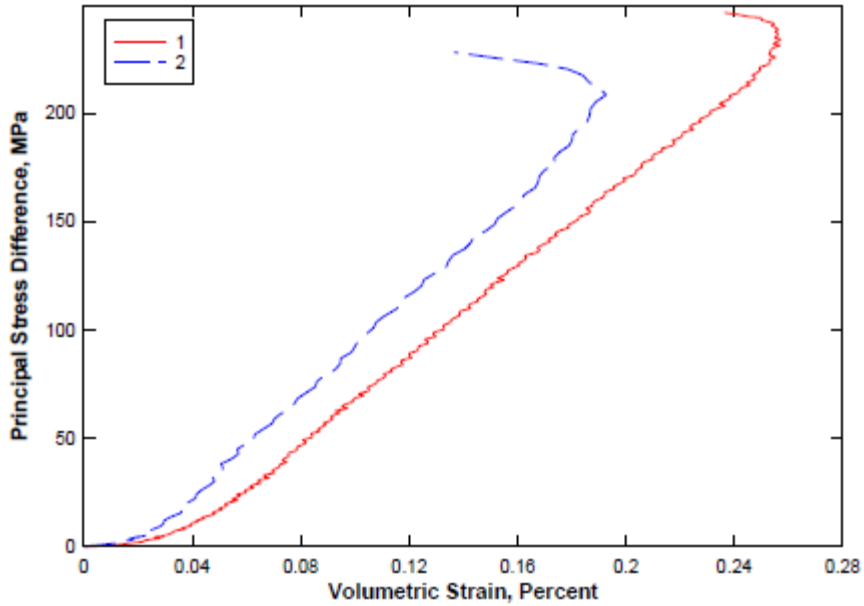


Figure 2-15. Stress-strain for unconfined compression (UC) test of Cor-Tuf1 (Williams, E. M., Graham, S. S., Reed, P. A., and Rushing, T. S. (2009). *Concrete With and Without Steel Fibers Geotechnical and Structures Laboratory Concrete With and Without Steel Fibers*. Vicksburg, MS.)

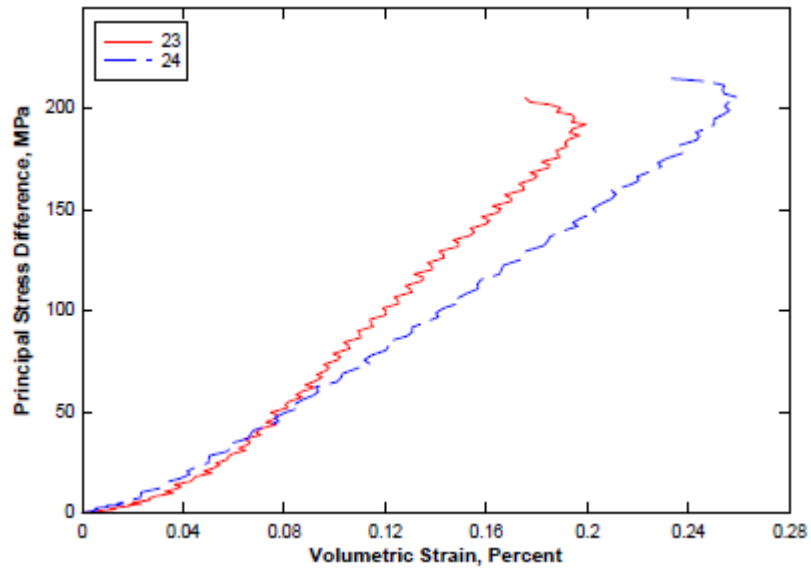


Figure 2-16. Stress-strain for UC test of Cor-Tuf2 (Williams, E. M., Graham, S. S., Reed, P. A., and Rushing, T. S. (2009). *Concrete With and Without Steel Fibers Geotechnical and Structures Laboratory Concrete With and Without Steel Fibers*. Vicksburg, MS.)

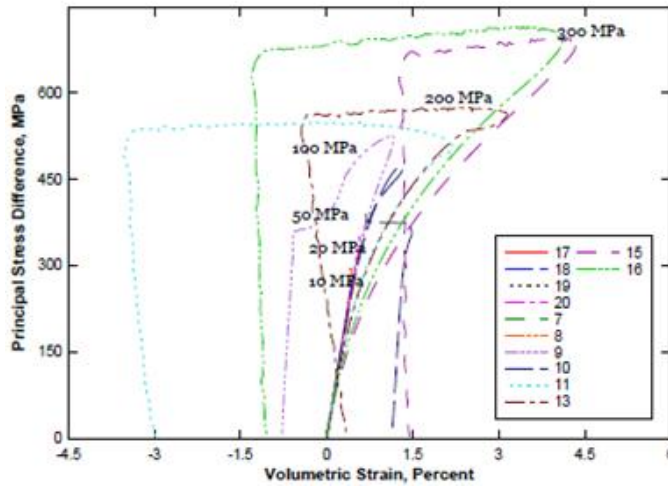


Figure 2-17. Triaxial compression (TxC) test results with confining pressures of 10MPa to 300 MPa (Cor-Tuf1) (Williams, E. M., Graham, S. S., Reed, P. A., and Rushing, T. S. (2009). *Concrete With and Without Steel Fibers Geotechnical and Structures Laboratory Concrete With and Without Steel Fibers*. Vicksburg, MS.)

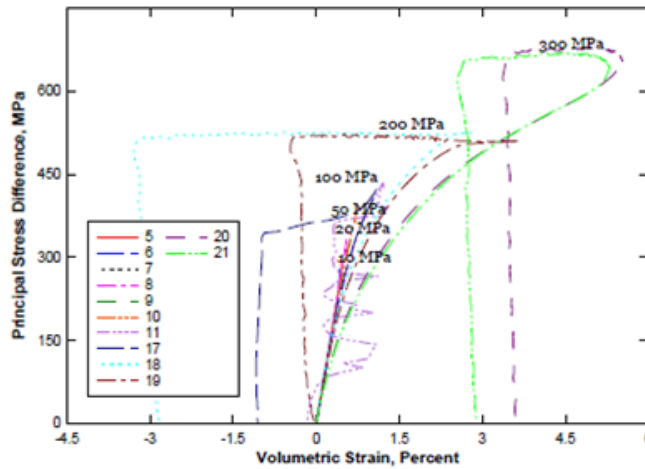


Figure 2-18. TxC test results with confining pressures of 10MPa to 300 MPa (Cor-Tuf2) (Williams, E. M., Graham, S. S., Reed, P. A., and Rushing, T. S. (2009). *Concrete With and Without Steel Fibers Geotechnical and Structures Laboratory Concrete With and Without Steel Fibers*. Vicksburg, MS.)

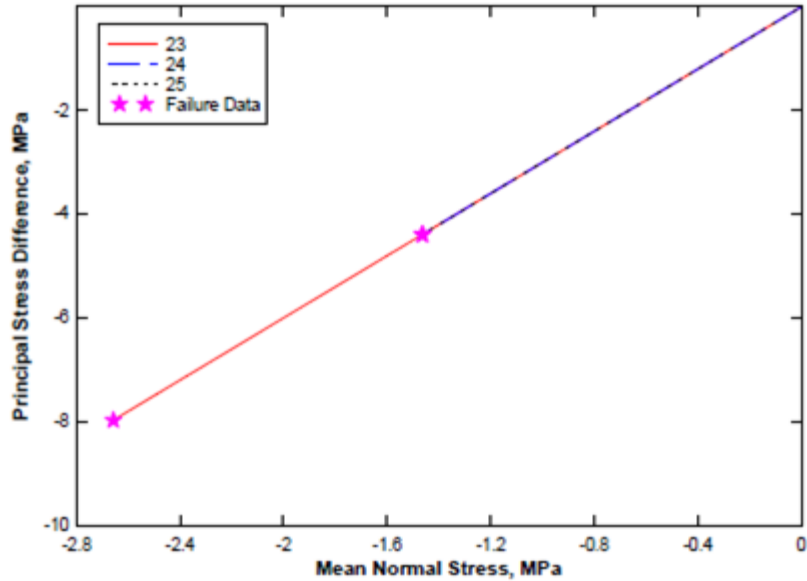


Figure 2-19. Stress path from direct pull tests for Cor-Tuf1 (Williams, E. M., Graham, S. S., Reed, P. A., and Rushing, T. S. (2009). *Concrete With and Without Steel Fibers Geotechnical and Structures Laboratory Concrete With and Without Steel Fibers*. Vicksburg, MS.)

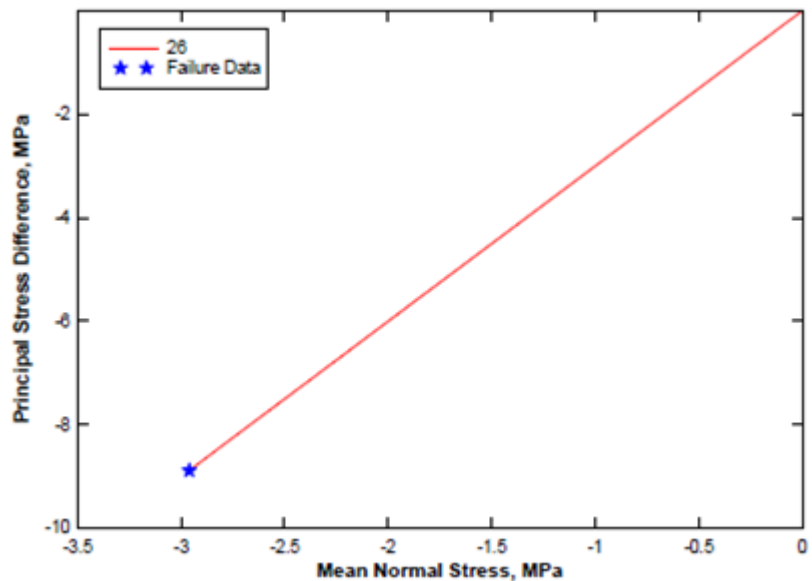


Figure 2-20. Stress path from direct pull tests for Cor-Tuf2 (Williams, E. M., Graham, S. S., Reed, P. A., and Rushing, T. S. (2009). *Concrete With and Without Steel Fibers Geotechnical and Structures Laboratory Concrete With and Without Steel Fibers*. Vicksburg, MS.)

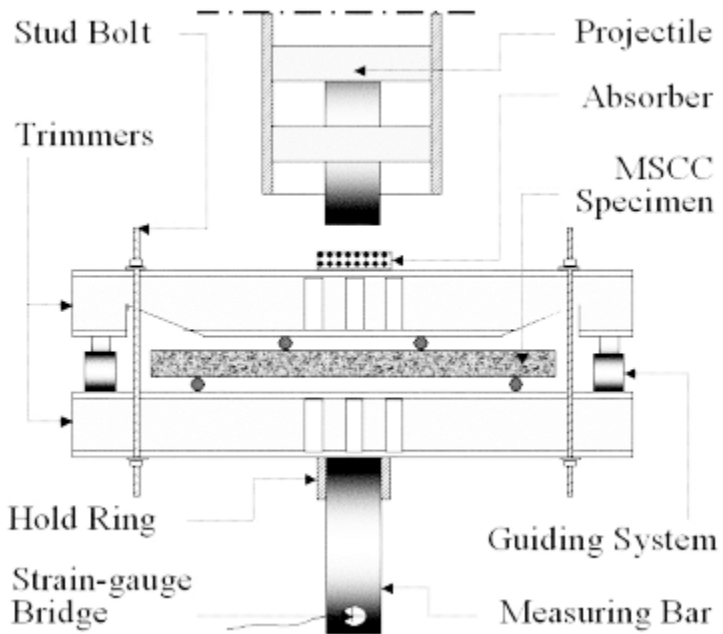


Figure 2-21. Block-bar device diagram (Parant, E., Rossi, P., Jacquelin, E., and Boulay, C. (2007). "Strain Rate Effect on Bending Behavior of New Ultra-High-Performance Cement-Based Composite." *ACI Materials Journal*, (104-M50), 458-463.)

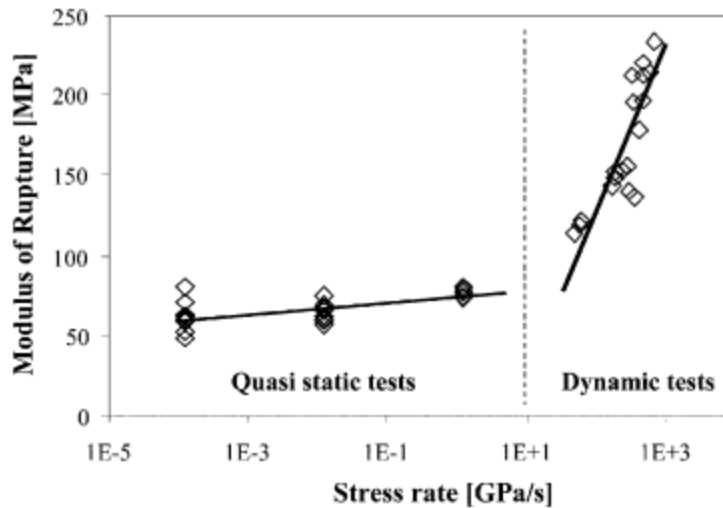


Figure 2-22. Modulus of Rupture-stress rate diagram (Parant, E., Rossi, P., Jacquelin, E., and Boulay, C. (2007). "Strain Rate Effect on Bending Behavior of New Ultra-High- Performance Cement-Based Composite." *ACI Materials Journal*, (104-M50), 458-463.)

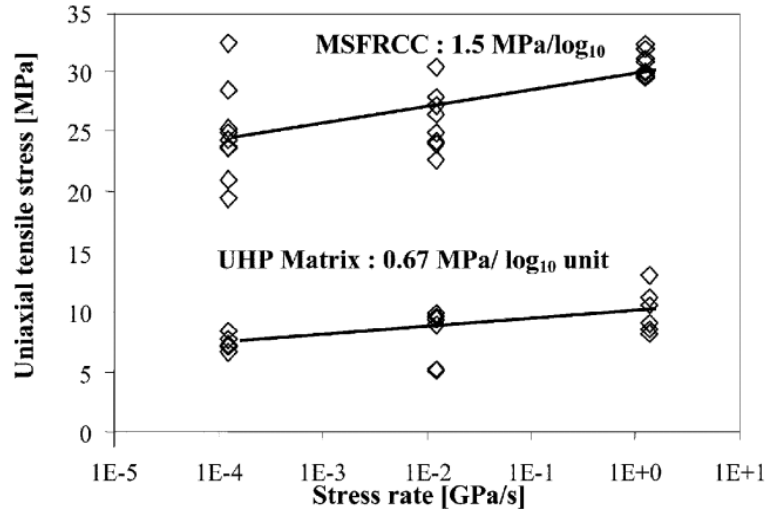


Figure 2-23. Uniaxial tensile stress vs. stress rate (Parant, E., Rossi, P., Jacquelin, E., and Boulay, C. (2007). "Strain Rate Effect on Bending Behavior of New Ultra-High- Performance Cement-Based Composite." *ACI Materials Journal*, (104-M50), 458-463.)

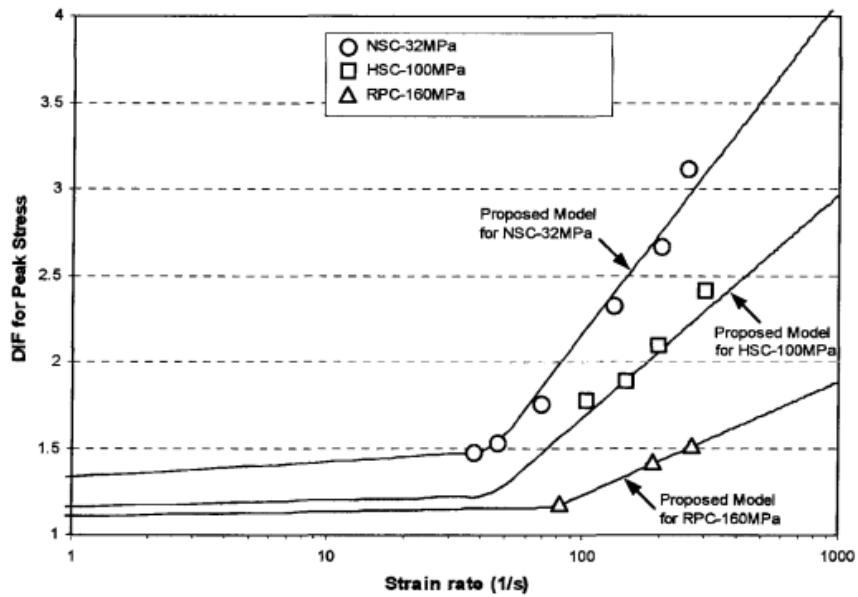


Figure 2-24. Dynamic increase factor (DIF) vs. strain rate (Ngo, T., Mendis, P., and Krauthammer, Ted. (2007). "Behavior of Ultrahigh-Strength Prestressed Concrete Panels Subjected to Blast Loading." *Journal of Structural Engineering, ASCE*, (November), 1582-1590.)

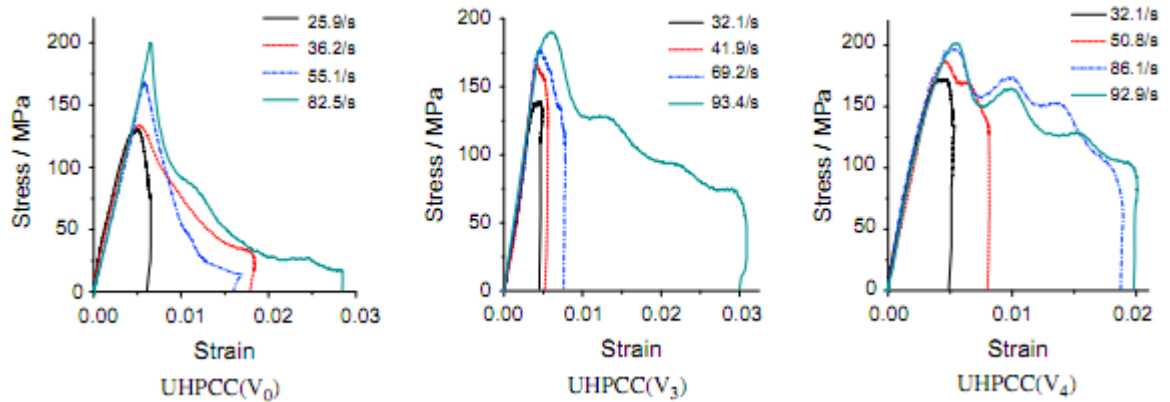


Figure 2-25. Stress-strain diagrams for split-hopkinson pressure bar (SHPB) tests with varying fiber percentages (Rong, Z., Sun, W., and Zhang, Y. (2010). "Dynamic compression behavior of ultra-high performance cement based composites." *International Journal of Impact Engineering*, Elsevier Ltd, 37(5), 515-520.)



Figure 2-26. SHPB specimens post-test (Rong, Z., Sun, W., and Zhang, Y. (2010). "Dynamic compression behavior of ultra-high performance cement based composites." *International Journal of Impact Engineering*, Elsevier Ltd, 37(5), 515-520.)

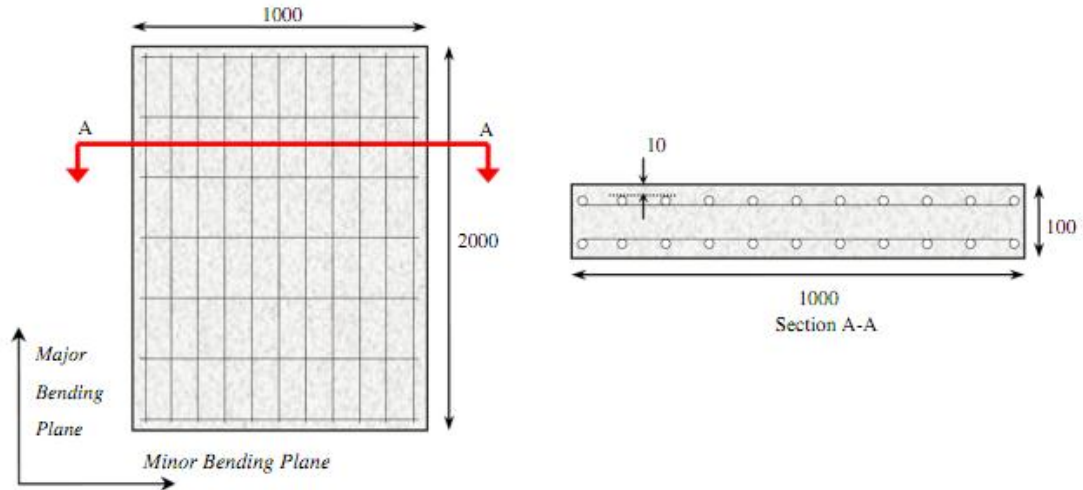


Figure 2-27. Reinforcement geometry for blast slabs (Wu, C., Oehlers, D. J., Rebstrost, M., Leach, J., and Whittaker, a. S. (2009). "Blast testing of ultra-high performance fibre and FRP-retrofitted concrete slabs." *Engineering Structures*, Elsevier Ltd, 31(9), 2060-2069.)



Figure 2-28. Cracking in NRC-3 slab (top); Cracking in UHPFC slab (bottom) (Wu, C., Oehlers, D. J., Rebstrost, M., Leach, J., and Whittaker, a. S. (2009). "Blast testing of ultra-high performance fibre and FRP-retrofitted concrete slabs." *Engineering Structures*, Elsevier Ltd, 31(9), 2060-2069.)

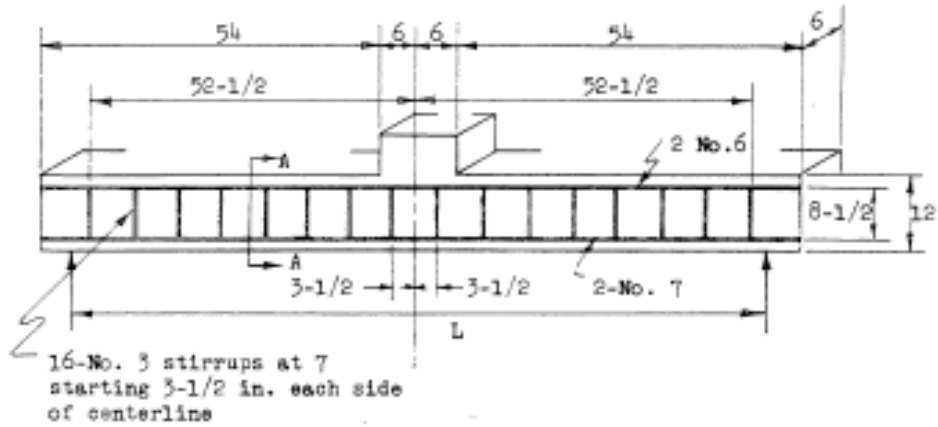


Figure 2-29. Feldman and Siess reinforced concrete beam design, front view (Feldman, A., and Siess, C. P. (1956). *Investigation of Resistance and Behavior of Reinforced Concrete Members Subjected to Dynamic Loading - Part I.* Urbana, Illinois.)

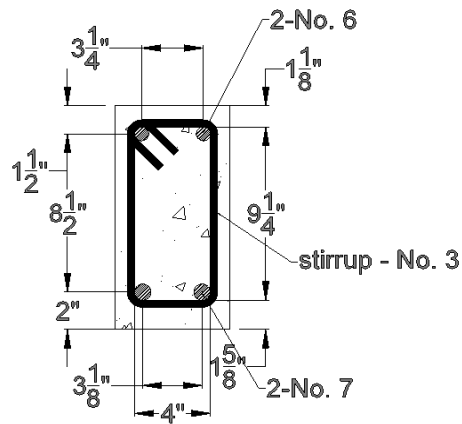


Figure 2-30. Feldman and Siess beam 1-f and 1-h, section view (Adapted from Feldman, A., and Siess, C. P. (1956). *Investigation of Resistance and Behavior of Reinforced Concrete Members Subjected to Dynamic Loading - Part I.* Urbana, Illinois.)

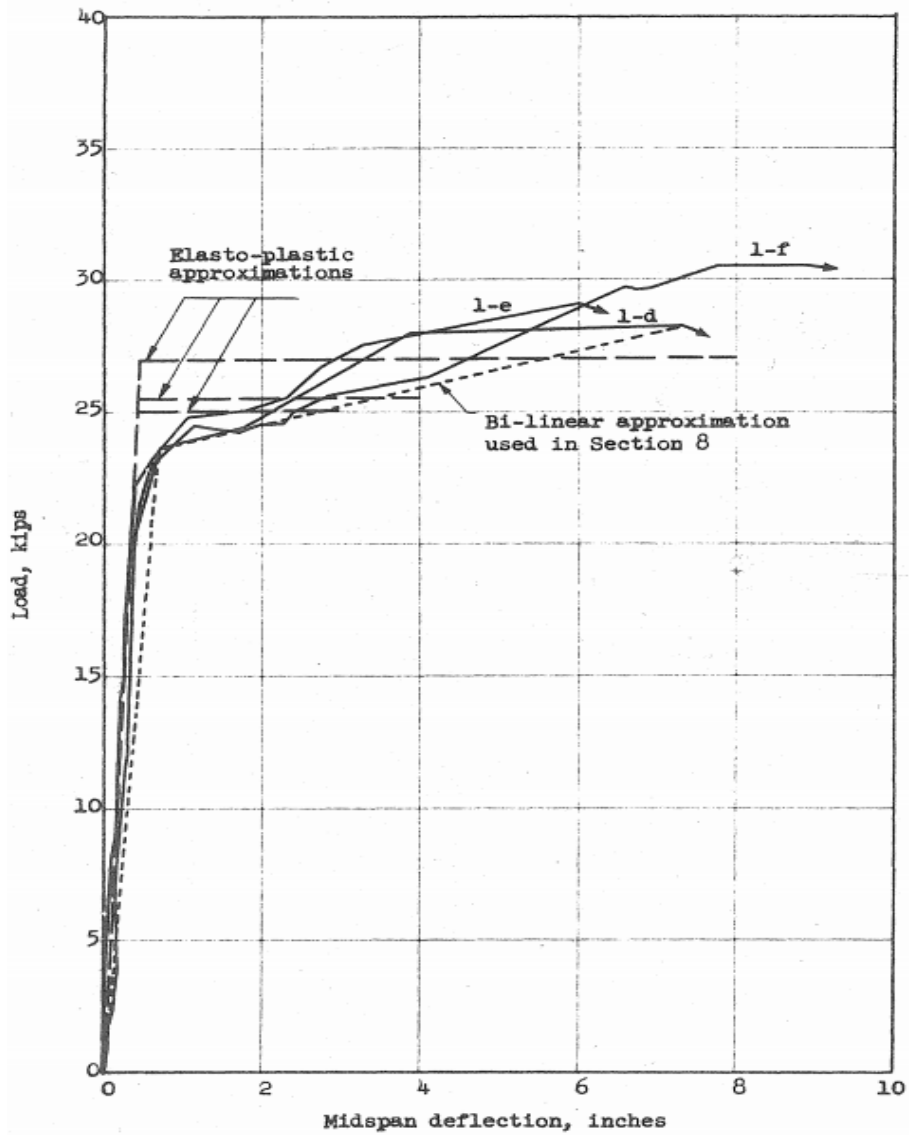


Figure 2-31. Load vs. Midspan Displacement for Feldman and Siess static tests (Feldman, A., and Siess, C. P. (1958). *Investigation of Resistance and Behavior of Reinforced Concrete Members Subjected to Dynamic Loading - Part II*. Urbana, Illinois.)

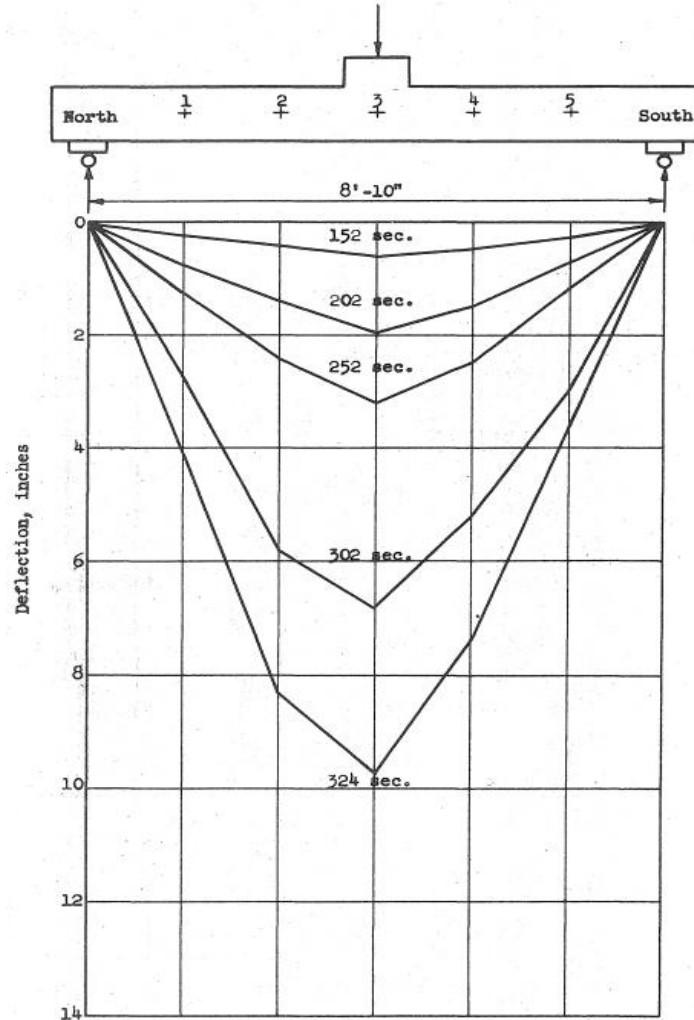


Figure 2-32. Load time-history for Feldman and Siess Beam 1-f (Feldman, A., and Siess, C. P. (1958). *Investigation of Resistance and Behavior of Reinforced Concrete Members Subjected to Dynamic Loading - Part II*. Urbana, Illinois.)

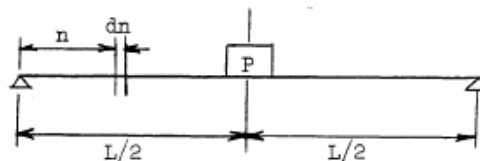


Figure 2-33. Load-beam system for single degree of freedom (SDOF) calculations (Feldman, A., and Siess, C. P. (1956). *Investigation of Resistance and Behavior of Reinforced Concrete Members Subjected to Dynamic Loading - Part I*. Urbana, Illinois.)

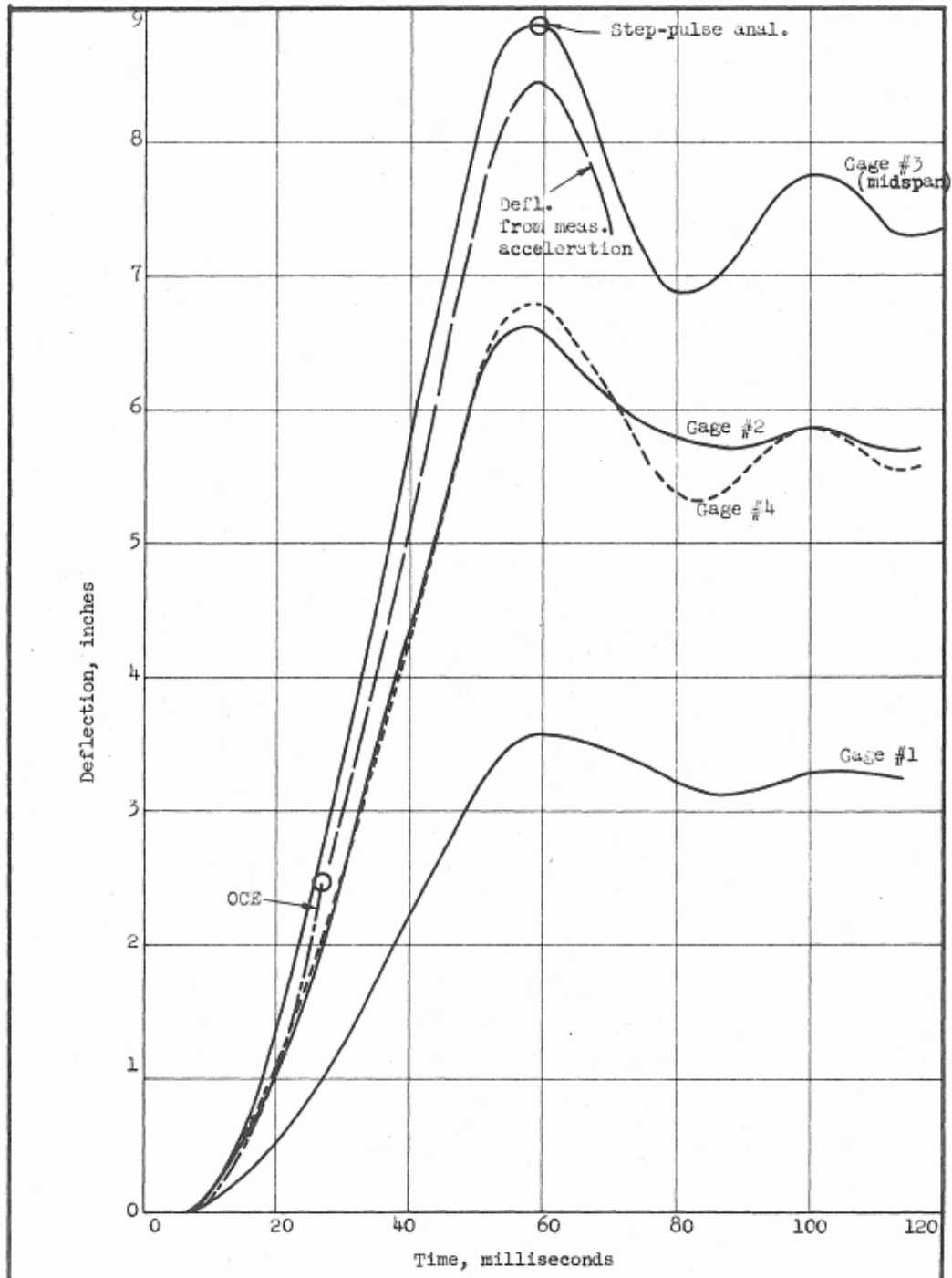


Figure 2-34. Displacement vs. time for impact of Beam 1H (Feldman, A., and Siess, C. P. (1958). *Investigation of Resistance and Behavior of Reinforced Concrete Members Subjected to Dynamic Loading - Part II*. Urbana, Illinois.)

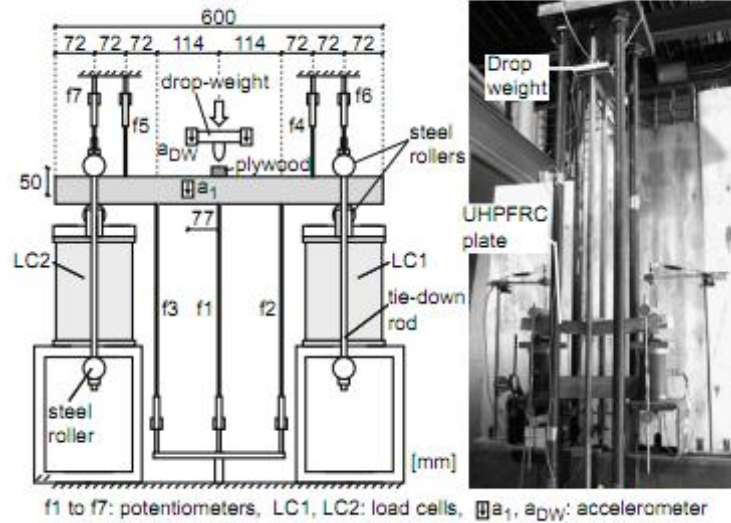


Figure 2-35. Habel and Gauvreau drop hammer setup (Habel, K., and Gauvreau, P. (2008). "Response of ultra-high performance fiber reinforced concrete (UHPFRC) to impact and static loading." *Cement and Concrete Composites*, Elsevier Ltd, 30(10), 938-946.)

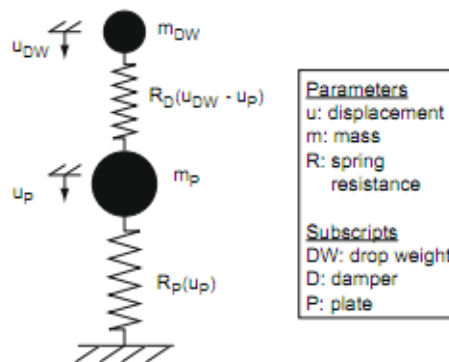


Figure 2-36. Two mass-spring model (Habel, K., and Gauvreau, P. (2008). "Response of ultra-high performance fiber reinforced concrete (UHPFRC) to impact and static loading." *Cement and Concrete Composites*, Elsevier Ltd, 30(10), 938-946.)

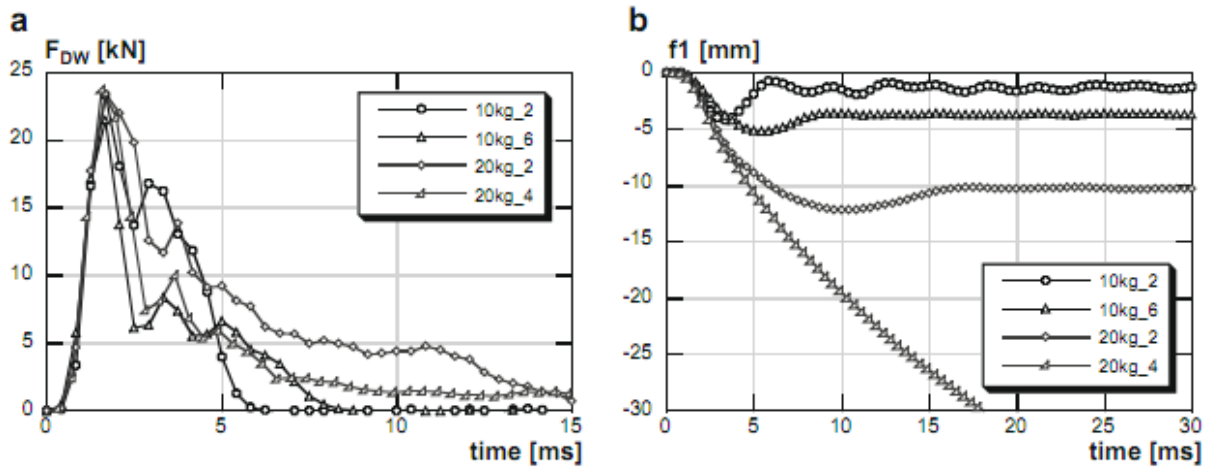


Figure 2-37. (a) Drop weight force vs. time; (b) Deflection vs. time (Habel, K., and Gauvreau, P. (2008). "Response of ultra-high performance fiber reinforced concrete (UHPFRC) to impact and static loading." *Cement and Concrete Composites*, Elsevier Ltd, 30(10), 938-946.)

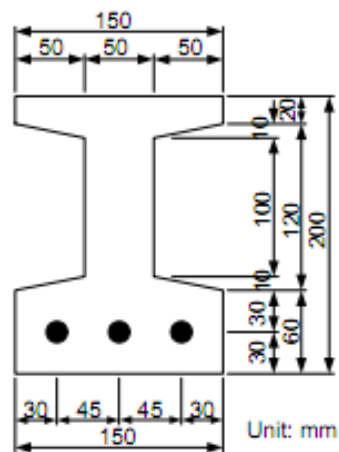


Figure 2-38. Fujikake et al. reactive powder concrete (RPC) beam cross section (Fujikake, K., Senga, T., Ueda, N., Ohno, T., and Katagiri, M. (2006). "Study on Impact Response of Reactive Powder Concrete Beam and Its Analytical Model." *Journal of Advanced Concrete Technology*, 4(1), 99-108.)

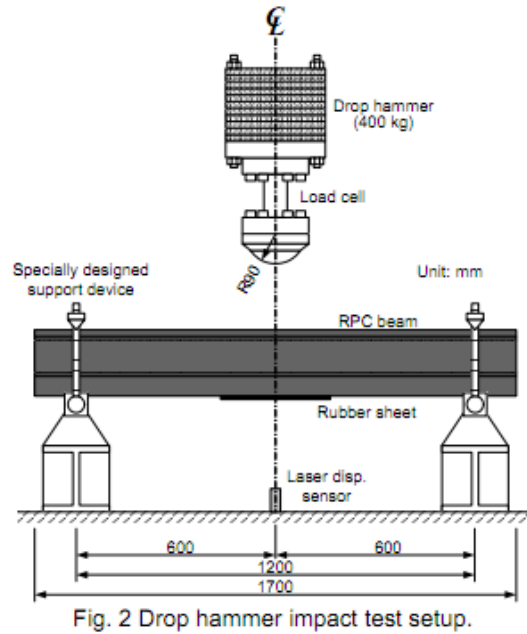


Figure 2-39. Fujikake et al. drop hammer test setup (Fujikake, K., Senga, T., Ueda, N., Ohno, T., and Katagiri, M. (2006). "Study on Impact Response of Reactive Powder Concrete Beam and Its Analytical Model." *Journal of Advanced Concrete Technology*, 4(1), 99-108.)

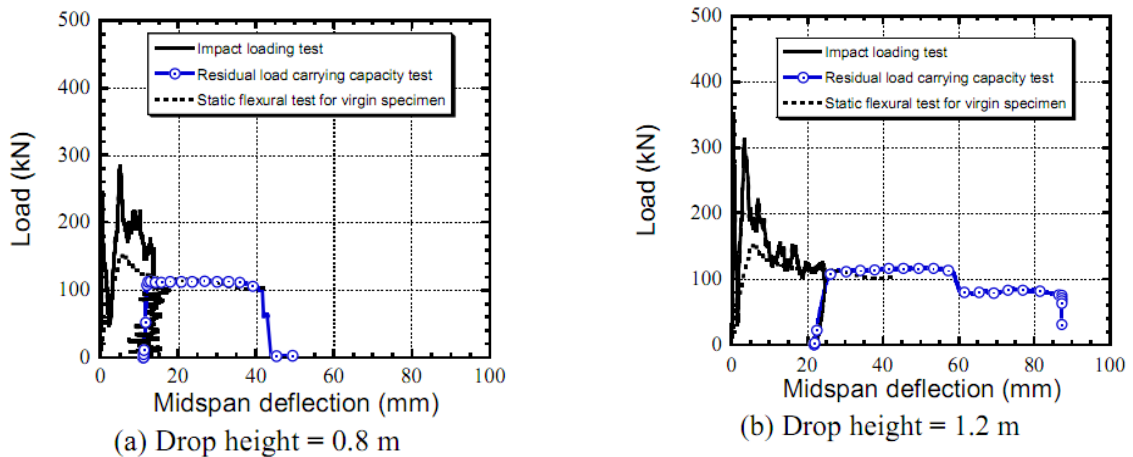


Figure 2-40. (a) Fujikake et al. drop hammer test from 0.8 m; (b) Drop from 1.2 m (Fujikake, K., Senga, T., Ueda, N., Ohno, T., and Katagiri, M. (2006). "Study on Impact Response of Reactive Powder Concrete Beam and Its Analytical Model." *Journal of Advanced Concrete Technology*, 4(1), 99-108.)

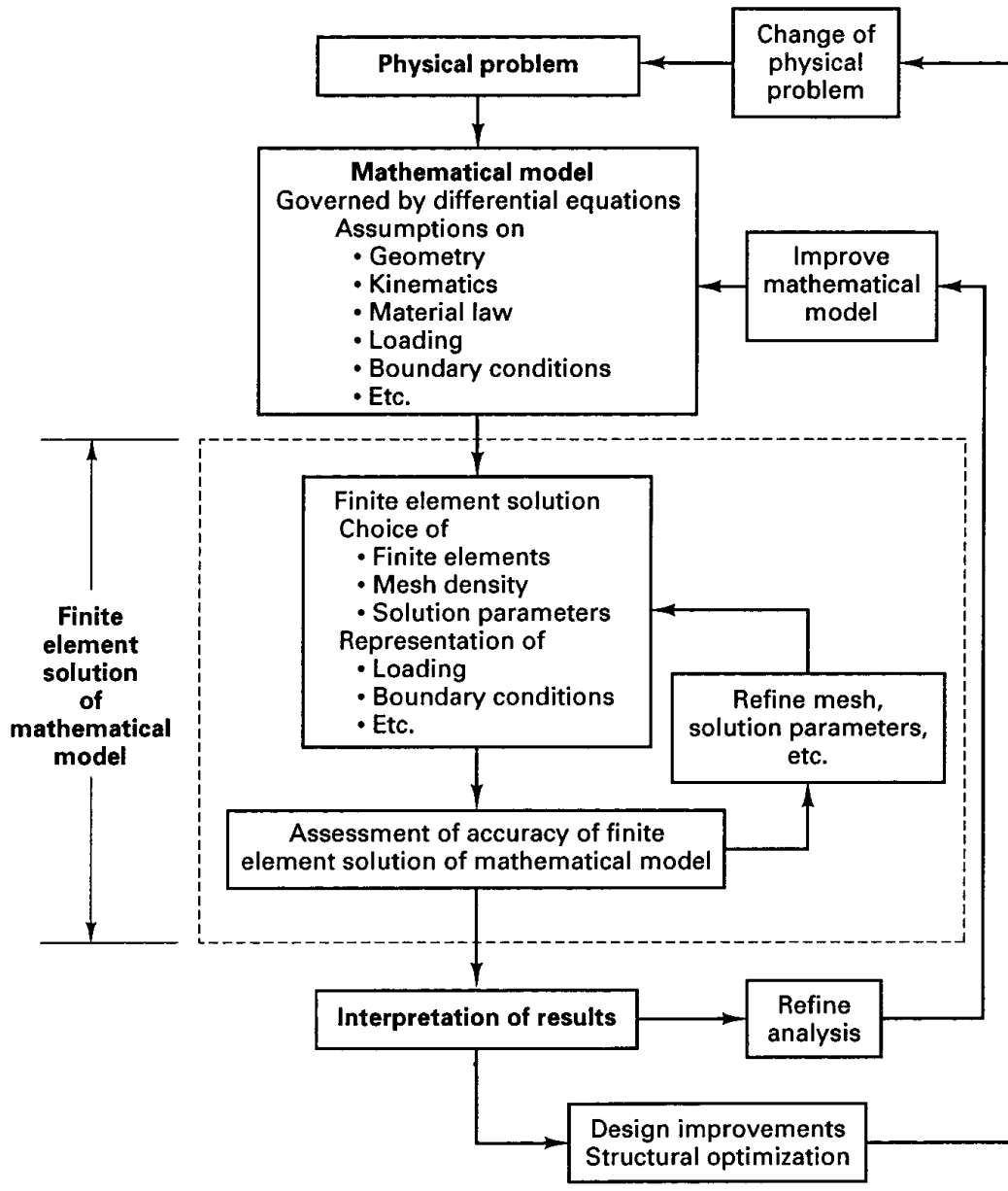


Figure 2-41. Flow process for a physical problem solved with finite element analysis (Bathe, K. (1995). *Finite Element Procedures*. Prentice-Hall, Upper Saddle River, New Jersey.)

CHAPTER 3 EXPERIMENTAL INVESTIGATION

3.1 Introduction

The majority of the experimental portion of this project will take place after the completion of this paper; however, the magnitude of the experiments will be based on the predictions made during the numerical analysis discussed later on. The static beam test results, which have been obtained for all 6 beam series, will be presented in conjunction with the simulated results along with discussion. The following is a description of the specimens and equipment that will be utilized to statically and dynamically characterize the properties of Cor-Tuf. All of the NSC and Cor-Tuf beam and cylinder specimens were mixed, poured and cast from the same mix batches to ensure uniformity during testing. The data gathered from these experiments will be utilized to calibrate the prediction models and create accurate material models.

3.2 Test Specimens

3.2.1 Cylinders For Static Tests

The Geotechnical and Structures Laboratory, ERDC, US Army, was responsible for specimen preparation and static testing of all 6 in diameter by 12 in height specimens. ERDC retained 9 of these cylinders to statically test as none of the equipment at the University of Florida can generate enough force to test the UHPC cylinders. These cylinders are indicated in Table 3-1. The Center for Infrastructure Protection and Physical Security at the University of Florida (CIPPS) will test the 4 in diameter by 8 in height (4x8) specimens locally to accelerate the testing process. For static testing purposes a total of 9 - 4x8 cylinders will be produced by ERDC and tested. The specimen quantities and materials for static tests are summarized in Table 3-2.

3.2.2 Cylinders For Dynamic Tests

The cylinders for dynamic testing, also prepared by ERDC, will be tested at CIPPS. ERDC will cast, in addition to the static cylinders already mentioned, 9 – 4 in diameter by 8 in tall cylinders for impact testing as shown in Table 3-3. Additionally, 99 cylinders will be cast in addition to the static cylinders in the 6 in diameter by 12 in height size, see Table 3-4. The variation in sizes will allow for a first impression of any size effects in Cor-Tuf.

3.2.3 Beams For Static and Impact Testing

In addition to cylinder testing, a series of beams constructed of NSC as well as both variations of Cor-Tuf will be tested both statically and dynamically at CIPPS. The Geotechnical and Structures Laboratory at ERDC will also cast the beams. The beams will be cast from the same concrete batches as the cylinders and subjected to the same curing process. This will ensure that the cylinders can provide specific characteristic curves to the material used in the beams.

Typical beam dimensions, reinforcement details, and cross sections are shown in Figure 3-1 and described in Table 3-5 and Table 3-6. All reinforcement except the B5 series shall be Grade 60. The B5 series will be made of Cor-Tuf1 without reinforcing bars. The B2 and B6 series will only contain longitudinal reinforcement, no shear reinforcement (stirrups). This specimen design was created after the discovery of the findings in Graybeal (2005) which showed that UHPC with fibers reinforcement may not require shear reinforcement. In each specimen, a 1 in thick steel plates shall be placed at support points and ½ in thick steel plate at load point. The plates should help avoid any issues of localized crushing. Strain gages will be placed along both of the tension (bottom) reinforcement bars at 18 in spacing (3 per reinforcing bar) for each beam

specimen before the casting of concrete, and the strain gage calibration data will be provided to CIPPS including the conversion to strain and the initial bias. The six strain gages will be placed at each of the quarter-spans (two per end per bar) as well as at the midspan (two) of the bottom rebar.

3.3 Testing Equipment and Setup

3.3.1 Static Testing Equipment For Cylinders

The first set of static tests were performed on cylinders measuring 4" x 8" and will be performed locally at the University of Florida in Weil Hall using a Gilson MC-250CS compression testing unit, shown in Figure 3-4. The capacity of this machine is 350 klf however it does not have any output for the load applied and therefore will not be used for the 4" x 8" Cor-Tuf cylinders. Additionally, the 6" x 12" cylinders require over 700 kips of force and will need to be tested at FDOT. The first tests conducted with the 4" x 8" cylinders were not from the beam concrete batches and were merely for calibration purposes. The cylinders were not outfitted with strain gages, subsequent tests will contain significant amounts of data and will measure the post-peak behavior of all three materials for use in accurate modeling of the cylinders and beams.

The 4" x 8" and 6" x 12" cylinder tests will be conducted on 3 cylinders of each material at FDOT. If possible, the tests will be carried out with the same strain gage pattern. The tests will help calibrate the models as well as create a control group for the dynamic tests. The dynamic tests will attempt to use the same strain gage patterns as well.

3.3.2 Static Testing Equipment For Beams

Static testing of beams will be accomplished with the use of an Enerpac RC-5013 hydraulic jack controlled by an Enerpac P-462 hand pump with an oil pressure gauge.

The load will be slowly applied to the beam in 1-2 kip increments to ensure that the failure can be properly captured. In between each increment, loading will be paused and the beam will be checked for cracking and any other irregularities. The data acquisition (DAQ) for this portion of the testing will be recorded using a National Instruments USB-6218 capable of recording 32 analog channels of 16 bits at 250 kS/s (kilosamples/second). A special program was created to run the NI DAQ that allowed for sampling of each signal at 100-1000 Hz during loading, and then at a rate of 0.5 Hz while hand measurements were being taken.

3.3.3 Dynamic Testing Equipment For Cylinders

Dynamic testing of cylinders will be carried out using the CIPPS drop hammer shown in Figure 3-6. Table 3-7 describes the specific measurements and capabilities of the drop hammer. The hammer can release its maximum weight of approximately 600 lbs, when outfitted with a load cell and striker plate, from a height of over 16 feet. Drops from this height, depending on the response of the specimen, can create forces exceeding 1000 kips, although for no longer than 0.5-2 milliseconds. However, despite this great force, the possibility exists that it may not be capable of failing all of the test specimens, especially the cylinders. For this reason, extra load plates have been manufactured to create a higher impact load. This will be discussed further in the chapter on numerical predictions. An important aspect to note about the hammer is its braking system. The brakes are designed to deploy after the load cell reaches a certain load. The brakes will fire and as the load cart is rebounding off of the beam or cylinder, stop it from contacting the specimen a second time. In this way, any specimen that has been subjected to an impact load can be tested further if it has not failed.

3.3.4 Dynamic Testing Equipment For Beams

The beams will be tested in much the same manner as the cylinder using the impact drop hammer. The beams will be supported on each end with a stand that is attached to the strong floor of the laboratory. Each stand is constructed with a roller to allow for simply supported conditions as well as a load cell mounted below the roller to capture the reactions from the tests. An example of the supports can be seen in

3.4 Instrumentation

The data from testing of the cylinders and beams will be both thorough and complex. The data acquisition system utilized for the static and dynamic testing of beams, and the dynamic testing of cylinders is shown in Figure 3-7. The system consists of a High Techniques HT600 to capture the voltages of all incoming signals; an OASIS 2000 signal conditioner to condition raw voltage and supply voltage to strain gauges and load cells; and a rack computer to save all of the incoming data as well as monitor the tests in progress. The HT600 contains 64 channels that read from BNC cables. Each channel is read independently in order for the data to be read continuously. The channels can each hold up to 8 million points that can be read up to a frequency of 2 million points per second. The OASIS 2000 is setup with 10 boards capable of regulating the voltage to load cells and strain gages. Additionally, it is set up with 2 boards that are capable of supplying current to accelerometers and other sensors that require it. The OASIS 2002 is capable of outputting 5, 10 and 15 V at gains of 1-1000.

The instrumentation that will be monitored by the data acquisition systems includes all of the following: strain gages of varying sizes on both concrete and steel inside of the beams, accelerometers, displacement gauges, velocity sensors and load

cells ranging from 50 kips to 2000 kips. The data from these inputs can be sampled at frequencies of up to 2 MHz which will be vital for dynamic tests that will not exceed 5 ms. The tests will also be captured by both normal and high speed video. The high speed cameras utilized will be a Memrecam fx K3 high speed camera as well as a Phantom v5.2. The Memrecam is capable of capturing footage at 10,000 fps at a resolution of 1280 x 96. The Phantom camera is capable of capturing video at 148,000 fps at a resolution of 96 x 8 (although at this resolution the captured footage will likely not be useful).

Table 3-1. 6" x 12" cylinder quantities and material properties for static testing

Series	Quantity	Size	Material
1S-6x12	3	6"x12"	NSC ($f'_c = 3500$ psi)
2S-6x12	3	6"x12"	Cor-Tuf with fibers (Cor-Tuf1)
3S-6x12	3	6"x12"	Cor-Tuf without fibers (Cor-Tuf2)

Table 3-2. 4" x 8" cylinder quantities and material properties for static testing

Series	Quantity	Size	Material
1S-4x8	3	4"x8"	NSC ($f'_c = 3500$ psi)
2S-4x8	3	4"x8"	Cor-Tuf with fibers (Cor-Tuf1)
3S-4x8	3	4"x8"	Cor-Tuf without fibers (Cor-Tuf2)

Table 3-3. 4" x 8" cylinder quantities and material properties for impact testing

Series	Quantity	Material
1D-4x8*	3	NSC ($f'_c = 3500$ psi)
2D-4x8*	3	Cor-Tuf with fibers (Cor-Tuf1)
3D-4x8*	3	Cor-Tuf without fibers (Cor-Tuf2)

*Use the same concrete, as for the cylinders in Table 3-1 and Table 3-2

Table 3-4. 6" x 12" cylinder quantities and material properties for impact testing

Series	Quantity	Material
1D-6x12*	33	NSC ($f'_c = 3500$ psi)
2D-6x12*	33	Cor-Tuf with fibers (Cor-Tuf1)
3D-6x12*	33	Cor-Tuf without fibers (Cor-Tuf2)

*Use the same concrete, as for the cylinders in Table 3-1 and Table 3-2

Table 3-5. Beam quantities and materials for static and impact testing

Series	Quantity	Concrete	Materials		Details
			Longitudinal Reinforcement	Shear Reinforcement	
B1	6	NSC ($f'_c = 3500$ psi)	Top 2-#6 Bottom 2#7	#3 @ 5"	Fig.1
B2	2	NSC ($f'_c = 3500$ psi)	Top 2-#6 Bottom 2#7	No shear Reinforcement	Fig. 2
B3	6	Cor-Tuf with fibers (Cor-Tuf1)	Top 2-#6 Bottom 2#7	#3 @ 5"	Fig. 1
B4	6	Cor-Tuf without fibers (Cor-Tuf2)	Top 2-#6 Bottom 2#7	#3 @ 5"	Fig. 1
B5	6	Cor-Tuf with fibers (Cor-Tuf1)	No longitudinal reinforcement	No shear Reinforcement	Fig. 3
B6	6	Cor-Tuf with fibers (Cor-Tuf1)	Top 2-#6 Bottom 2#7	No shear Reinforcement	Fig. 2

Table 3-6. Static and impact testing matrix per material

Test	Quantity	Description
Static	1	Static displacement controlled test for obtaining the resistance function.
Impact	1	Multiple drops with increasing drop heights in on the same specimen till failure.
Impact	3	Single drop height high enough to cause failure in the specimen. (Not carried out for B2)

*With the exception of series B2, all series will have one extra beam as a precaution.

Table 3-7. Center for Infrastructure Protection and Physical Security (CIPPS) Drop Hammer Specifications

Drop Hammer Specifications	
Rail Cart Weight	129.46 lbs
Adapter Plates Total	365.00 lbs
Striker Weight	Varying
Drop Tower Height	195.84 in
Minimum Drop Height	12 in

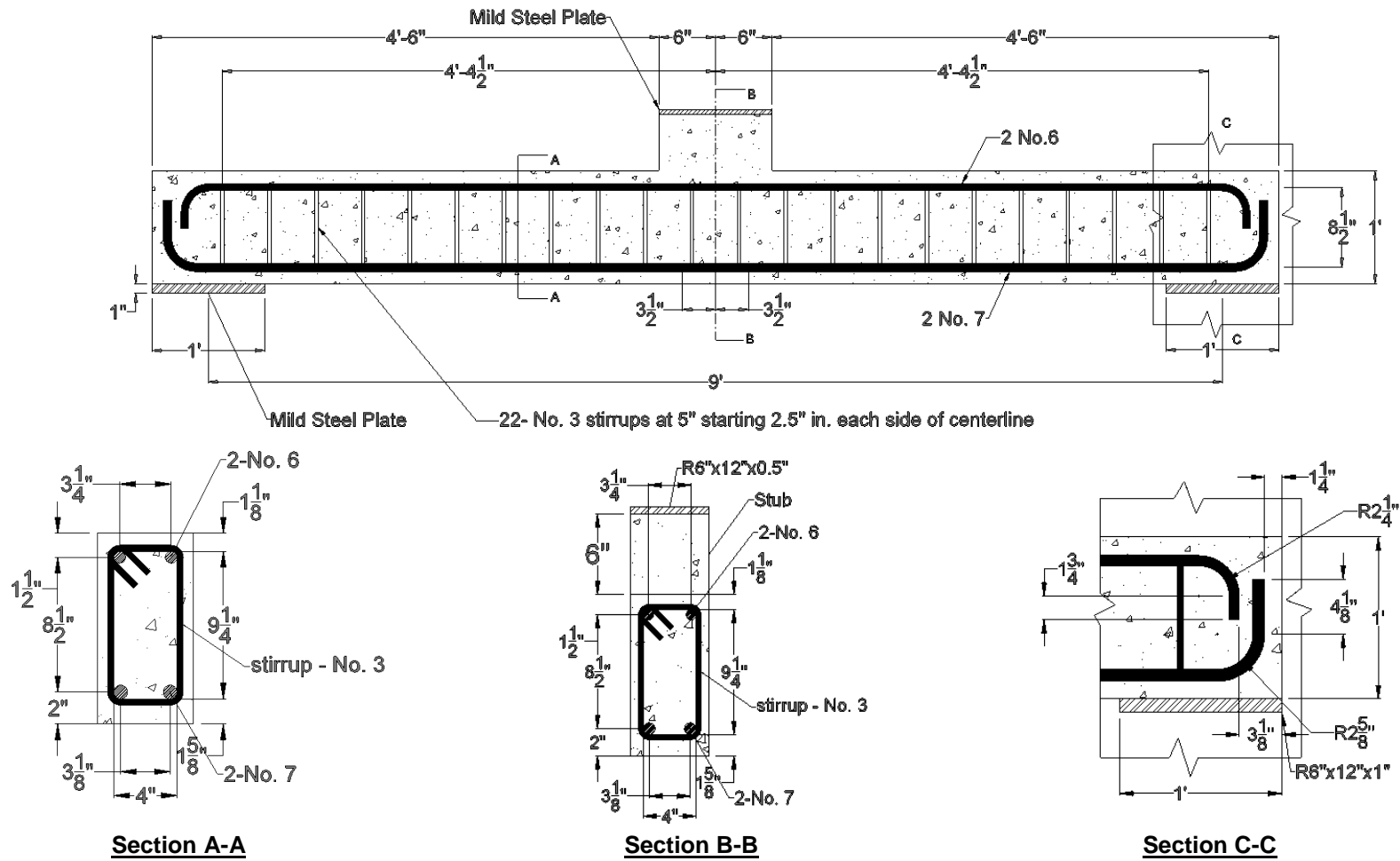


Figure 3-1. Beam dimensions and details for series B1, B3 and B4 (Table 3-5)

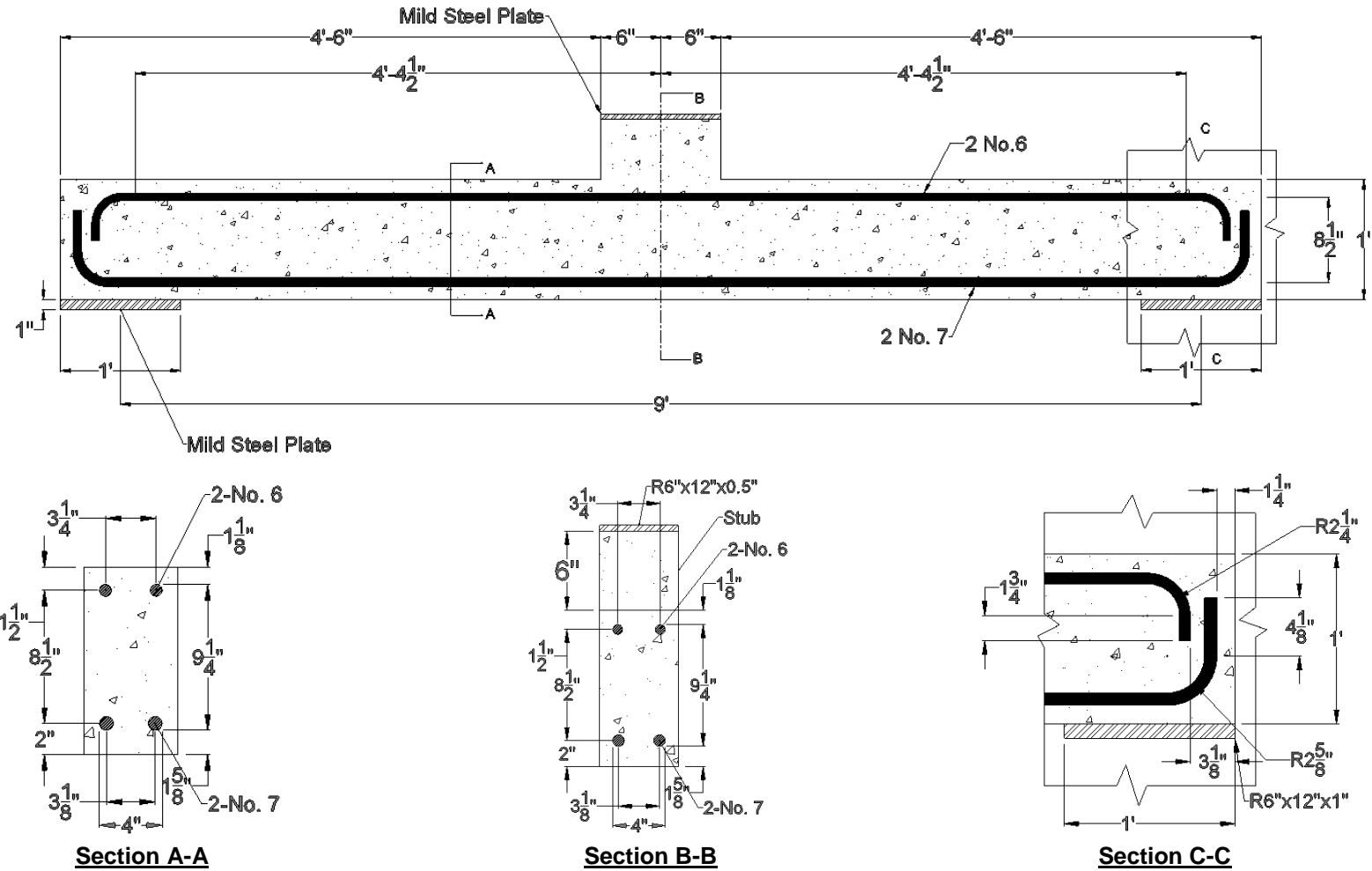
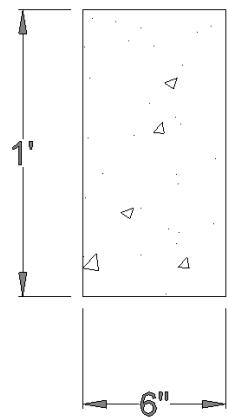
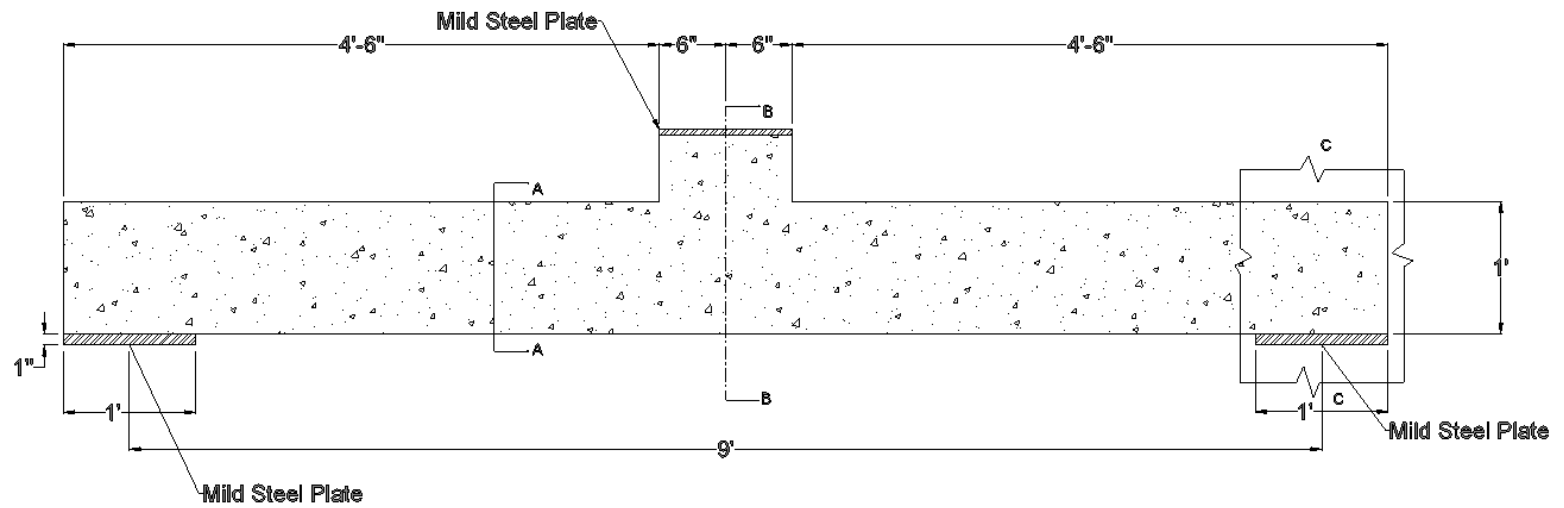
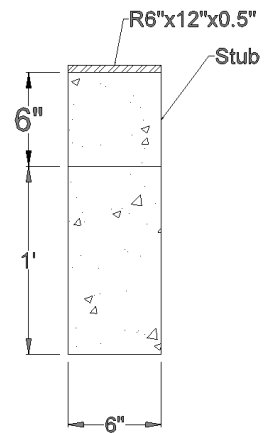


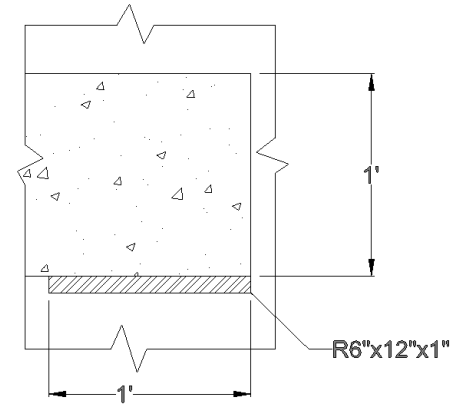
Figure 3-2. Beam dimensions and details for series B2 and B6 (Table 3-5)



Section A-A



Section B-B



Section C-C

Figure 3-3. Beam dimensions and details for series B5 (Table 3-5)



Figure 3-4. Gilson MC-250CS Compression Testing Machine



Figure 3-5. Enerpac RC-5013 hydraulic jack for static testing



Figure 3-6. Center for Infrastructure Protection Physical Security (CIPPS) Drop Hammer

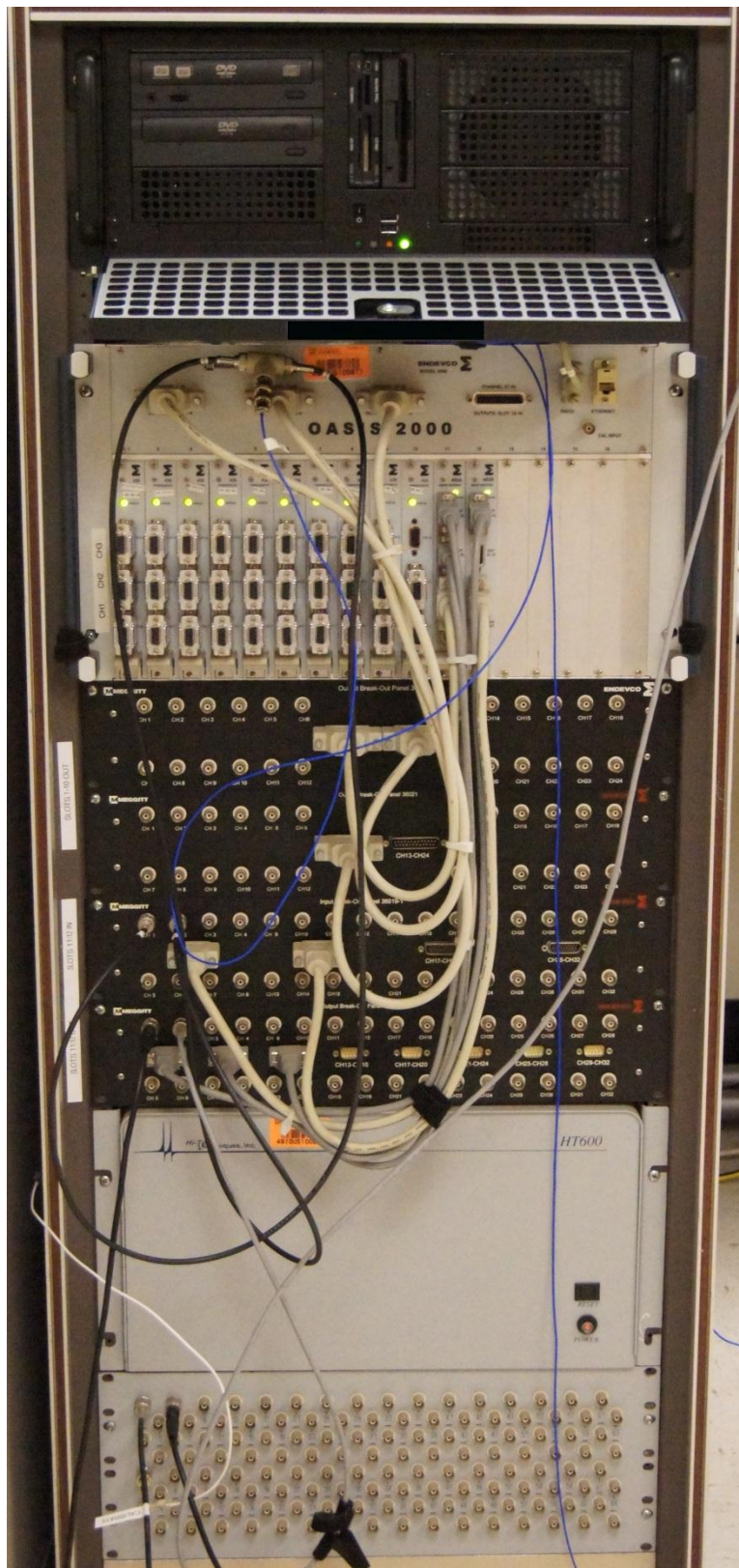


Figure 3-7. CIPPS Data Acquisition System



Figure 3-8. Supports for beam testing

CHAPTER 4 MODEL VALIDATION

4.1 Introduction

The Feldman and Siess impact experiments (Feldman and Siess 1956, 1958) were utilized as the validation cases for the numerical modeling performed in this project. The beam design created by Feldman and Siess, and replicated for these experiments, is well suited due to both the size of the beams as well as the reinforcement detail utilized. While modifications in the type of steel, and strength of the concrete and steel were made for the final beams to be tested, the overall design and shape remained the same. In addition the beams having the desired properties for testing, the documentation of the experimental work also allowed for accurate model validation.

This chapter contains the model validation work that was completed and utilized to create the predictions for the CIPPS beam specimens that will be tested. The following items will be covered in this chapter: material models, inputs for Abaqus parameters, modeling details and the results of the models compared to experimental results. While the models did not fully capture the results of the Feldman and Siess experiments, the overall behavior of each experiment was properly presented in the models.

4.2 Material Models

A variety of material models exists for both concrete and steel depending on both the types of concrete and steel and the interaction between the two. For the purposes of the numerical solutions shown here, the modified Hognestad parabola (MacGregor and Wight 2005) concrete model was utilized for concrete in compression. The Hognestad parabola utilizes the compressive strength from cylinder tests as well as common

parameters for normal strength concrete to create a characteristic material curve. Modifications were made to the curve to accommodate the methodologies of Abaqus. The tension portion of the concrete model was based on the Hsu model (Hsu 1993) for concrete in tension. This model was chosen as it closely follows the ACI recommendations (American Concrete Institute 2011). The steel model was based on the Park and Paulay model described in Park and Paulay (1975). These models have been tested and utilized in a variety of theses, the most recent being that of Koh (2011), the material models work well for both static and dynamic scenarios.

4.2.1 Modified Hognestad Parabola

The modified Hognestad parabola utilizes the compression results from a uniaxial compression test of plain concrete cylinders (6 inch diameter by 12 inch height) to create material curves. Hognestad created generalized material curves (MacGregor and Wight 2005) for varying compressive strengths shown in Figure 4-1. The modified Hognestad stress-strain curve, shown in Figure 4-2, is designed for use with concrete mixes that do not exceed 6000 psi. In the case of Feldman and Siess the mixes reached up to 6600 psi but this was deemed within range of the curves predictions. The curve begins with a second degree parabola that peaks at f_c'' followed by a linear descent until a strain of 0.0038.

Parabola:

$$f_c = f_c'' \left[\frac{2 \varepsilon_c}{\varepsilon_0} - \left(\frac{\varepsilon_c}{\varepsilon_0} \right)^2 \right] \quad \text{For } \varepsilon_c \leq \varepsilon_0 \quad (4-1)$$

Linear descent:

$$f_c = f_c'' - E_{cd} (\varepsilon_c - \varepsilon_0) \quad \text{For } \varepsilon_c > \varepsilon_0 \text{ and less than } 0.0038 \quad (4-2)$$

With:

$$f_c'' = 0.9 f_c' \quad (4-3)$$

$$\varepsilon_0 = \frac{1.8 f_c''}{E_c} \quad (4-4)$$

$$E_c = w_c^{1.5} 33 \sqrt{f_c'} \quad \text{For } 90 \text{ lb / ft}^3 \leq w_c \leq 160 \text{ lb / ft}^3 \quad (4-5)$$

$$E_c = 57000 \sqrt{f_c'} \quad \text{for normal weighted concrete with } f_c' \text{ in psi} \quad (4-6)$$

$$E_{cd} = \frac{0.15 f_c''}{0.0038 - \varepsilon_0} \text{ or } 500 \text{ ksi} \quad (4-7)$$

Where:

f_c is the concrete compressive stress.

f_c'' is the maximum concrete compressive stress.

f_c' is the uniaxial concrete compressive strength under standard test cylinder.

ε_c is the concrete strain.

ε_0 is the concrete strain at maximum compressive stress.

E_c is the elastic modulus, defined by ACI 318 (2011).

E_{cd} is the descending elastic modulus ACI 318 (2011).

w_c is the density of the concrete in lb/ft³.

These equations were utilized to create the compressive curve for concrete that was inputted into Abaqus's concrete damage plasticity model, discussed below. A small modification was necessary in order to meet the requirement of Abaqus. In Abaqus, for a material to fail, the final strain point must bring the stress below 5% of the maximum

stress; otherwise it assumes that the final stress-strain point continues at the same stress infinitely. For example, from Figure 4-2, the stress would remain at $0.85 f_c''$ until the model completed its run. One of the concrete curves utilized in Abaqus is the one shown in Figure 4-3, as can be seen the stress drops to 1% of the peak stress allowing for a failure of the material, but not to zero as this can cause issues in the matrix calculations resulting in abnormal model failures.

4.2.2 Hsu Tension Model

ACI 318 (2011) Section 8.6.1 recommends that the average splitting tensile strength be $f_{ct} = 6.7\sqrt{f'_c}$ for normal strength concrete, where f'_c is in psi. In Section 9.5.2.3 the modulus of rupture is defined as $f_r = 7.5\sqrt{f'_c}$ where f'_c is again in psi. Clearly, the tensile strength will be far lower than the compressive strength. Despite a loss in strength following the cracking of the concrete, the tensile strength does not drop to zero as can be seen in Figure 4-4. While a variety of material models exist, the Hsu (1993) tension model has provided accurate results in Abaqus models Koh (2011). Hsu described the tensile stress-strain curve of concrete as seen below:

Ascent:

$$f_c = E_c \varepsilon_c \quad \text{For } \varepsilon_c \leq \varepsilon_{cr} \quad (4-8)$$

$$E_c = 47000 \sqrt{f'_c} \quad (4-9)$$

Descent:

$$f_c = \frac{f_{cr}}{1 + \sqrt{\frac{\varepsilon_c - \varepsilon_{cr}}{0.002}}} \quad (4-10)$$

$$f_{cr} = 3.75 \sqrt{f'_c} \quad (4-11)$$

Where, as before, f'_c is the uniaxial concrete cylinder compressive strength in psi.

f_{cr} is the cracking stress of plain concrete in psi.

ϵ_{cr} is the cracking strain.

For similar reasons to that of the compressive strength curves, the tensile curve that were utilized for input in Abaqus needed to be modified slightly to create a failure point. In order to accomplish this, the tensile strength was brought to a final stress that was 5% of the peak tensile strength. The existing curve was extended linearly after flattening out to a strain of 0.1 to coincide with the failure of the steel reinforcement. An example of a tensile curve, which is based on a concrete with a compressive strength of 6150 psi, can be seen in Figure 4-5. Although it is not visible, the tensile strength rises suddenly and then begins decreasing in the curve shown.

4.2.3 Park and Paulay Steel Model

In their book on reinforced concrete, Park and Paulay (1975) present a steel model based on the principles of strain-hardening. The model consists of an elastic region, a yield plateau region and a strain hardening region as can be seen in Figure 4-6. The following are the equations utilized to create the characteristic curve:

Region AB:

$$f_s = E_s \epsilon_s \quad \text{For } (\epsilon_s < \epsilon_y) \quad (4-12)$$

Region BC:

$$f_s = f_y \quad \text{For } (\epsilon_y \leq \epsilon_s < \epsilon_{sh}) \quad (4-13)$$

Region CD:

$$f_s = f_y \left[\frac{m(\varepsilon_s - \varepsilon_{sh}) + 2}{60(\varepsilon_s - \varepsilon_{sh}) + 2} + \frac{(\varepsilon_s - \varepsilon_{sh})(60 - m)}{2(30 + r + 1)^2} \right] \quad \text{For } (\varepsilon_y \leq \varepsilon_s < \varepsilon_{sh}) \quad (4-14)$$

Where:

$$m = \frac{\left(\frac{f_u}{f_y}\right)(30 + r + 1)^2 - 60r - 1}{15r^2} \quad (4-15)$$

$$r = \varepsilon_{su} - \varepsilon_{sh} \quad (4-16)$$

And:

ε_{su} is the ultimate strain.

f_u is the ultimate stress.

m and r are variables of the equation.

f_y is the yield strength of the steel.

f_s is the compressive stress at a point on the curve.

E_s is the modulus of elasticity for the steel.

ε_{sh} is the strain when strain hardening begins.

ε_s is the strain at a point on the curve.

As was the case with the other material models, the final stress value was brought below 10%, in this case 1%, of the peak stress value. The reduction to 1% was chosen after model validations still showed residual strength with higher values that did not exist in the experimental results.

4.3 Abaqus Parameters

The Abaqus software provides the user with an abundance of options to choose from for modeling a variety of scenarios. For this reason, the modeling choices that the user makes must be concise in order to properly capture the behavior of the problem that needs to be solved. The following section will present some of the choices made for the model validation and experimental investigation, and why they were chosen. Additionally, specific modeling intricacies will be discussed that enabled faster modeling of the specimens and ensured accuracy despite not utilizing all of the physical attributes of the test, i.e. support conditions.

4.3.1 Concrete Damage Plasticity Model

While three material models exist that are specifically designed to model concrete in Abaqus, the work presented will utilize the concrete damage plasticity (CDP) model. Koh (2011) utilized this material model to accurately predict the results of connections under progressive collapse. The CDP material model is a plasticity-based model available in Abaqus/Standard and Abaqus/Explicit and can model concrete under monotonic, cyclic and/or dynamic loading.

The CDP model was selected because of its versatility and ability to run in Abaqus/Explicit, allowing for the modeling of highly dynamic experiments. The model uses concepts of isotropic damage elasticity in conjunction with isotropic tensile and compressive plasticity to represent the inelastic behavior of concrete. The model can also be defined for sensitivity to the strain rate, including the ability to increase peak strength at higher strain rates. The model allows for different yield strength in tension and compression as well as different degradation of the elastic stiffness in tension and compression.

Thus, the model allows for two material curves, the compression curve shown in Figure 4-7; and the tension curve, shown in Figure 4-8. The compression curve consists of a linear-elastic (undamaged) section that continues until reaching the stress σ_{co} ; this section has a slope of E_o , the elastic Young's modulus. The following section is a curve that constitutes the start of the plastic region which reaches a peak at the ultimate stress, σ_{cu} , after which the stress decreases along the same path. The curve follows a similar path to that of the modified Hognestad parabola which aids in the input of the material properties. The tension curve for the CDP model begins in a similar fashion, with a slope of E_o rising until it reaches the tensile failure stress, σ_{to} . Following this section, the stress reduces as tension stiffening rules the post-peak behavior. Tension stiffening accounts for the interaction between concrete and steel by representing the behavior of both through average strain and average stress throughout the cracked region. In order for the CDP model to function properly, the tension stiffening region must be properly defined. Abaqus recommends a linear degradation from the peak stress until reaching zero at the ultimate strain, however, the method described in section Hsu Tension Model will be utilized to better approximate the tension stiffening effect.

An important feature of the CDP model is the damage parameters for both the concrete and tension portions of the concrete model. The damage is designed to define the behavior of the material after being loaded and unloaded (cyclic loading). Loading beyond the elastic range in either compression or tension will lead to a decrease in strength and stiffness that must be accounted for. The following two damage parameters, d_c and d_t , define the damage for compression and tension respectively.

The values for these damage parameters range from zero, no damage, up to one, complete damage and loss of all strength.

The stress-strain relationship for the compression curve after reaching peak stress can be defined in terms of stress and the inelastic (crushing) strain, ε_c^{in} . The inelastic strain is calculated as follows:

$$\varepsilon_c^{in} = \varepsilon_c - \varepsilon_{oc}^{el} \quad (4-17)$$

$$\varepsilon_{oc}^{el} = \frac{\sigma_c}{E_0} \quad (4-18)$$

Where:

ε_{oc}^{el} is the elastic compressive strain.

ε_c is the total compressive strain.

σ_c is the concrete compressive stress.

E_0 is the elastic Young's modulus.

Abaqus takes the inelastic strain values and converts them to plastic strain values, ε_c^{pl} . Equation (4-19) shows how the plastic strain values are calculated, these values must always be positive.

$$\varepsilon_c^{pl} = \varepsilon_c^{in} - \left(\frac{d_c}{1-d_c} \right) \left(\frac{\sigma_c}{E_0} \right) \quad (4-19)$$

For the tension behavior, the failure is characterized by the post failure stress and cracking strain, $\varepsilon_t^{\sim ck}$. The cracking strain is defined by using the equations below:

$$\varepsilon_t^{\sim ck} = \varepsilon_t - \varepsilon_{ot}^{el} \quad (4-20)$$

$$\varepsilon_{ot}^{el} = \frac{\sigma_t}{E_0} \quad (4-21)$$

$$\sigma_t \geq \frac{\sigma_{to}}{100} \quad (4-22)$$

Where:

ε_t is the total strain.

ε_{ot}^{el} is elastic strain.

σ_{to} is the tensile failure/cracking stress.

σ_t is the concrete tensile stress, defined by in Equation (4-22) from Abaqus as the lower limit of post failure stress, this is to reduce potential numerical problems.

As in the compression curve, the cracking strain values are converted into plastic strain values, ε_t^{pl} , using the equation below.

$$\varepsilon_t^{pl} = \tilde{\varepsilon}_t^{ck} - \left(\frac{d_t}{1-d_t} \right) \left(\frac{\sigma_t}{E_o} \right) \quad (4-23)$$

In order to calculate the damage parameters for a specific concrete, cyclic loading tests must be performed on concrete samples, such as concrete cylinders. The tests performed by Feldman and Siess (1958) did not include cyclic loading tests of the batches of concrete utilized to create the experimental beams. While it is possible to utilize the peak compressive stress and some of the mix properties to find a comparable mix that has been cyclically loaded, it was deemed impractical as even minor changes in the material properties could adversely affect the damage results. Without having been present for the Feldman and Siess experiments, the specific mixing and curing practices can never be known. Therefore, a linear damage model was created for both

compression and tension. The compression damage begins at the yield point and continues to 0.004 total strain reaching a damage value of 0.6. Any value higher than this yielded a negative plastic strain. Similarly, the tension damage begins at the cracking strain with a value of 0 and ends at a value of 0.95 damage at 0.1 total strain.

In addition to the compression and tension characteristic curves and their respective damage parameters, the CDP model also contains a set of parameters to further control the properties of the material model. These parameters include: the dilation angle (φ), the flow potential eccentricity (ε), the compressive stresses ratio (f_{bo} / f_{co}), the stress invariant ratio (K) and the viscosity parameter (μ). As explained in the previous section, little is known about the concrete utilized by Feldman and Siess beyond its basic properties. Several parametric studies were performed in conjunction with the work below to study the effects of these parameters. In addition to showing little change in the results, without having experimental data to back up the changing of a parameter, the justification for making modifications was lacking. Therefore, the default values for these parameters remained unchanged during the modeling process. These default parameters provided by Abaqus can be seen in Table 4-1.

4.3.2 Elements

A variety of options exist when creating the mesh elements in Abaqus, one of the most important choices in Abaqus consists of choosing either first or second order elements. First order elements have nodes only at the corners and use linear interpolation to calculate the necessary field variables such as displacements and temperatures. Second order elements have a node in the middle, within the element, and use quadratic interpolation rather than linear. For most cases, Abaqus recommends

the use of second order isoparametric (quadrilateral and hexahedral elements capable of modeling non-rectangular shapes (Cook et al. 2002)) in conjunction with reduced integration provide the most efficient elements in problems with a smooth solution. However, for this analysis, first order element and reduced integration were utilized as they are ideal for large strain gradients and plasticity analysis with large strains.

As a result, the C3D8R, an 8 node linear brick element, was utilized with reduced integration in modeling the concrete; a drawing of the C3D8R element can be seen in Figure 4-9. This drawing shows that each face of the element has four integration points. The use of reduced integration elements can help avoid shear and volumetric locking (numerical formulations in fully integrated elements can lead to non-existent shear strain values) that can create stiffness that is not based on the physical or material properties of the model. Additionally, Cook et al. (2002) explained that the use of reduced integration can not only reduce computational time, it may also improve the results of FEA models as reduced integration elements eliminate over-stiffness caused by full integration.

While first order elements such as C3D8R do not suffer from issues of shear and volumetric locking, they do suffer from hourglass effect (or spurious modes). Hourglass effects are problems that occur in first-order, reduced-integration elements where the elements will distort in a manner that will cause the strain values at the integration points to be zero, which then leads to uncontrolled distortions in the mesh (Simulia 2011). In order to combat this issue, Abaqus has built in hourglass controls.

Also worth of mention is the type of element utilized for modeling both longitudinal and shear reinforcement. These elements were modeled as B31 2-node linear beams.

Abaqus/Explicit only allows the use of B31 elements for wire parts. All of these elements were based on wire frame parts, which will be discussed later on in the section below, Model Formulation.

4.3.2.1 Element dimensions

The mesh for the beam and reinforcement was seeded and meshed such that all elements were one inch in length, meaning that for the C3D8R the elements were one inch cubes. These element dimensions were chosen after parametric studies with these elements, and also half inch elements, were performed. The half inch elements yielded approximately the same results; however, the computational time increased substantially. Larger element dimensions were not viable as a square mesh was desired and the spacing between the reinforcement would not allow for a larger mesh without the reinforcement embedding inside of elements rather than on the nodes of the concrete elements.

4.3.2.2 Hourglass controls

Due to the aforementioned issues created by hourglass effects, Abaqus included in the element formulation the choice of implementing five hourglass controls to enhance the default behavior of the elements. While each has its own purpose, only two of the hourglass controls were deemed useful, following parametric studies of static and dynamic cases, for the work conducted here: the enhanced and stiffness hourglass controls. The enhanced hourglass control can give more accurate displacement results for coarse meshes that use linear-elastic materials when compared to other hourglass controls, and also provide higher resistance to hourglass effects for nonlinear materials. The issue with this higher resistance is that the enhanced hourglass control can create overly stiff behavior in plastic models experiencing bending; thus, care must be taken

when applying it. The stiffness hourglass control for first order, reduced integration elements changes the dependence of stiffness from the bulk modulus to the shear modulus. Additionally, a scale factor can be applied to these stiffness factors to manipulate the hourglass stiffness.

When utilizing any of the hourglass controls, precautions needed to be taken. The first, and easiest, method of checking the validity of using an hourglass control was to check the displaced shape of the beams in the output file. If any abnormalities were apparent, a different hourglass control was chosen or modifications were made to the model, as necessary. The second method of verifying the hourglass controls was to output the artificial energy and compare it to either the internal energy or external work (depending on the case that was being analyzed). If the internal energy did not exceed 10% of these values, the hourglass control was deemed to be valid. When the value of internal energy exceeds 10% it indicates that the hourglass controls are overcompensating for errors (dissipating excess energy) in a model and should therefore be modified or replaced. The internal energy was always checked following a simulation; however, visual confirmation of an error, when visible, was a more efficient method of discovering any issues.

4.3.2.3 Distortion control

While the use of any added features in the element formulation was generally avoided in order avoid creating behavior that was not present in the physical specimen, due to the nature of reduced integration, certain features were enabled to improve the numerical results. The results of these models were always checked through parametric studies as well as evaluations of the energy and other outputs of the simulations. The distortion control option in the element formulations is designed to avoid excessive

inversion or distortion of solid elements. While this can be useful in cases where the elements distort excessively, the distortion control dissipates a certain amount of energy depending on the level of distortion as well as the level of distortion control set. As was the case with the hourglass controls, the energy dissipated by the distortion control was plotted and compared to the total energy. If any anomalies were noticed the level of distortion control, or its implementation, were modified. While the distortion control was rarely used, primarily in parametric studies that will not be used as validation cases; due to some of its benefits, it deserved mention.

4.3.3 Model Formulation

The physical attributes of a test specimen do not always easily translate into the numerical form; therefore, this section will discuss the methodology use to translate certain physical features to aid in the numerical simulation. Some of these changes included modeling the reinforcement as wires, the supports as single points and applications of the load through constraints.

4.3.3.1 Wire parts and embedment

The complexity of the Finite Element models would have increased exponentially if the reinforcement had been modeled as a solid part. First, the location of each section of reinforcement would need to be removed from the concrete material in order to properly account for conservation of volume. Second, a special set of constraints would have been necessary in order to keep the reinforcement in place. Third, the number of elements in each section of reinforcement would have increased as well. Finally, the interaction between concrete and steel would need to be properly defined to ensure the correct behavior as bending occurred.

However, wire elements have been shown to work accurately in reinforced concrete FE analyses of full scale structures. Typically, the rebar is only modeled for small-scale investigations, such as penetration performance. They greatly reduces the computational costs, do not create large issues with the conservation of volume and do not require any input on the interaction of concrete and steel. Instead, the beam is meshed in such a manner that the nodes of the beam and the nodes of the reinforcement were located in the same position. The embedment constraint (Simulia 2011) was then applied to the reinforcement and the beam. The embedment constraint ties the nodes of the reinforcement to the nodes of the concrete so that they must move in unison. While in the physical specimen this would not be 100% accurate, the movement of the reinforcement during testing is so slight that this was deemed a suitable approximation.

4.3.3.2 Boundary conditions for supports

Modeling the support conditions to the physical specifications of the test proved to be impractical. In addition to the added computational time of meshing the supports, the rotational degrees of freedom provided by the supports were difficult to replicate. While a model of a mere cylinder could be utilized to model the supports, when the load is removed from the beam its natural reaction is to rebound and therefore lift off of the supports. The actual test specimen had rollers for supports with the beams being attached to the support and permitted to rotate about the roller.

Instead of using rollers, the supports were approximated using a single reference point tied to a collection of nodes, with the boundary conditions applied to the reference node, as shown in Figure 4-10. The boundary condition applied to the reference point, labeled “Left Support” in the image, constrains the displacement in the y-plane (down),

and leaves the x and z planes as well as the rotations to move as necessary. The reference point is then tied to the series of nodes highlighted in red. When one row of nodes was chosen as the support, nodal deformations occurred; therefore, three rows of nodes were chosen to stabilize the reaction at the supports. This solution had little to no effect on either the displacement or reaction results and solved the issue of excessive nodal deformations. Additionally, these results were compared to a similar model with the actual support conditions, both performed similarly (before the beam rises off of the supports in the “roller” model). These support conditions were also replicated in the predictions model as the beams will be tested with a similar roller support system.

4.3.3.3 Additional constraints

In addition to the constraints mentioned above, another constraint was utilized to apply the load to the beam. In a comparable method to the support conditions mentioned above, a reference point was placed in the center of the stub (top of the beam) and the nodes on top of the stub were chosen as the constrained nodes, as shown in Figure 4-11. The load was then applied to the reference point which divided the load evenly among all of the constrained nodes. This method provided two advantages: the load did not need to be converted to a pressure and the constraint helped stabilize the load points. The load definition provided in Feldman and Siess (1958) is in terms of force rather than pressure. Therefore, if different loading histories were to be applied to the beam they would need to be converted to pressure applied to the top of the stub. Furthermore, the constraint on the stub aids in stabilizing the stub so that it does not experience excessive element distortion. While some crushing may occur in the stub, the model can fail prematurely if the element distortion rate is

extreme, which did not occur in the physical testing. Therefore, the constraints help to limit the distortion of the stub which has no effect on the reactions and displacements of the entire model.

4.4 Beam 1-f Model Validation Results

Beam 1-f, as mentioned previously, was designed identically to the specifications of Beam 1-h and tested statically. To ensure parity between the Beam 1-h and Beam 1-f validation models, all Finite Element simulations were performed in the Abaqus/Explicit software. In order to accomplish this without incurring excessive computational efforts, the static cases were completed in shorter duration than the actual tests, ranging between 5 and 30 seconds. These times were considerably shorter than the actual static tests, which caused some fluctuation in the results. Parametric studies were performed with increasing time that show that the results of the shorter durations could be averaged to approximate the longer duration run results without losing accuracy.

The values for concrete compressive strength were taken from an average of the values provided in Table 2-13 and inserted into the modified Hognestad curve to create the material properties for Abaqus and DSAS. Additionally, as there were no values provided for the Beam 1-f steel reinforcement, the values were taken from Beam 1-h, see Table 2-12.

. The values for all of the steel reinforcement are fairly similar; therefore, this was deemed an appropriate substitution. The Abaqus model utilizes the reduced integration, 8 node linear brick (C3D8R) elements discussed previously with the enhanced hourglass control. Additionally, the loading is displacement controlled such that the load was increased from 0 to 5 seconds from 0 to 8 inches, linearly.

The results of the DSAS and Abaqus computations are shown in Figure 4-12. The numerical simulations closely emulate the physical response observed during the experiment. The plastic region of the results deviates slightly from the experimental results, likely due to deficiencies in the plastic region of the reinforcement material models. Additionally, Figure 4-13 shows that the beam failed in compression with strain concentrations forming to the right and left of the stub in the compression zone. The experimental beam failed in a similar manner with the compression steel buckling as failure was reached.

4.5 Beam 1-h Model Validation Results

The numerical simulations of beam 1-h were complex and required extensive parametric study; which included changes in hourglass controls, material properties, dynamic increase factors and element properties. The results that will be shown below are the final models chosen based on comparisons with the experimental results and observations, as well as their parity with the methodology utilized for beam1-f. The loading function utilized for modeling was taken from an approximation of the digitized load curve, shown in Figure 4-14. The digitized load curve contains fluctuations that created unpredictable results in the numerical simulations; the approximated load function reaches the same peak load while also maintaining the same calculated impulse to ensure parity between the model and experimental results.

After performing some of the first numerical simulations with DSAS and then ABAQUS, it became evident that strain rate effects were a factor in the results of the Feldman and Seiss impact tests. The dynamic increase factors feature in DSAS was utilized to generate DIF values based on varying strain rates for the concrete in both compression and tension, as well as for the reinforcement. The results of a parametric

study utilizing DSAS to apply a variety of strain rates is shown in Figure 4-15. The model fails without including any dynamic increase factors; the use of a strain rate of 10 yielded the closest results to the experiment. Additionally, the auto strain rate value is included in the plot; it utilizes a calculated strain rate from the time history of a first run without DIF and then re-runs the model with the DIF corresponding to the calculated strain rate. The DIF values from all of these runs are detailed in Table 4-2, also listed are strain rate values utilized specifically for the Abaqus computations.

The results of the parametric study for varying strain rates in Abaqus for beam 1-h is shown in Figure 4-16. The results differed from those of DSAS; beam 1-h in Abaqus matched the experimental results at a strain rate of 0.1, rather than 10. As mentioned previously, the values of the DIF for each strain rate are detailed in Table 4-2. A comparison of the best cases of Abaqus and DSAS, mentioned above, versus the experimental results are shown in Figure 4-17. Finally, a plot of the deformed shape of beam 1-h with DIF for a strain rate of 0.1, with plastic strains visualized, can be seen in Figure 4-18.

Table 4-1. Abaqus default concrete damage plasticity parameters (Simulia. (2011).
 “Abaqus FEA.” Prentice-Hall, Vélizy-Villacoublay, France.)

Dilation Angle	Eccentricity	f_{b0}/f_{c0}	K	Viscosity Parameter
28	0.1	1.16	0.666	0

Table 4-2. Dynamic increase factors for Dynamic Structural Analysis Suite (DSAS) runs based on strain rate

Strain Rate	Dynamic Increase Factors		
	Concrete Compression	Concrete Tension	Rebar Reinforcement
0 (none)	0	0	0
0.1	1.213	1.991	1.150
1	1.281	2.586	1.200
3.306 (Auto)	1.318	3.013	1.226
5	1.331	3.186	1.235
10	1.353	3.508	1.250
20	1.375	3.879	1.265

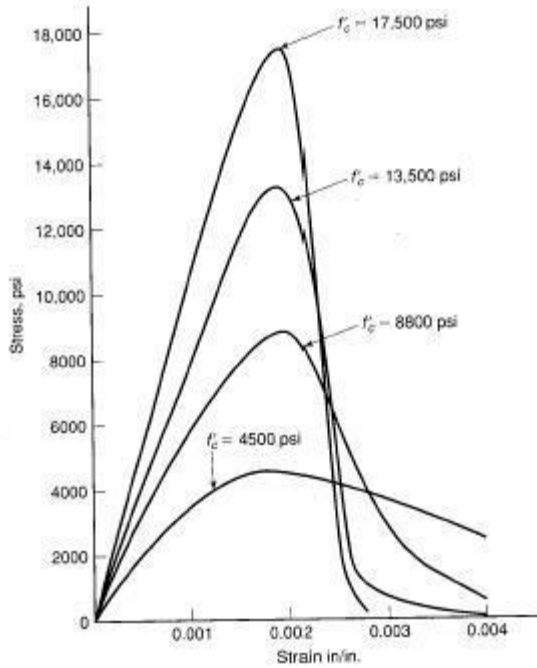


Figure 4-1. Concrete compressive stress-strain curves for different compressive strengths (MacGregor, J. G., and Wight, J. K. (2005). *Reinforced Concrete: Mechanics and Design*. Prentice-Hall.)

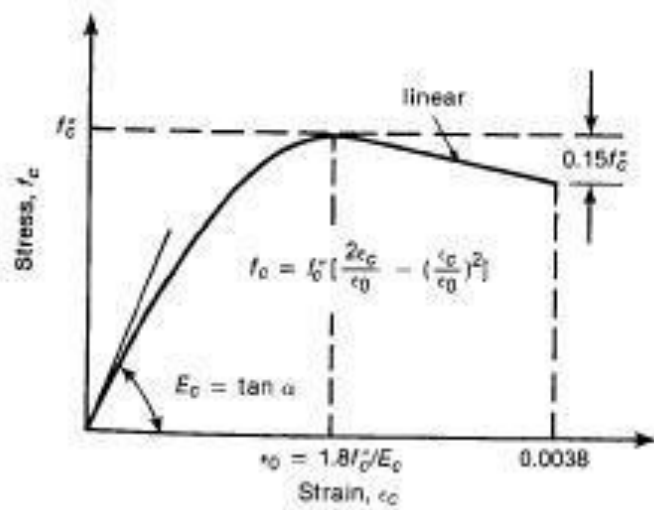


Figure 4-2. Modified Hognestad stress-strain curve for concrete in compression (MacGregor, J. G., and Wight, J. K. (2005). *Reinforced Concrete: Mechanics and Design*. Prentice-Hall.)

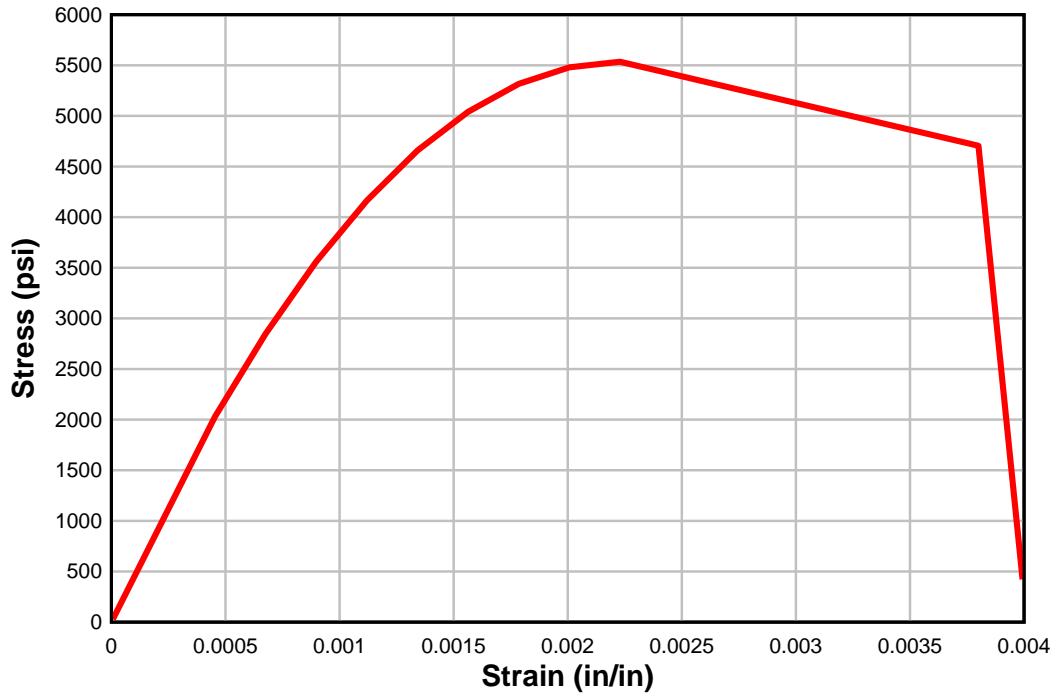


Figure 4-3. Modified Hognestad curve for Abaqus, $f'_c = 6150$ psi

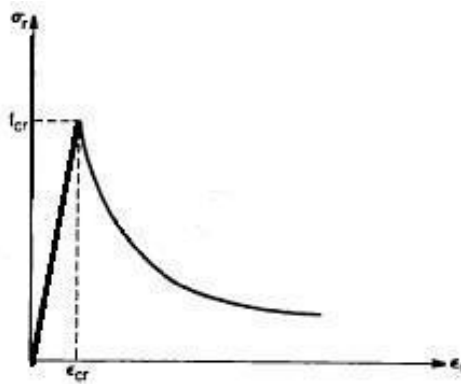


Figure 4-4. Tensile strength curve of reinforced concrete (Hsu, T. T. (1993). *Unified Theory of Reinforced Concrete*. CRC Press.)

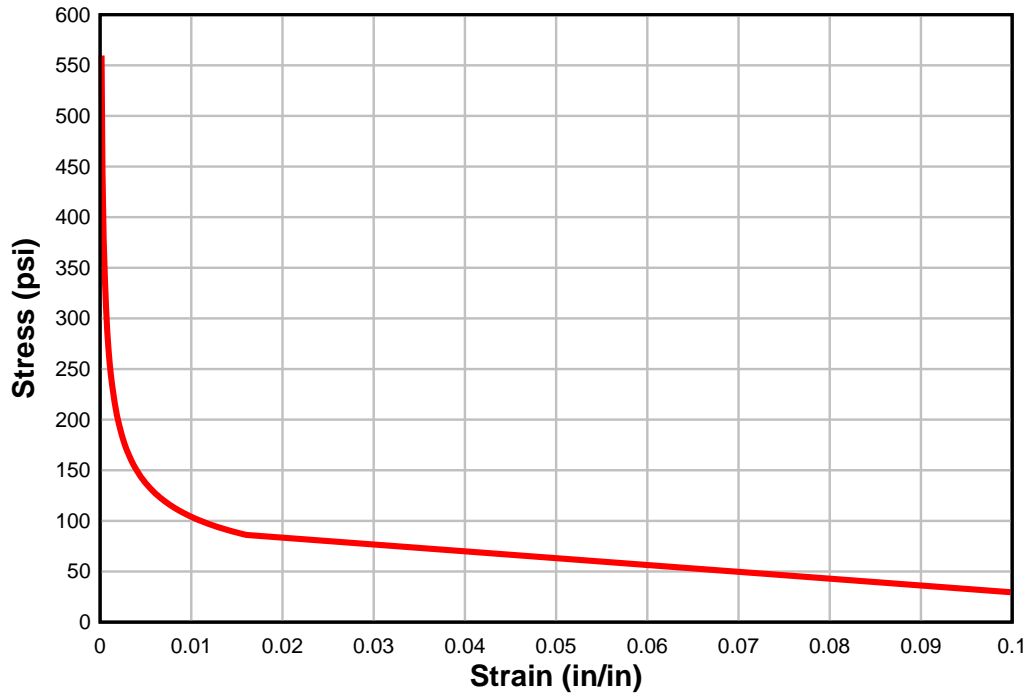


Figure 4-5. Modified Hsu tensile curve for Abaqus

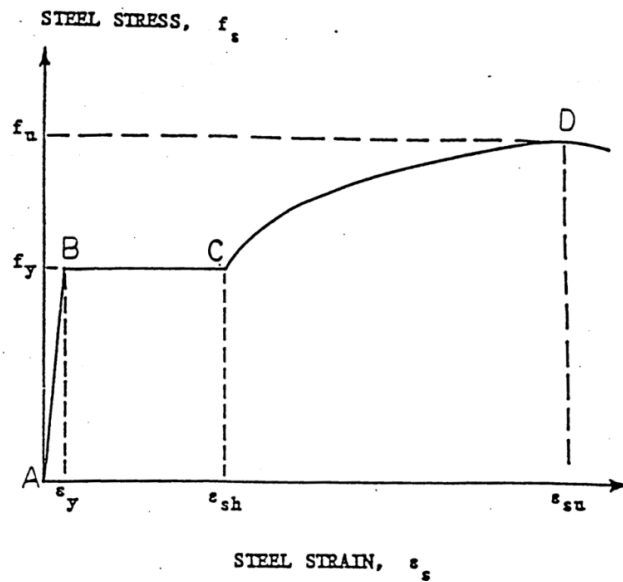


Figure 4-6. Strain hardening material model for steel reinforcement (Krauthammer, Theodor, and Shahriar, S. (1988). *A Computational Method for Evaluating Modular Prefabricated Structural Element for Rapid Construction of Facilities, Barriers, and Revetments to Resist Modern Conventional Weapons Effects*. Minneapolis, MN.)

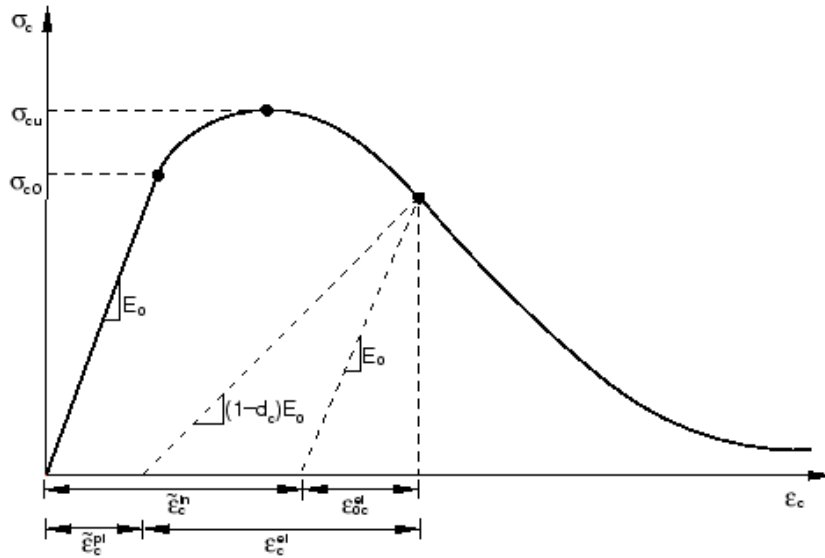


Figure 4-7. Uniaxial stress-strain curve for compression in concrete damage plasticity model (Simulia. (2011). "Abaqus FEA." Prentice-Hall, Vélizy-Villacoublay, France.)

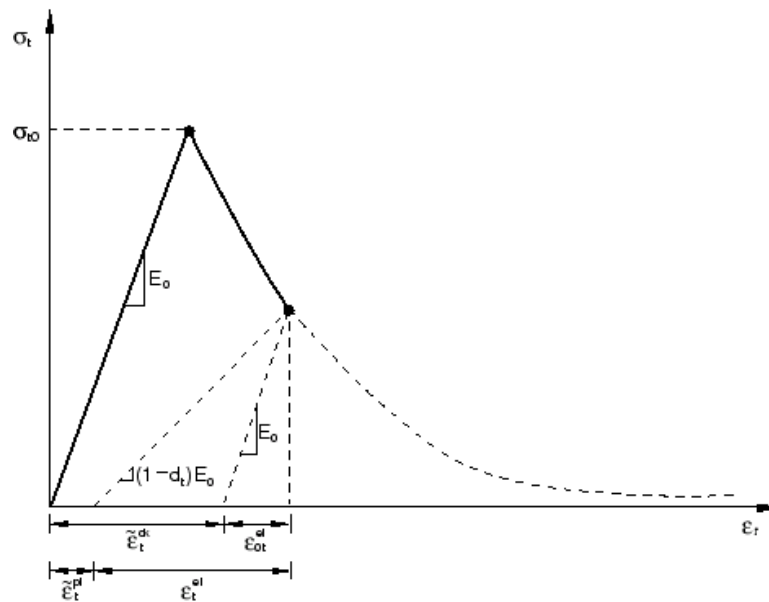


Figure 4-8. Tension stress-strain curve in concrete damage plasticity model (Simulia. (2011). "Abaqus FEA." Prentice-Hall, Vélizy-Villacoublay, France.)

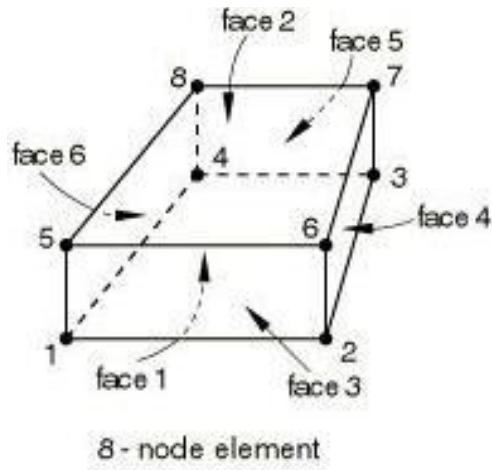


Figure 4-9. First order linear 8 node brick element (Simulia. (2011). "Abaqus FEA." Prentice-Hall, Vélizy-Villacoublay, France.)

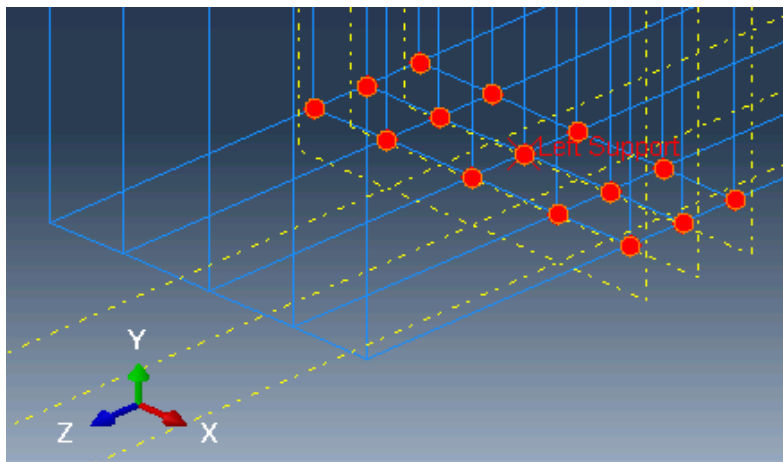


Figure 4-10. Example of support conditions for Feldman and Sesis beam 1-h

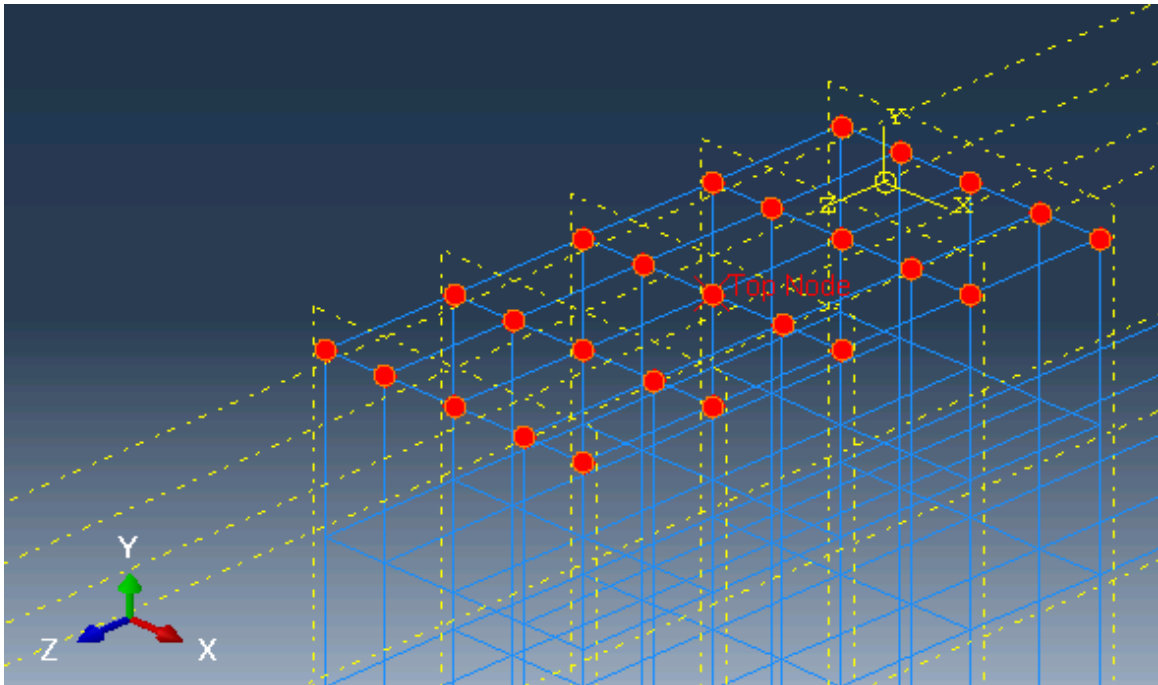


Figure 4-11. Top node constraint for applying load to Feldman and Siess beams

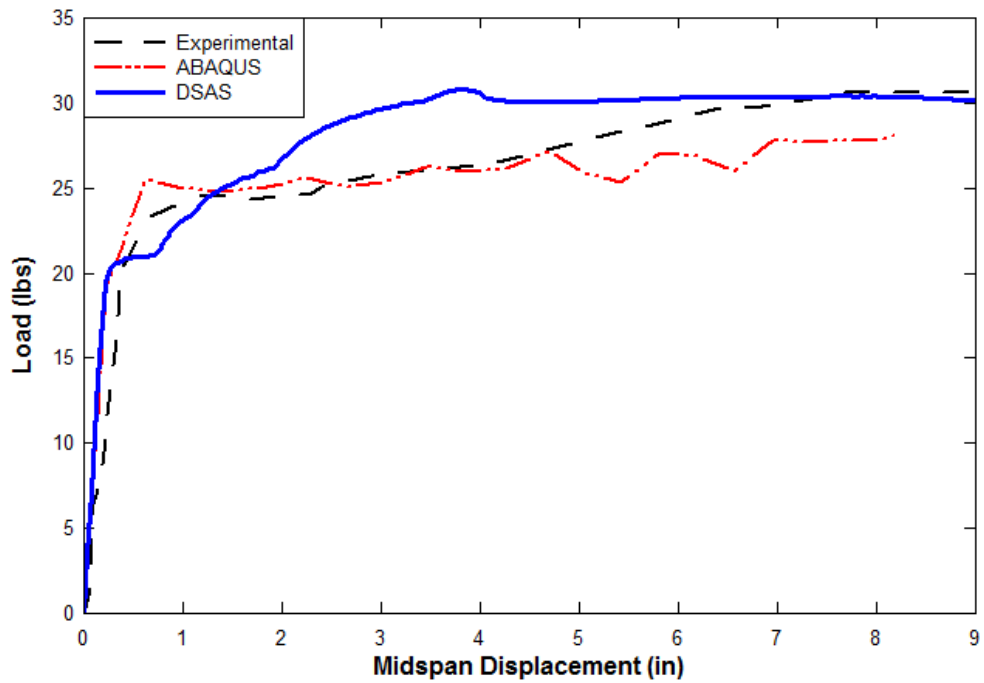


Figure 4-12. Beam 1-f Numerical vs. Experimental Results

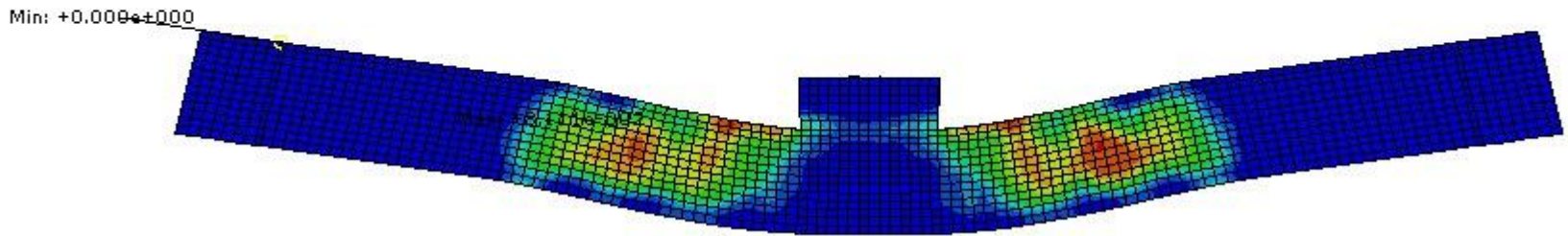
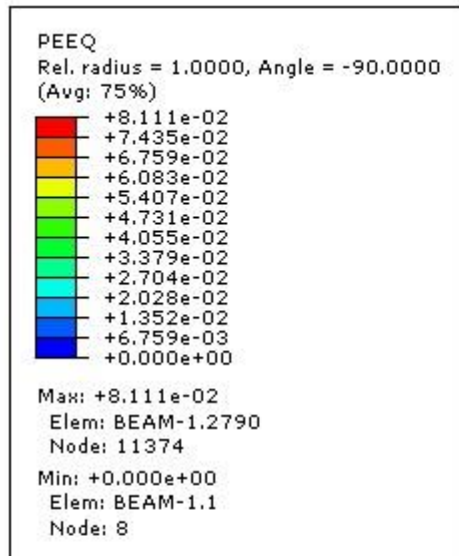


Figure 4-13. Plot of the plastic strains in deformed Beam 1f

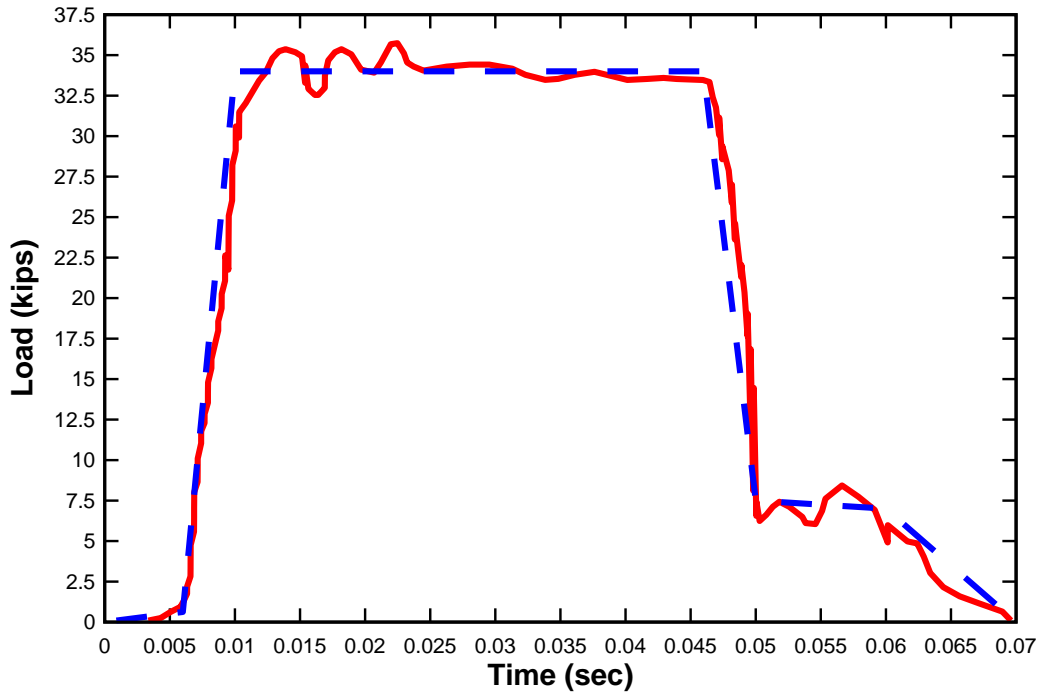


Figure 4-14. Digitized vs. approximated load curves for beam 1-h

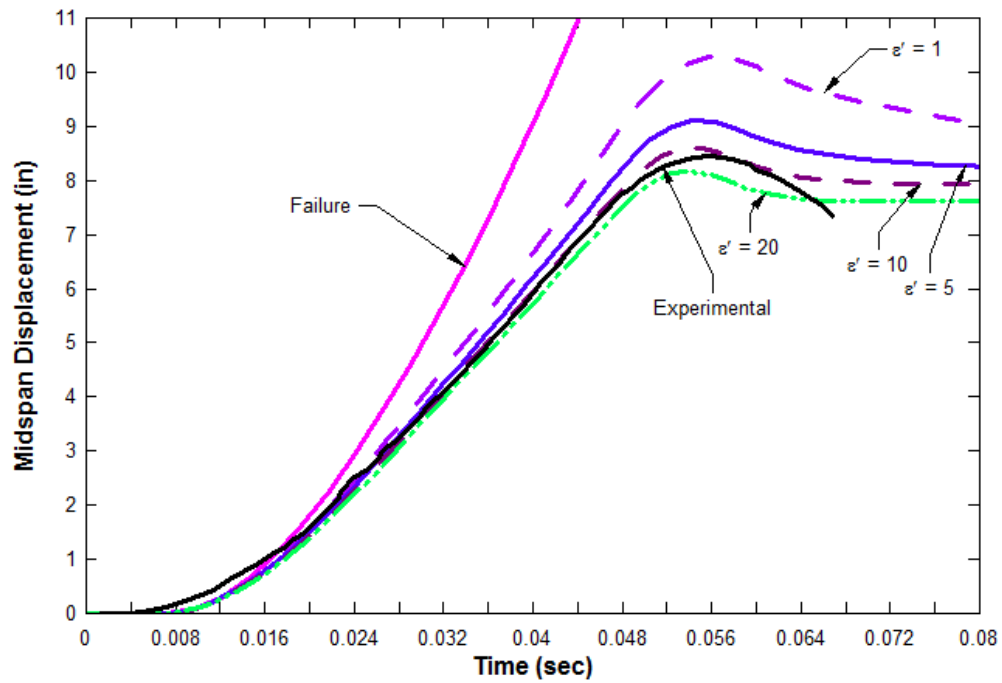


Figure 4-15. Beam 1-h DSAS parametric analysis with DIF

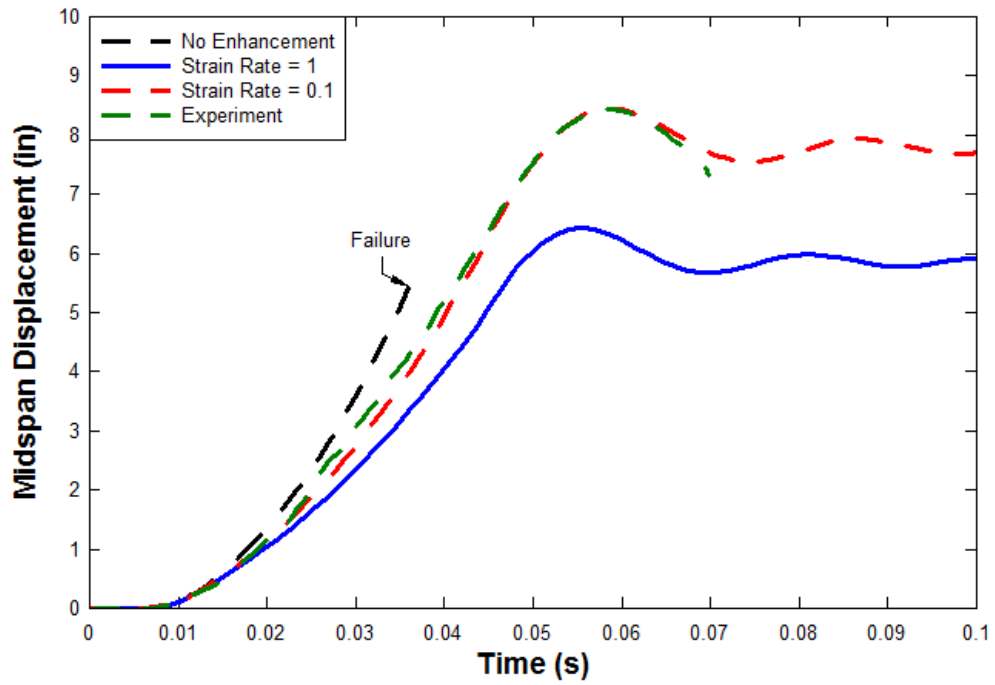


Figure 4-16. Parametric study of varying strain rates for beam 1-h in Abaqus

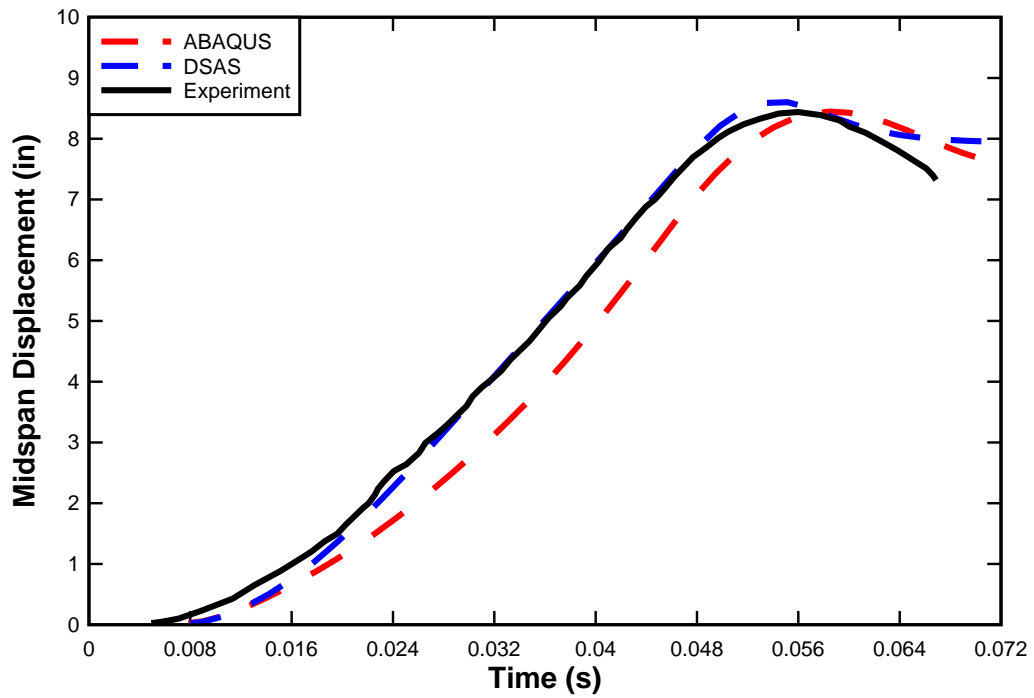


Figure 4-17. Numerical vs. experimental results for beam 1-h

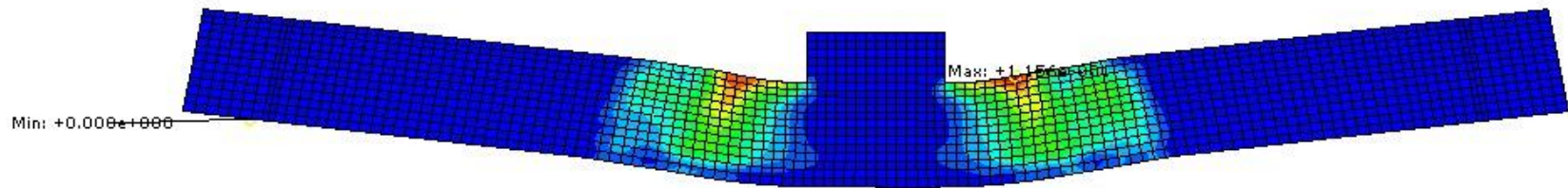
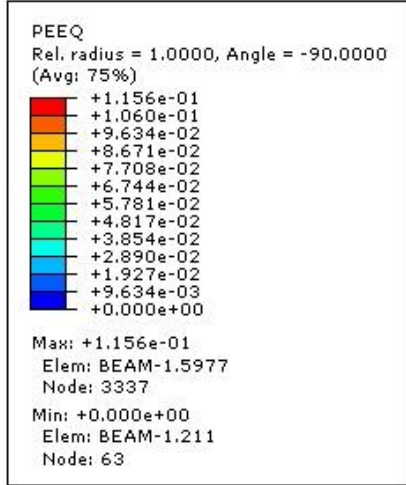


Figure 4-18. Beam 1-h Abaqus deformed plot with plastic strain

CHAPTER 5 NUMERICAL PREDICTIONS AND PRELIMINARY TEST RESULTS

5.1 Introduction

The following are the numerical predictions for the CIPPS beams subjected to static and dynamic loading, as well as preliminary tests results from the static testing of all six beam series. The numerical predictions are based on the available data for material properties provided by ERDC for NSC and Cor-Tuf. Parametric studies were performed for the dynamic cases with varying drop heights and masses. The predictions that will be shown are final cases that were chosen based on the criteria of failing and/or nearing the limits of the impact hammer the beams.

5.2 Cor-Tuf Material Model

The material properties for Cor-Tuf provided by ERDC lack the plastic behavior of the material. In order to create prediction models, approximations were made based on the material curves of Ductal which has similar linear-elastic properties to Cor-Tuf (Gowripalan and Gilbert 2000). The actual properties utilized in the model are shown in Figure 5-1. The difference between Cor-Tuf 1 and Cor-Tuf 2 occurs in the tensile region. The tensile strength of Cor-Tuf 2 decreases rapidly after reaching 2400 psi, whereas Cor-Tuf 1 experiences a form of tension stiffening as the fibers bridge the cracks at 2400 psi enabling it to reach a peak of 3600 psi.

5.3 Static Test Predictions and Test Results

5.3.1 B1F

B1F was a normal strength concrete beam with full reinforcement that was tested statically. A pre-test photo of the beam can be seen in Figure 5-2. A photo of the beam during loading can be seen in Figure 5-3, the beam is beginning to show typical

cracking patterns seen in flexural static tests. B1F failed due to buckling of the compression rebar which can be seen in Figure 5-4. The beam reached a peak load of approximately 37 kips and failed at about 5.5 inches. After the failure of the compression rebar the beam continued to carry a significant amount of load (above 30 kips).

Both ABAQUS and DSAS provided reasonable predictions of the performance of the beam, as shown in Figure 5-5. The ABAQUS results did not seem to acquire the same plastic load as the experiment. These differences will be discussed further in the conclusions. DSAS predicted the beam would carry load to a greater deflection than occurred in the actual experiment.

5.3.2 B2A

The B2A series was created as a comparison series for the B6F series. The B2A series was cast out of normal strength concrete while the B6F series was cast out of Cor-Tuf1 (Cor-Tuf with fibers). Neither of these beam series contain shear reinforcement with the purpose of evaluating the shear capabilities of Cor-Tuf1 and B2A being the control series for the B6F beams. This will be discussed further in the B6F static testing section later on.

The B2A series, as was expected, failed due to the formation of a shear crack on the south side of the beam, as can be seen in Figure 5-8. During testing, the beam behaved similarly to a normally reinforced beam, such as B1F, sustaining similar flexural cracks. At approximately 0.4 inches and with a peak load of 17 kips the beam failed suddenly in shear. Both ABAQUS and DSAS over predicted the peak load before failure of the beam, shown in Figure 5-9. Abaqus over predicted the displacement of the

beam as well; however, the scale of these deflections are so small that such a difference is negligible.

5.3.3 B3F

B3F is a Cor-Tuf1 beam series with full shear and longitudinal reinforcement as specified in Table 3-5. The B3F series outperformed the B1F NSC series with a peak load of 48 kips and a maximum displacement of 4 inches. While these results are impressive, they were not as high as those predicted by DSAS and ABAQUS. The failure was due to the yielding of the tension rebar at the bottom of the beam. While a certain amount of compression cracks had occurred, the beam was far from failing in compression. The fibers aided to a certain extent to reduce cracking; however, as the crack width neared the length of the fibers, pullout was inevitable. Fibers spanning the crack and pullout of the fibers are apparent in Figure 5-12. The fibers due provide a necessary ductility which became apparent after testing the Cor-Tuf 2 beam (B4F) without any fibers, discussed below.

The DSAS and ABAQUS predictions for the B3F series under static loading show a steady rise up to 65 kips and then a decrease to 40 kips for several inches, shown below in Figure 5-14. The behavior of the experimental beam was more similar to that of NSC where the material yields, becomes plastic and keeps deflecting at roughly the same load. DSAS predicts that the beam will carry load much longer than the experimental beam could whereas the Abaqus model failed earlier than the experimental.

5.3.4 B4F

The B4F beams are fully reinforced with longitudinal and shear reinforcement in the same manner as B1F and B3F, see Table 3-5. However, B4F is cast from Cor-Tuf 2

which is the same UHPC material as Cor-Tuf 1 without any fibers reinforcement. The beam was predicted to perform better than the normal strength concrete beam (B1F) but not to outperform the Cor-Tuf1 beam (B3F). The beam suffered a compression rebar failure after reaching a peak load of 43.5 kips although it continued to carry load afterward and reached a final deflection of over 8 inches. There were several interesting observations taken from this experiment. The first observation is that Cor-Tuf 2 is highly brittle when compared to Cor-Tuf1 or even normal strength concrete, no doubt due to the lack of fibers for ductility. The beam showed obvious cracks because of this before any load was even applied to the beam. In addition, this resulted in a few pieces of the beam spalling off during testing; one quarter sized piece shot over 30 feet from the beam. The second observation was that despite the fact that the compression rebar had buckled, the beam continued to carry near its peak load for another 6 inches of deflection where the beam finally began to yield. The compression near the stub was so great that when the beam was removed later from the supports, the stub simply fell off.

The predictions for B4F were fairly accurate to the experimental results, as can be seen in Figure 5-19. The DSAS continues to carry load after the failure of the experimental beam while the Abaqus prediction failed slightly prematurely.

5.3.5 B5F

B5F was a beam composed of Cor-Tuf 1 (with fibers) with no longitudinal or shear reinforcing rebar. It was tested statically to investigate the capacity of large scale UHPC members with no structural reinforcement. A pretest photo of the beam can be seen in Figure 5-20. The two slings were placed around to beam so that in the event of complete failure of the beam it would not collapse suddenly onto the ground and cause unintended damage. A photo of the beam loaded to 20 kips before total failure can be

seen in Figure 5-21. At this load the beam was observed to continue deflection, with cracking and popping noises indicating loss of strength due to fiber pullout. The observed failure mode was tensile failure approximately 4" offset from the edge of the loading stub. Evidence of this failure can be observed in Figure 5-22 and Figure 5-23. Additionally, although the beam lost all load capacity, it did not snap completely apart due to continuity requirements for hinge formation. The beam had a peak load of 22.8 kips and a peak deflection of 0.56 inches. Gross yielding of the beam occurred at a deflection of 0.31", and the beam continued to deflect until failure of the section. The residual load capacity of the beam was 2.2 kips.

Figure 5-24 compares the resistance curves of B5F between the experimental data and the ABAQUS and DSAS predictions. Both computer codes over-estimate the capacity of the structure by a significant amount, nearly double. ABAQUS predicted a peak load of 35.96 kips, while the peak load predicted by DSAS was 39.3 kips.

5.3.6 B6F

B6F was a test of Cor-Tuf 1 without any stirrups for shear reinforcement. This test was conducted due to a previous report by the Federal Highway Administration (FHWA) that tested Ductal UHPC beams without shear reinforcement (FHWA 2006). A pretest photo of B6F is shown in Figure 5-25. During testing, the beam was loaded slowly, and the primary damage mode observed was of flexural cracking. An example of these cracks can be seen in Figure 5-26 which shows the beam at a load of 45 kips. Upon further loading, the flexural cracks were observed to open while a diagonal shear crack began to form approximately 8" from the edge of the loading stub. Figure 5-27 demonstrates these cracks at a load of 47 kip. The peak load observed was at 49.5 kips with a resultant deflection of 1.5 inches. The observed failure mode was a combination

of flexural and diagonal shear. The beam yielded after 47 kips, and deflected continuously until rupture of the tensile rebar, which resulted in complete collapse of the beam. The deflection of the beam immediately prior to collapse was 4.6 inches. A photo of the beam after complete collapse is shown in Figure 5-28.

A comparison of the resistance curves generated by the numerical simulations and the experimental results is shown in Figure 5-29. The difference in the results is similar to B5F, in that both ABAQUS and DSAS predict higher strengths than what was observed. ABAQUS predicted a peak load of 64.8 kips at 0.4 inches while DSAS predicted a peak load of 65.7 kips at 0.44 inches. DSAS was unable to predict total failure of the beam, and predicted that the beam would have a continuous residual capacity of approximately 37 kips. The ABAQUS simulation, however, was able to predict the total failure of the beam, however at a much earlier displacement than what was observed (3.5 inches compared to 4.6 inches in the experiment).

5.4 Dynamic Beam Predictions

5.4.1 Cylinder and Contact Properties

The dynamic beam predictions are based on numerical simulations carried out in Abaqus/Explicit by modeling the physical attributes of the proposed experiments. The impact hammer, shown in Figure 3-6, is modeled as a simple cylinder in Abaqus, seen in Figure 5-30. The cylinder is assigned a mass equal to the desired weight of the rail cart for testing as well as an initial velocity calculated from the proposed drop height. The initial velocity is applied to the cylinder through the “predefined fields” option in Abaqus (Simulia 2011). Additionally, the degrees of freedom of the cylinder are constrained such that it can only move in the y-direction so that it cannot deflect off of the beam. The top of the beam (stub) as well as the entire hammer are given “hard”

contact properties (Simulia 2011) to approximate the contact behavior that will be experienced in the physical experiments. Furthermore, the nodes on the top of the beam remain constrained, as mentioned in the section about additional constraints, in order to mimic the behavior of the stub with a plate attached to it.

5.4.2 Gravity

An issue with modeling a cylinder impact in Abaqus/Explicit is the application of gravity. In order to create the proper magnitude in the response as well as proper behavior of the falling cylinder, gravity must be applied. However, applying gravity instantaneously can cause numerical errors. In the end, this method was chosen after several test cases were performed by applying gravity only to a beam without any loading and watching the fluctuations in deflection. These fluctuations were minor enough that applying gravity instantaneously for cases with such dynamic loading was considered acceptable.

5.4.3 Hammer Mass and Height

The heights and masses of the hammer (cylinder in Abaqus) for prediction cases were chosen after an exhaustive series of parametric studies. The original matrix of runs included heights of 5, 7.5 and 10 ft with masses of 300, 450 and 600 lbs. It was determined that for all of the beams, with the exception of B5, only the extreme load case of 10 ft and 600 lbs would be effective at creating a failure. Additional cases were created to model the maximum height of 15 ft with a mass of 600 lbs. Furthermore, a fictional cases of 15 ft and 800 lbs was created based on the notion of modification of the hammer to carry additional load beyond its original capacity. These final three cases will be reported on for all of beams.

5.4.4 Predictions

The predictions provided by Abaqus and DSAS can be seen in Figure 5-31 through Figure 5-36. The ABAQUS results show that both mixes of Cor-Tuf should outperform normal strength concrete. Additionally, the increased tensile capacity of Cor-Tuf1 should help it surpass Cor-Tuf2 in impact scenarios. The NSC beam without shear reinforcement should fail early when compared to the same beam with full reinforcement. Interestingly, and similar to the static results and predictions, the Cor-Tuf1 beam, B6, without shear reinforcement should perform similarly to B3, with shear reinforcement. B5, Cor-Tuf1 without any reinforcement, is expected to fail catastrophically, and will likely require a reduced load in order to get a proper load vs. displacement curve. However, the static tests showed that the Cor-Tuf material curves will need calibration, and therefore these predictions will change.

The DSAS results do not match up very well with the Abaqus results. In order to create the DSAS results, the load vs. time histories shown in Figure 5-37, taken from the contact forces of the cylinder on the top of the beam, from each Abaqus run impact are inputted into DSAS. These are a sample of the impact loads from a height of 10 ft with a mass of 600 lbs on each beam; the figure clearly shows that the behavior of each beam affects the load experienced in both magnitude and duration. The results under predict the expected displacement of the beams subjected to such severe loading.

Table 5-1. Summary of Test Results and Numerical Predictions for static beams

Series	Model	Load (kips)	% Difference	Deflection (in)	% Difference	Final Deflection (in)	%Difference
B1F	Experimental	38.3	-	5.909	-	5.614	-
	ABAQUS	34.4	10.1%	5.398	8.6%	6.500	15.8%
	DSAS	37.2	2.8%	3.252	45.0%	6.500	15.8%
B2A	Experimental	17.0	-	0.406	-	0.219	-
	ABAQUS	24.5	44.3%	0.481	18.3%	0.550	151.4%
	DSAS	19.7	15.7%	0.288	29.2%	0.364	66.3%
B3F	Experimental	47.6	-	1.339	-	4.097	-
	ABAQUS	65.3	37.2%	0.406	69.7%	2.500	39.0%
	DSAS	65.7	38.1%	0.445	66.8%	8.118	98.1%
B4F	Experimental	43.5	-	7.060	-	8.300	-
	ABAQUS	42.8	1.5%	5.815	17.6%	7.600	8.4%
	DSAS	48.2	10.9%	4.220	40.2%	9.000	8.4%
B5F	Experimental	22.8	-	0.313	-	0.560	-
	ABAQUS	36.0	57.7%	0.279	10.6%	0.439	21.6%
	DSAS	39.3	72.4%	0.337	7.9%	0.792	41.5%
B6F	Experimental	52.0	-	1.500	-	4.625	-
	ABAQUS	64.8	24.5%	0.405	73.0%	4.999	8.1%
	DSAS	65.7	26.4%	0.445	70.3%	4.970	7.5%

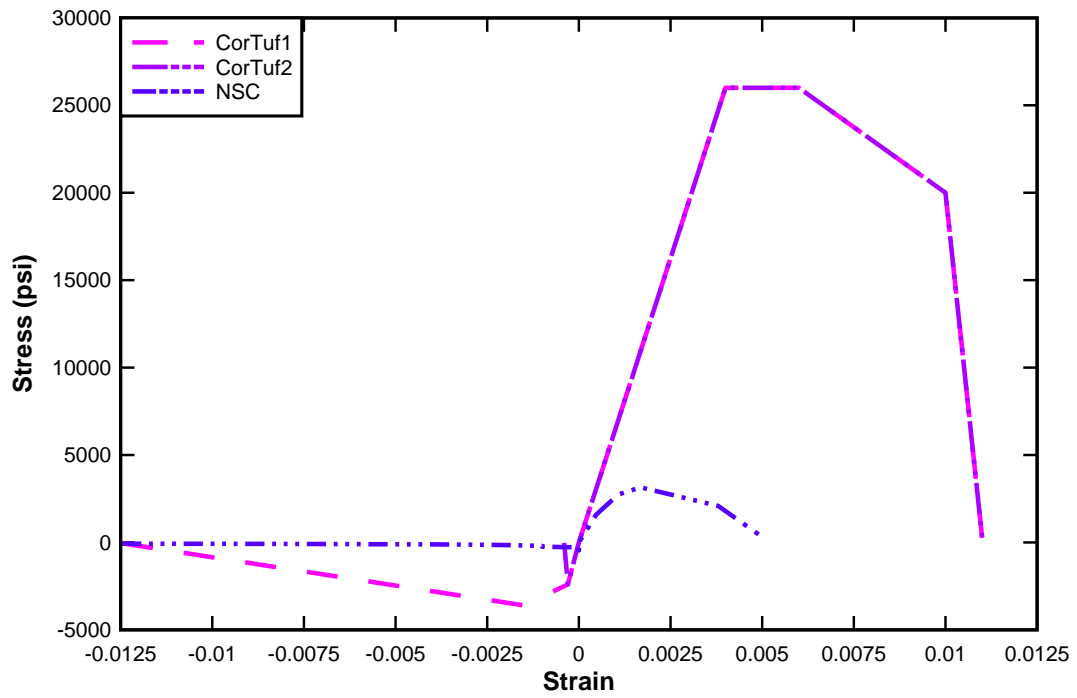


Figure 5-1. Material properties for Abaqus runs



Figure 5-2. Pre-test picture of B1F resting on the supports

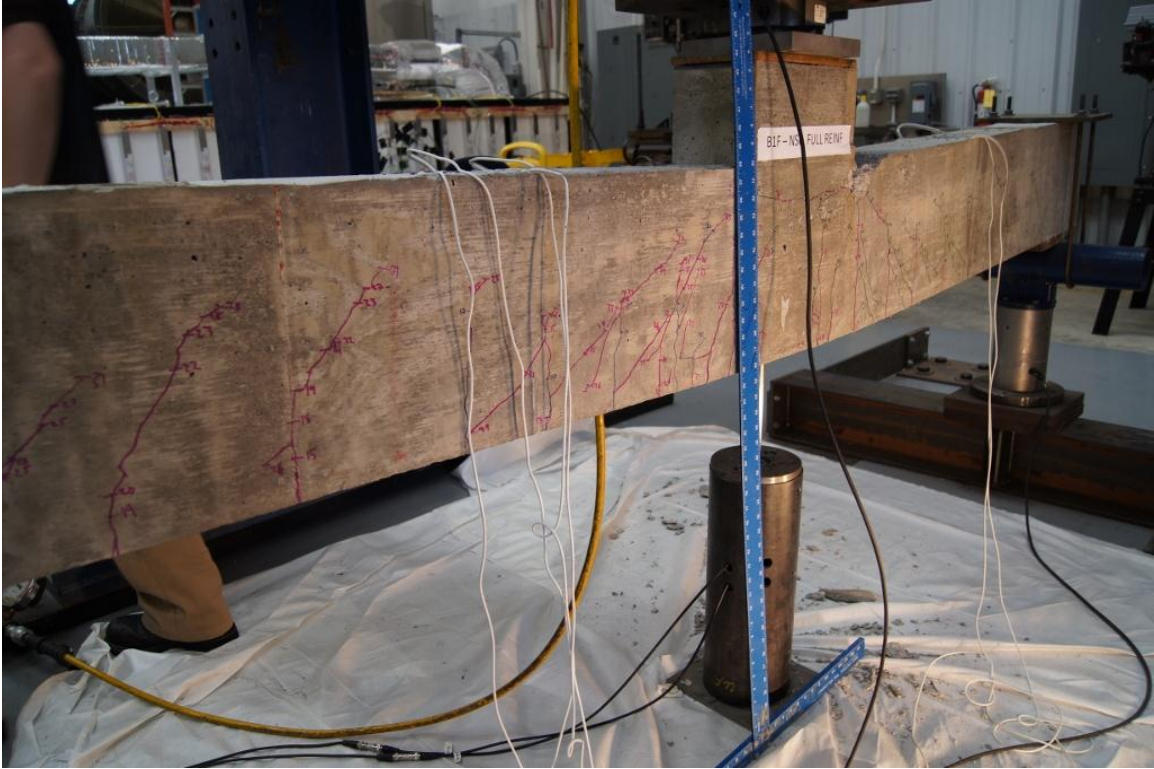


Figure 5-3. Mid-test picture of B1F loaded to 27 kips

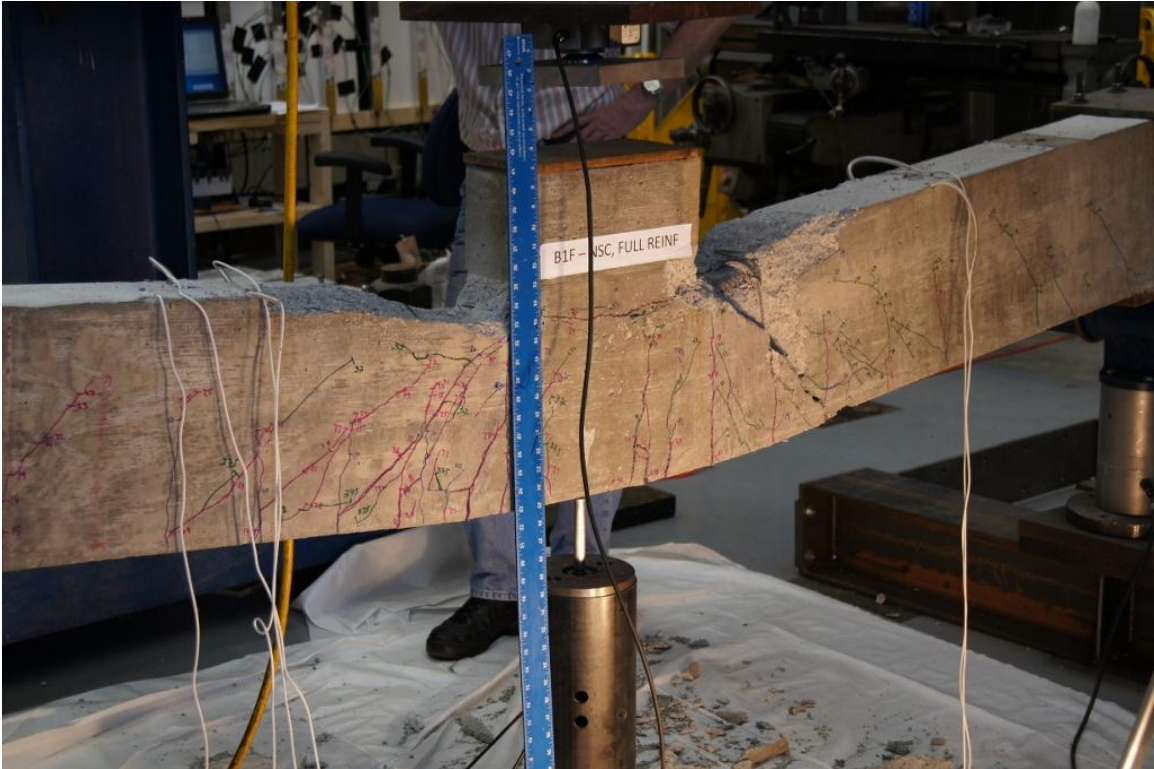


Figure 5-4. B1F at failure, a typical compression rebar failure

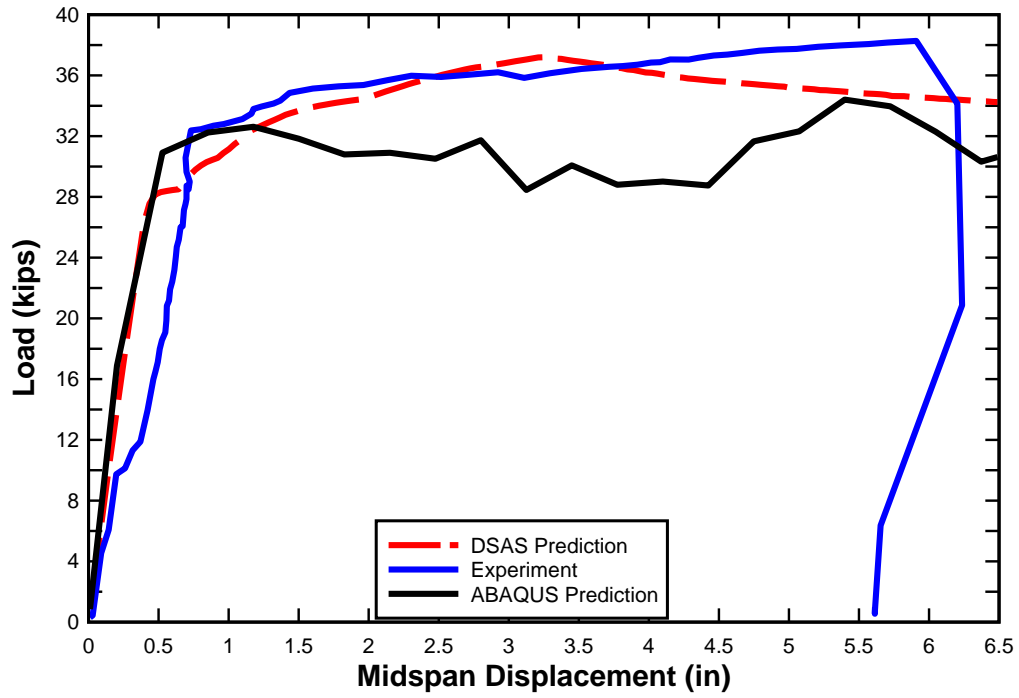


Figure 5-5. Predicted vs. Experimental Results for B1F NSC Static Test



Figure 5-6. B2A pre-test



Figure 5-7. B2A with 10 kips of load

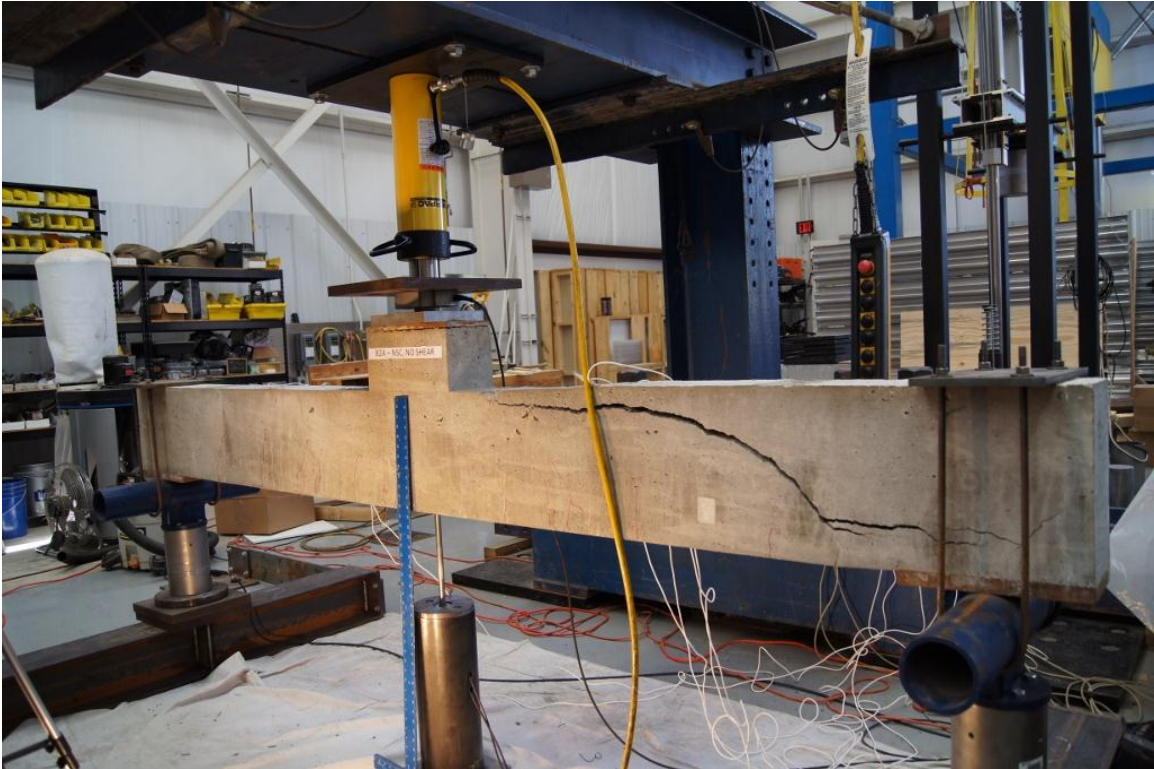


Figure 5-8. B2A at failure, due to shear

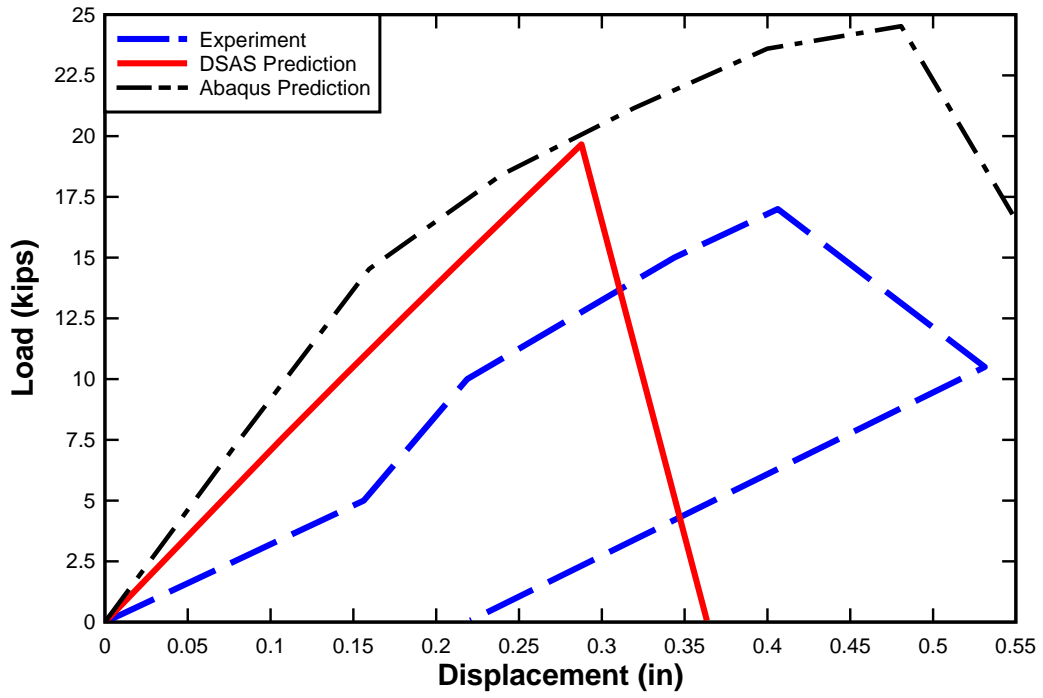


Figure 5-9. B2A Predictions vs. Experimental Results



Figure 5-10. B3F pre-test



Figure 5-11. B3F loaded to 35 kips



Figure 5-12. B3F crack at 40 kips



Figure 5-13. B3F at failure, tension rebar failure

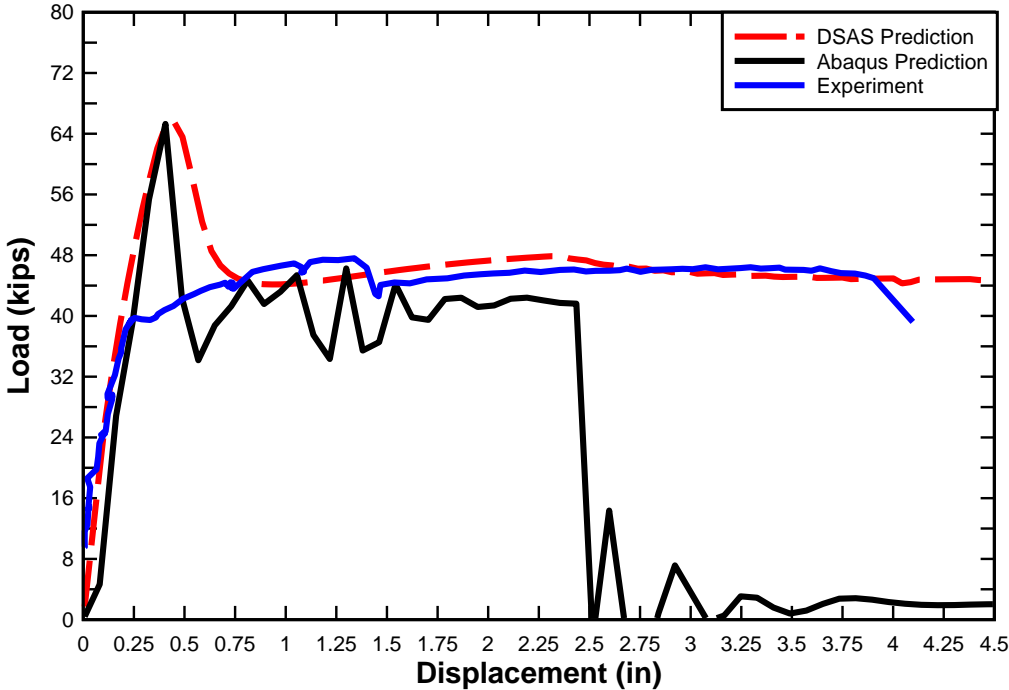


Figure 5-14. B3F Predictions vs. Experimental Results



Figure 5-15. B4F pre-test



Figure 5-16. B4F at 37 kips



Figure 5-17. B4F loaded to 40 kips



Figure 5-18. B4F loaded to failure, buckling of compression rebar

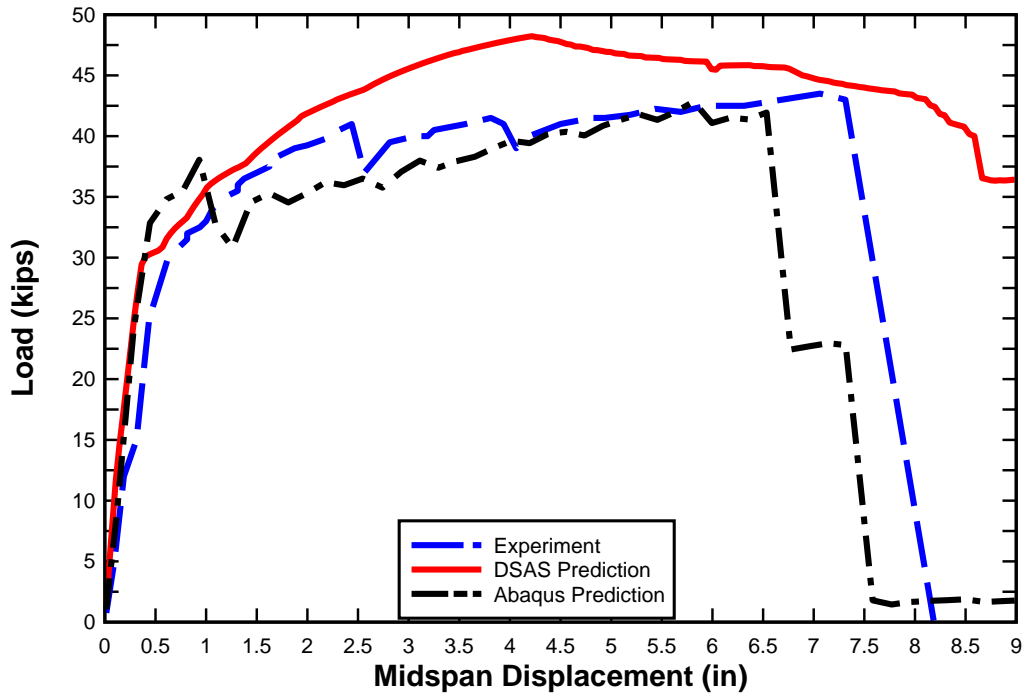


Figure 5-19. B4F Predictions vs. Experimental Results



Figure 5-20. B5F Pre-Test



Figure 5-21. B5F loaded to 20 kips



Figure 5-22. B5F tension failure



Figure 5-23. B5F tension crack at failure

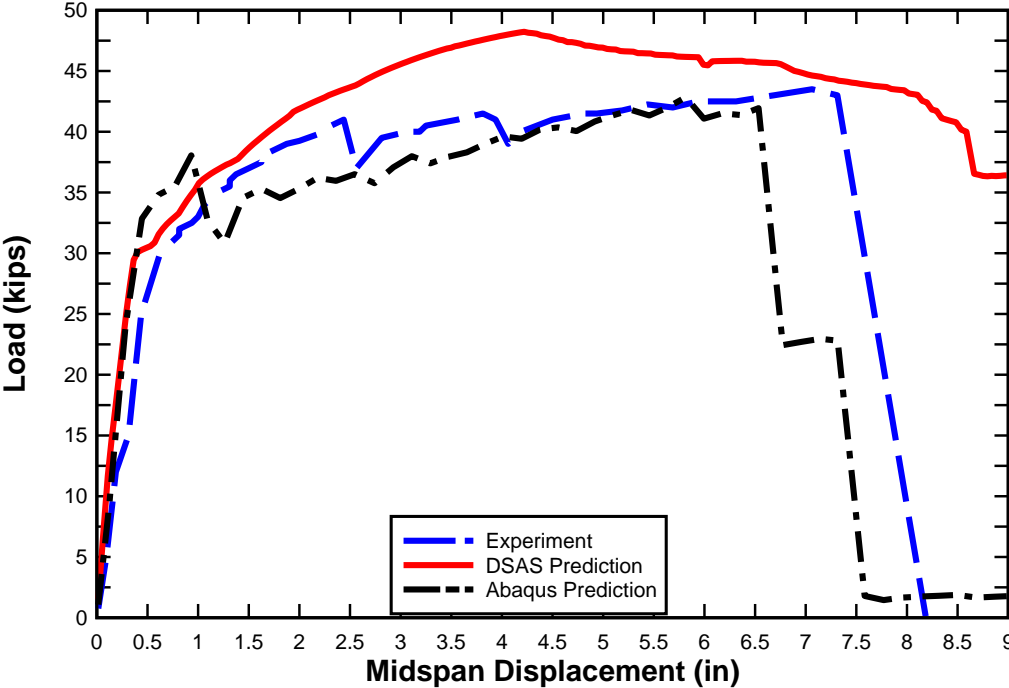


Figure 5-24. B5F Predictions vs. Experimental Results



Figure 5-25. B6F Pre-Test



Figure 5-26. B6F loaded to 45 kips

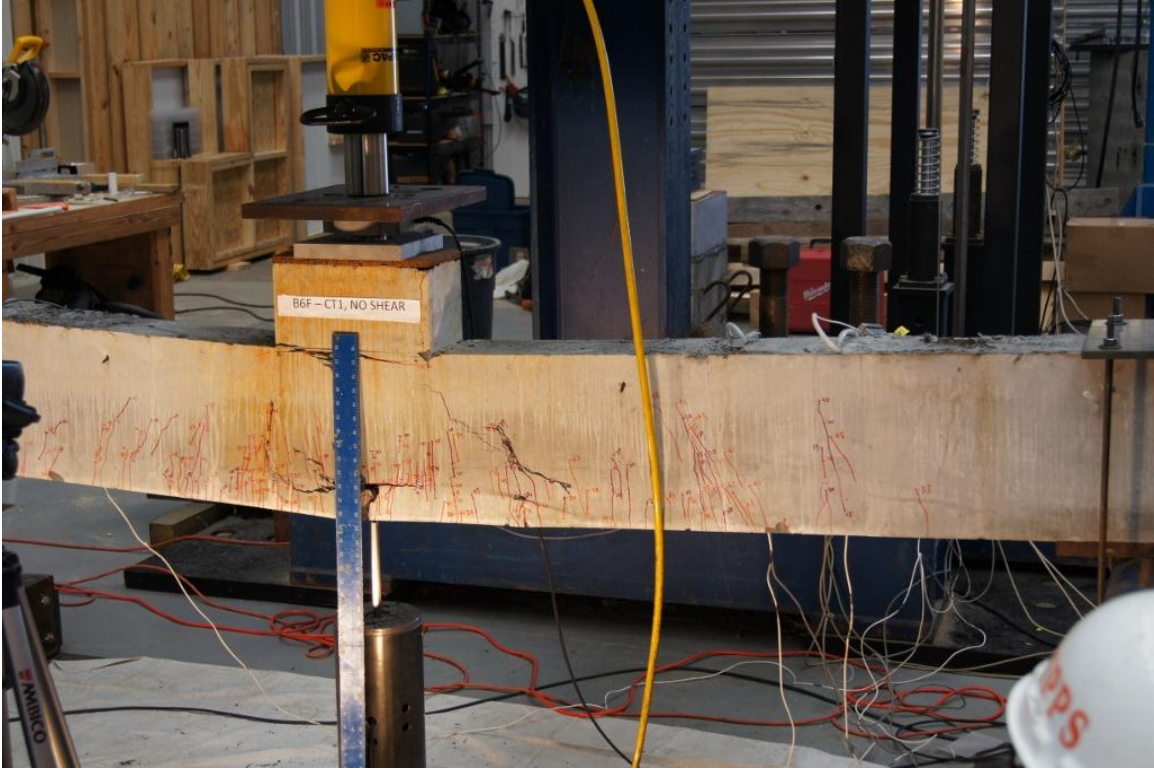


Figure 5-27. B6F loaded to 47 kips

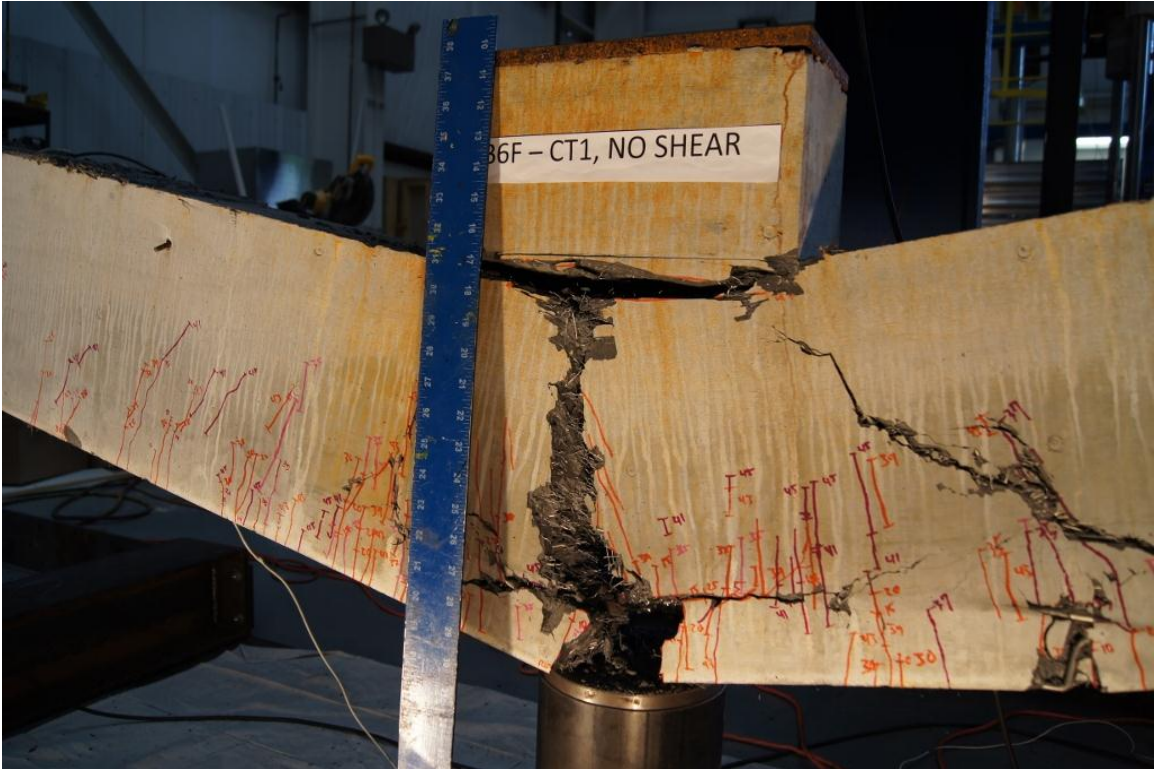


Figure 5-28. B6F failure, full tension failure

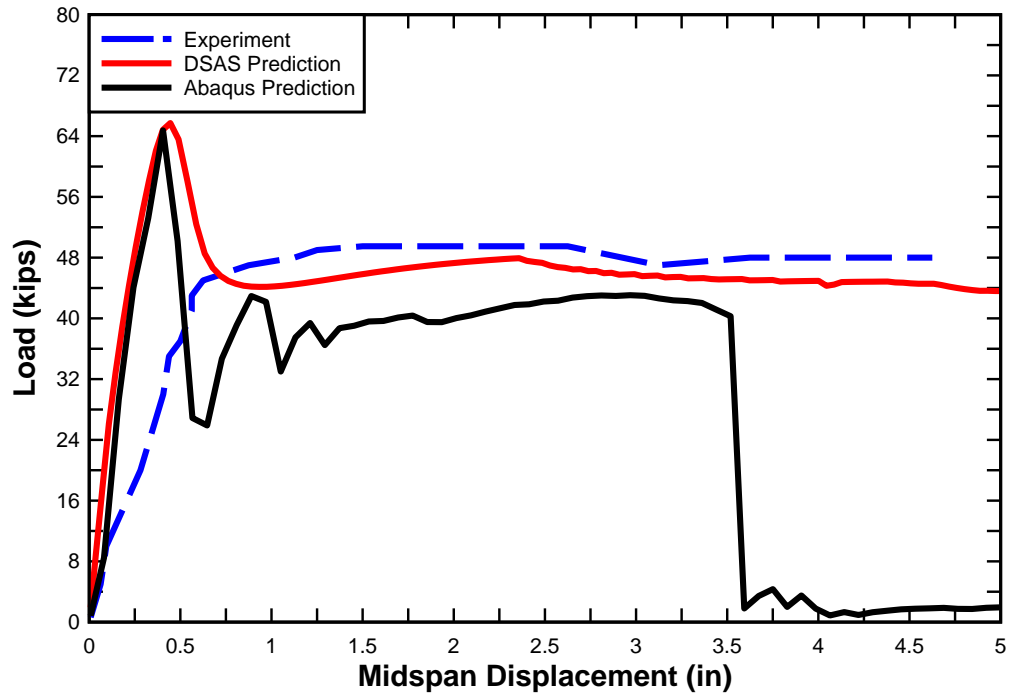


Figure 5-29. B6F Predictions vs. Experimental Results

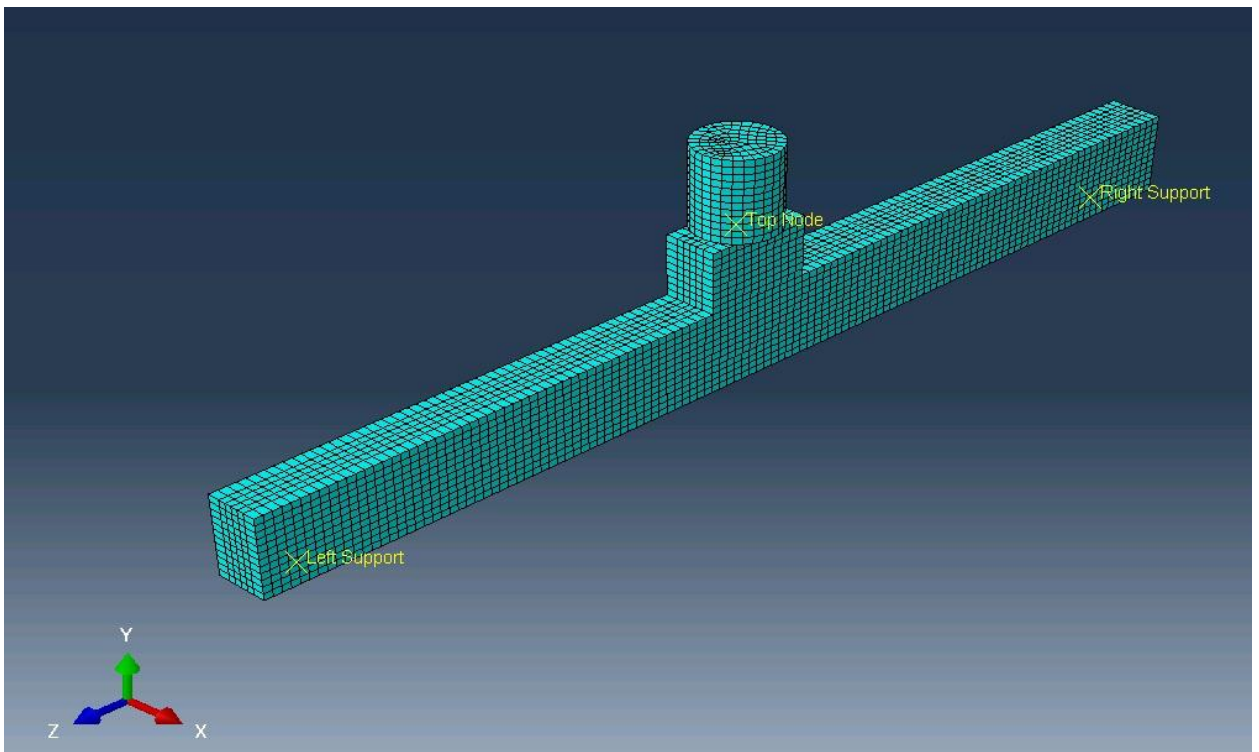


Figure 5-30. Dynamic beam representation in Abaqus

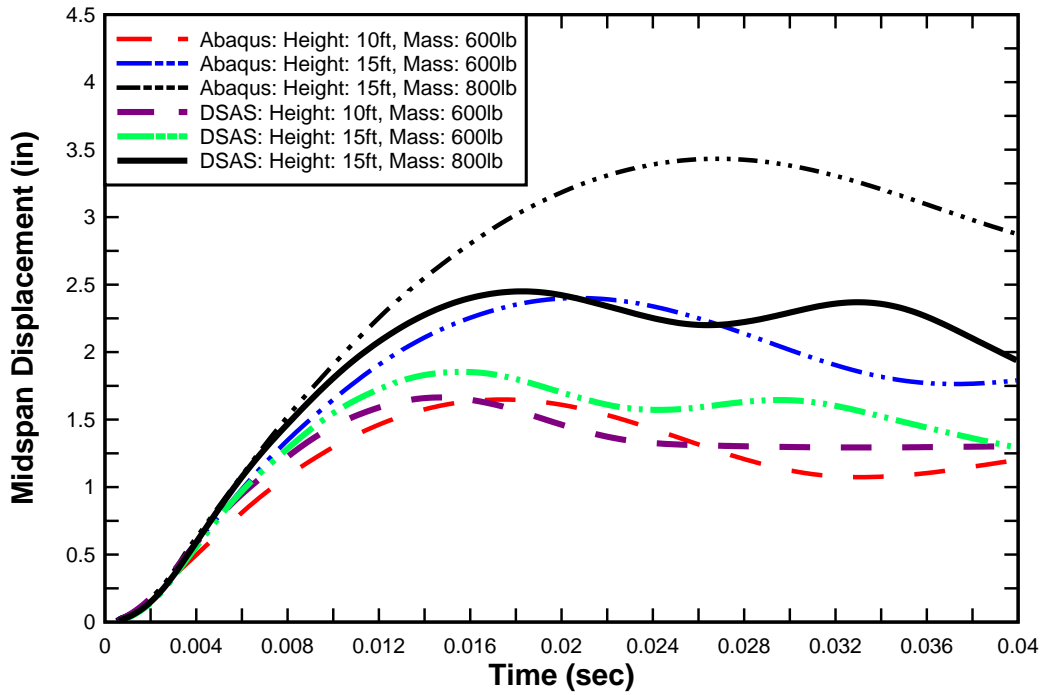


Figure 5-31. B1 Numerical impact midspan displacement vs. time results

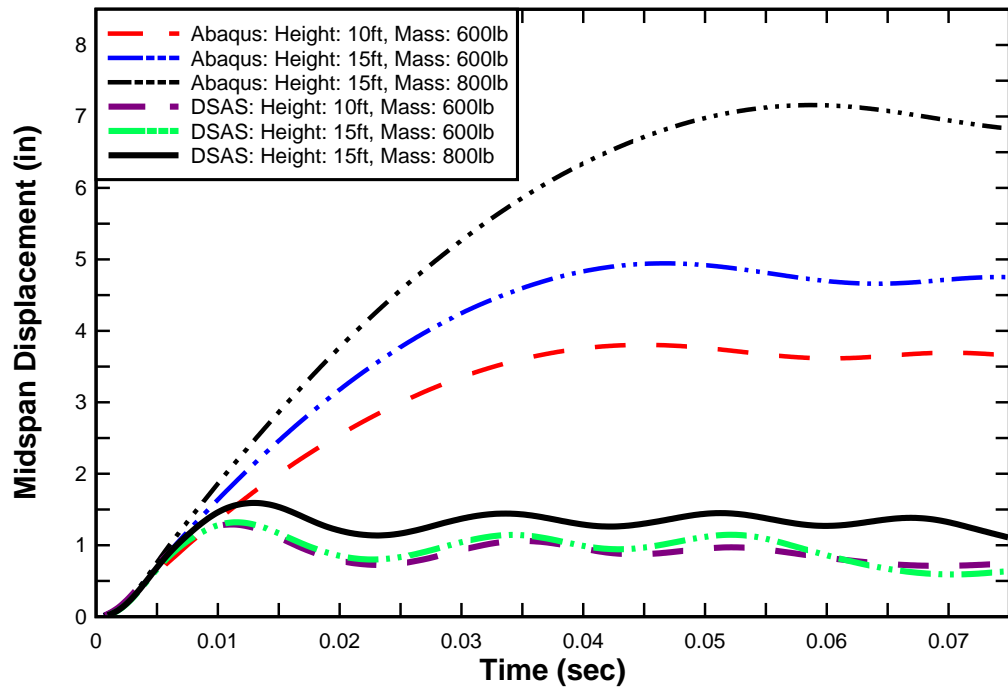


Figure 5-32. B2 Numerical impact midspan displacement vs. time results

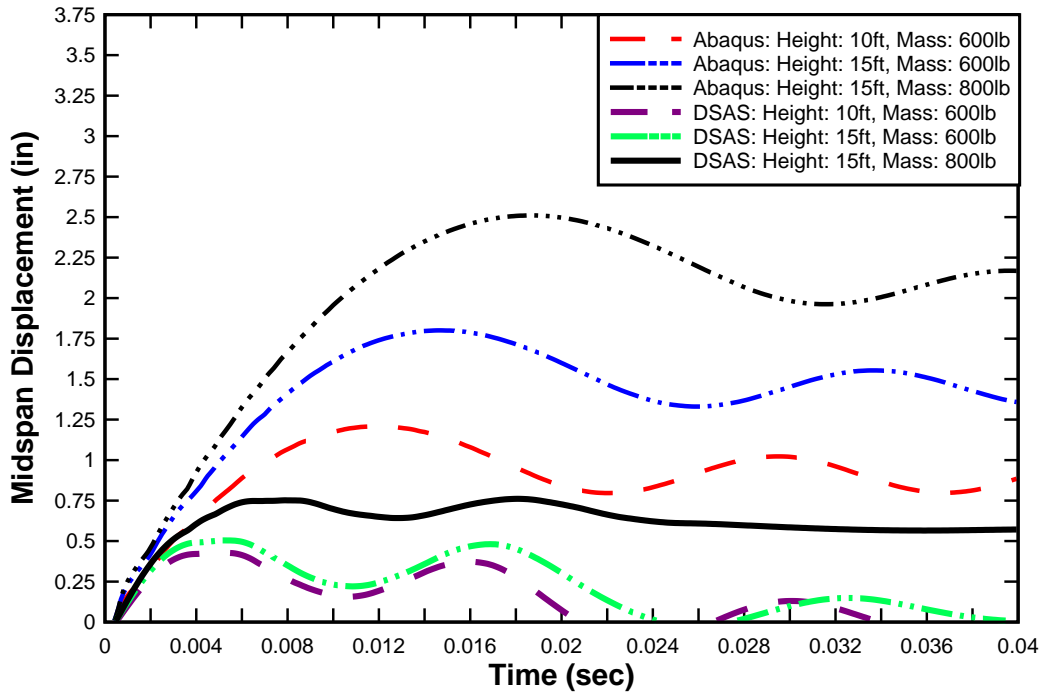


Figure 5-33. B3 Numerical impact midspan displacement vs. time results

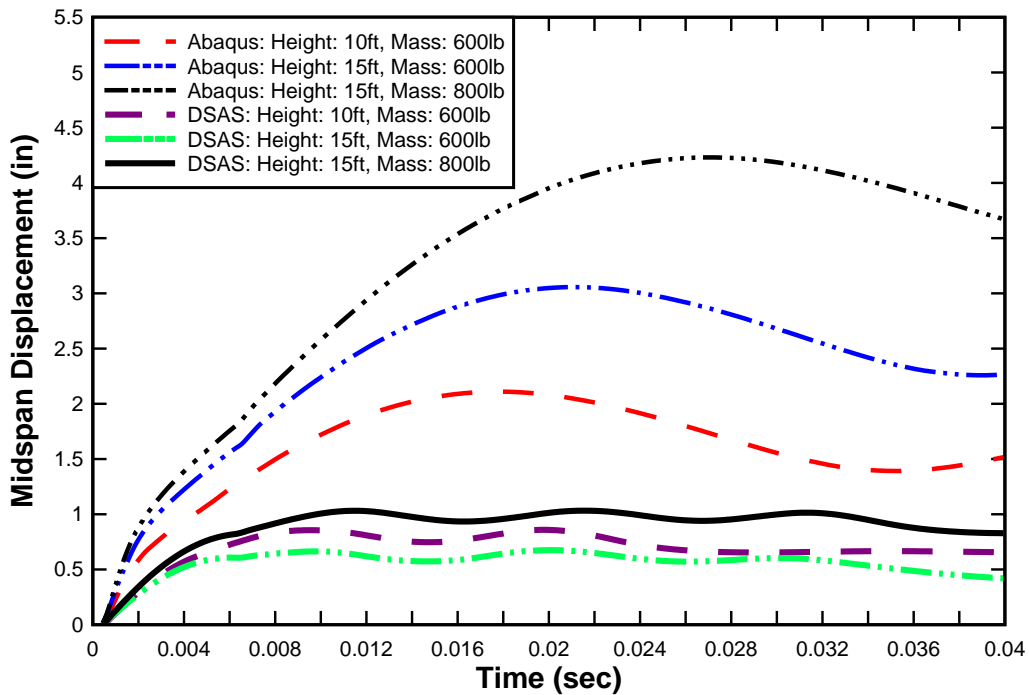


Figure 5-34. B4 Numerical impact midspan displacement vs. time results

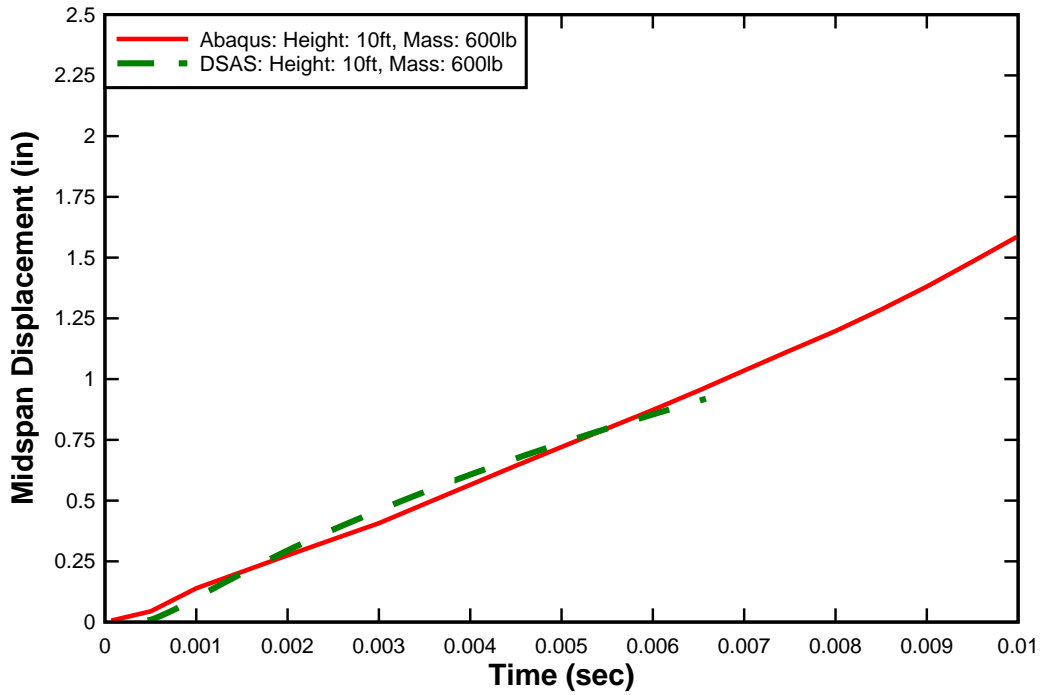


Figure 5-35. B5 Numerical impact midspan displacement vs. time results

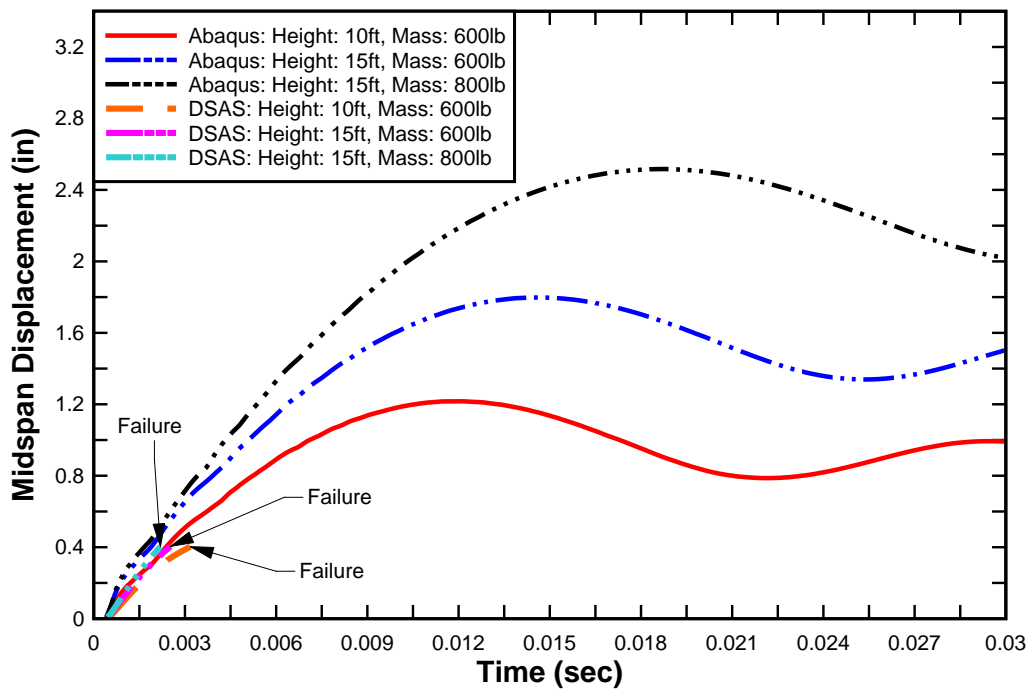


Figure 5-36. B6 Numerical impact midspan displacement vs. time results

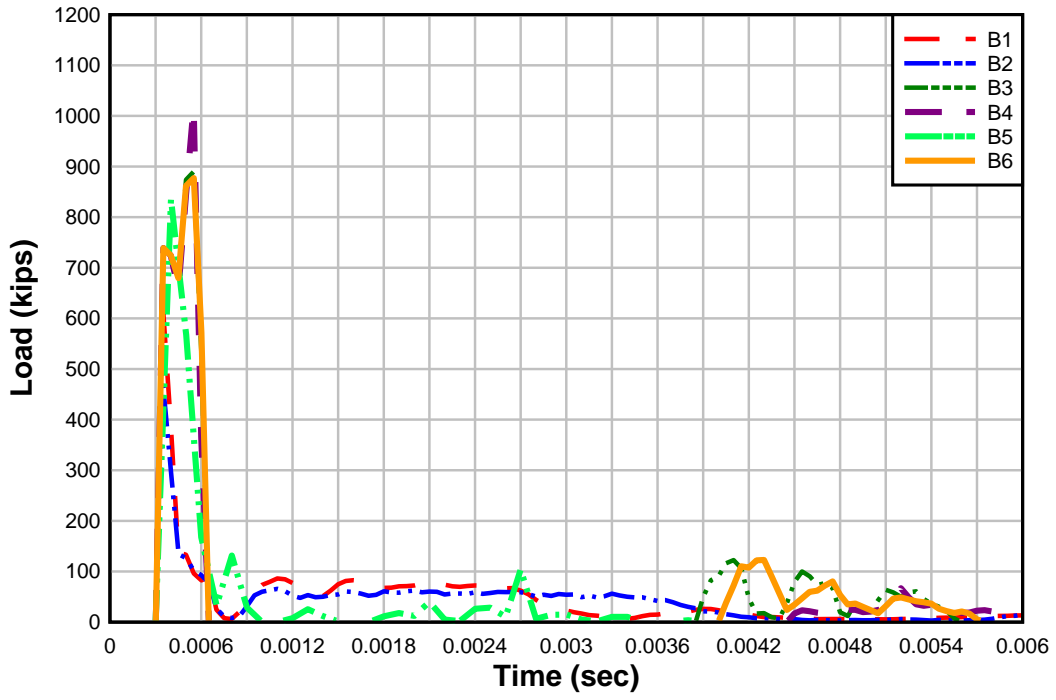


Figure 5-37. Load vs. time for hammer impact from 10 ft with 600 lbs

CHAPTER 6 CONCLUSIONS AND RECOMMENDATIONS

The work accomplished here is a start of the process that to properly characterize the full properties of Cor-Tuf as well as properly simulating impact experiments. The creation of validation models will allow for faster creation of trustworthy models in the future for reinforced concrete, and with the experiments to be performed, Cor-Tuf as well. The following are some conclusions that can be drawn from the work, followed by some recommendations of necessary future endeavors.

6.1 Model Validation

The model validation did a reasonable job of approximating the results of the Feldman and Siess experimental results. The Abaqus model did not require the higher dynamic increase factors that the DSAS models did. The DSAS models do not account for inertia in the same way that a finite element model does; therefore, the inherent inertia adds stiffness in the Abaqus models and likely accounted for the dynamic increase factors necessary in DSAS. Additionally, the static models of beam 1-f in Abaqus would improve significantly if they were run in Abaqus/Standard rather than Explicit.

6.2 Static Test Predictions

6.2.1 B1F

The reinforced concrete models for the static beam tests performed at CIPPS are fairly accurate for the B1 series. As with the validation models, the static cases would improve greatly when run in the Abaqus/Standard software package. DSAS provides reasonable predictions of the static results; however, the failure of the predictions occurs later than the experiment. This is likely due to the steel model being utilized that

will need some calibration once some coupon tests can be performed on the reinforcement being used for the tests.

6.2.2 B2A

In the case of ABAQUS, the concrete damage plasticity model utilized for the concrete material is not specifically designed for shear analyses. Therefore, the Abaqus model predicts higher stiffness from the beam than the actual test. The DSAS case over prediction could have occurred due to differences in the reported material properties utilized for the analysis and the actual material properties for the concrete and steel in the beam (this could also be taking place in the ABAQUS model as well). Additionally, it should be noted that these differences are more apparent due to the scale of the figure as most of the other cases had longer displacements.

6.2.3 B3F

The material model utilized for the numerical models was created based on the Ductal model that is linear-elastic, and then plastic. However, the full material curve for Cor-Tuf is as of yet unknown (although cylinder tests in near future should help with this issue) and therefore an approximation with Ductal was utilized due to their similar properties. It is assumed that once a proper characteristic curve for Cor-Tuf is created that the results of these models should be much closer to the experimental results. Also worth of noting is that in the ABAQUS model the concrete damage plasticity (CDP) model is utilized. This model was created and calibrated for normal strength concretes and is not designed for UHPC materials. However, since a proper UHPC model is still in the process of being created and finalized, the CDP model currently provides the best option for modeling UHPC. Additionally, the ABAQUS prediction drops below 0 for the load toward the end of the run. As explained in the B1F static test section, the

simulation is run over a shorter period of time than the actual test time which can cause fluctuations in the formulation of the load. The DSAS model utilized a similar model and remained relatively close to the Abaqus results.

6.2.4 B4F

The Abaqus and DSAS models for B4F both reasonably predicted the results of the static test. It is possible that this is a key to understanding the material model; the main difference between the Cor-Tuf 1 and Cor-Tuf2 models is the tension strength assigned to them and could therefore hint at a necessary change for the Cor-Tuf1 tension curve. However, it could also be a coincidence and will therefore need to be investigated further and is also why cylinder testing beyond peak strength will be vital to the continuing research.

6.2.5 B5F

Both Abaqus and DSAS predicted higher peak strengths for B5F but were much more accurate in their predictions for both yield deflection and final deflection for B5F. These results indicate that while the codes are accurate in their predictions of displacement, they are not accurate in predicting the flexural strength of the UHPC alone. As mentioned previously, these results will likely gain accuracy as the material model is refined. The B5F results could also be useful for understanding the tensile capacity of Cor-Tuf 1 as there is no influence from reinforcement.

6.2.6 B6F

The material model over predicted the peak load in Abaqus and DSAS. The Abaqus model collapsed before reaching 4 inches of deflection. While this was not entirely accurate, it showed that the Abaqus models are capable of simulating complete failure of the beam which will be useful later on.

6.3 Dynamic Test Predictions

Since the dynamic testing has not begun yet, the only conclusions that can be drawn are on the expected behavior of the beams and the comparison between Abaqus and DSAS results. The Abaqus models have already shown, as in the case of B2F, that the CDP model is not designed for cases of shear. Therefore, all of the Abaqus models must be considered with caution as loading of this magnitude likely cause shear failure in some of the specimen. Additionally, as was the case with B5C (impact of Cor-Tuf1 without reinforcement) the model itself does not fail; the beam remains plastic and deforms indefinitely.

The DSAS models, while using the load vs. time from Abaqus, appear to under predict the displacement of the beams when compared with Abaqus. These results also seem low when considering the magnitude of the load being applied, even if only for incredibly short durations. The loading curve provided for DSAS are highly incremented; however, they still require interpolation between any points provided. This could be creating a difference in the impulse that DSAS calculates and could affect the results. Another possibility is that DSAS ignores the stub which affects the plastic hinge length. This increased hinge length could be affecting the results of the DSAS runs.

6.4 Recommendations

The most important recommendation is proper material characteristic curves for Cor-Tuf1 and 2 in compression and tension. These curves must include the nonlinear portions of the curve all the way through crushing of the concrete and full cracking. The Abaqus and DSAS models need improved for UHPC materials. In the case of Abaqus, the AFC model may be required to properly model Cor-Tuf. Additionally, both Abaqus

and DSAS models need to be improved for shear modeling, especially Abaqus. In the case of Abaqus, a new material model might be necessary.

Additionally, the static beams showed that the Cor-Tuf beams are under reinforced. The B3F and B6F beams both failed in tension, and based on the results, had much more compression strength available. The tension reinforcement in these beams must be increased in order to utilize the full strength of Cor-Tuf and understand its true capabilities. As stated previously, these tests need to be backed up by other forms of other testing such as Split-Hopkinson Bar, slab testing and more impact testing with different beam designs.

LIST OF REFERENCES

- American Concrete Institute. (2011). *318-11: Building Code Requirements for Structural Concrete and Commentary*. ACI Committee 318, Detroit, MI.
- Association Française de Génie Civil. (AFGC). (2002). "Bétons fibrés à Ultra-hautes Performances (BFUP)- Recommandations provisoires (Ultra High Performance Fibre-Reinforced Concretes - Interim Recommendations)." France 98.
- Astarlioglu, S., and Krauthammer, Theodor. (2009). "Dynamic Structural Analysis Suite (DSAS)." University of Florida, Gainesville, FL.
- Bache, H. H. (1987). "Introduction to Compact Reinforced Composite." *Nordic Concrete Research*, (6), 19-33.
- Bathe, K. (1995). *Finite Element Procedures*. Prentice-Hall, Upper Saddle River, New Jersey.
- Bindiganavile, V., and Banthia, N. (2001a). "Polymer and Steel Fiber-Reinforced Cementitious Composites under Impact Loading — Part 1 : Bond-Slip Response." *ACI Materials Journal*, (98-M2), 10-16.
- Bindiganavile, V., and Banthia, N. (2001b). "Polymer and Steel Fiber-Reinforced Cementitious Composites under Impact Loading — Part 2 : Flexural Toughness." *ACI Materials Journal*, (98-M3), 17-24.
- Bindiganavile, V., Banthia, N., and Aarup, B. (2002). "Impact Response of Ultra-High-Strength Fiber-Reinforced Cement Composite." *ACI Materials Journal*, (99-M55), 543-548.
- Comite Euro-International Du Beton. (1993). *CEB-FIP Model Code 1990*. Thomas Telford Services Ltd., Lausanne, Switzerland.
- Cook, R., Malkus, D., Plesha, M., and Witt, R. (2002). *Concepts and Applications of Finite Element Analysis*. John Wiley and Sons, Inc., Hoboken, NJ.
- FHWA. (2006). *Structural Behavior of Ultra-High Performance Concrete Prestressed I-Girders*. McLean, VA.
- Fehling, E., Bunje, K., and Leutbecher, T. (2004). "Design relevant properties of hardened Ultra High Performance Concrete." *International Symposium on Ultra High Performance Concrete*, Kassel, Germany, 327-338.
- Feldman, A., and Siess, C. P. (1956). *Investigation of Resistance and Behavior of Reinforced Concrete Members Subjected to Dynamic Loading - Part I*. Urbana, Illinois.

- Feldman, A., and Siess, C. P. (1958). *Investigation of Resistance and Behavior of Reinforced Concrete Members Subjected to Dynamic Loading - Part II*. Urbana, Illinois.
- Fujikake, K., Senga, T., Ueda, N., Ohno, T., and Katagiri, M. (2006). "Study on Impact Response of Reactive Powder Concrete Beam and Its Analytical Model." *Journal of Advanced Concrete Technology*, 4(1), 99-108.
- Gowripalan, N., and Gilbert, I. R. (2000). *Design Guidelines for Ductal Prestressed Concrete Beams*. New South Wales.
- Graybeal, B. (2005). "Characterization of the Behavior of Ultra-High Performance Concrete." University of Maryland, College Park.
- Graybeal, BA. (2006). *Material Property Characterization of Ultra-High Performance Concrete*. McLean, VA.
- Habel, K. (2004). "ULTRA-HIGH PERFORMANCE FIBRE REINFORCED CONCRETES (UHPFRC) AND REINFORCED CONCRETE." ECOLE POLYTECHNIQUE FEDERALE DE LAUSANNE.
- Habel, K., and Gauvreau, P. (2008). "Response of ultra-high performance fiber reinforced concrete (UHPFRC) to impact and static loading." *Cement and Concrete Composites*, Elsevier Ltd, 30(10), 938-946.
- Habel, K., Viviani, M., Denarié, E., and Brühwiler, E. (2006). "Development of the mechanical properties of an Ultra-High Performance Fiber Reinforced Concrete (UHPFRC)." *Cement and Concrete Research*, 36(7), 1362-1370.
- Hsu, T. T. (1993). *Unified Theory of Reinforced Concrete*. CRC Press.
- Kang, S., Lee, Y., Park, Y., and Kim, J. (2010). "Tensile fracture properties of an Ultra High Performance Fiber Reinforced Concrete (UHPFRC) with steel fiber." *Composite Structures*, Elsevier Ltd, 92(1), 61-71.
- Koh, Y. (2011). "Characterizing a Reinforced Concrete Beam-Column-Slab Subassemblage Connection for Progressive Collapse Assessment." University of Florida.
- Krauthammer, Theodor. (2008). *Modern Protective Structures*. CRC Press, Boca Raton, FL.
- Krauthammer, Theodor, and Shahriar, S. (1988). *A Computational Method for Evaluating Modular Prefabricated Structural Element for Rapid Construction of Facilities, Barriers, and Revetments to Resist Modern Conventional Weapons Effects*. Minneapolis, MN.

- MacGregor, J. G., and Wight, J. K. (2005). *Reinforced Concrete: Mechanics and Design*. Prentice-Hall.
- Mazloom, M., Ramezani-pour, a. a., and Brooks, J. J. (2004). "Effect of silica fume on mechanical properties of high-strength concrete." *Cement and Concrete Composites*, 26(4), 347-357.
- Millard, S. G., Molyneaux, T. C. K., Barnett, S. J., and Gao, X. (2010). "Dynamic enhancement of blast-resistant ultra high performance fibre-reinforced concrete under flexural and shear loading." *International Journal of Impact Engineering*, Elsevier Ltd, 37(4), 405-413.
- Morin, V., Cohen Tenoudji, F., Feylessoufi, a., and Richard, P. (2001). "Superplasticizer effects on setting and structuration mechanisms of ultrahigh-performance concrete." *Cement and Concrete Research*, 31(1), 63-71.
- Ngo, T., Mendis, P., and Krauthammer, Ted. (2007). "Behavior of Ultrahigh-Strength Prestressed Concrete Panels Subjected to Blast Loading." *Journal of Structural Engineering*, ASCE, (November), 1582-1590.
- Parant, E., Rossi, P., Jacquelin, E., and Boulay, C. (2007). "Strain Rate Effect on Bending Behavior of New Ultra-High- Performance Cement-Based Composite." *ACI Materials Journal*, (104-M50), 458-463.
- Park, R., and Paulay, T. (1975). *Reinforced Concrete Structures*. John Wiley and Sons, Inc., New York, 195-269.
- Peters, S. J. (2009). "Fracture toughness investigations of micro and nano cellulose fiber reinforced ultra high performance concrete." The University of Maine.
- Rong, Z., Sun, W., and Zhang, Y. (2010). "Dynamic compression behavior of ultra-high performance cement based composites." *International Journal of Impact Engineering*, Elsevier Ltd, 37(5), 515-520.
- Ross, C. A., Kuennen, S. T., and Strickland, W. S. (1989). "High Strain Rate Effects on Tensile Strength of Concrete." *Proceedings of 4th International Symposium on the Interaction of Non-Nuclear Munitions with Structures*, University of Florida Graduate Engineering Center, Eglin AFB, FL.
- Rossi, P., Arca, A., Parant, E., and Fakhri, P. (2005). "Bending and compressive behaviours of a new cement composite." *Cement and Concrete Research*, 35(1), 27-33.
- Semioli, W. J. (2001). "The New Concrete Technology." *Concrete International*, (November), 75-79.

- Simulia. (2011). "Abaqus FEA." Prentice-Hall, Vélizy-Villacoublay, France.
- Soroushian, P., and Obaseki, K. (1986). "Strain Rate-Dependent Interaction Diagrams for Reinforced Concrete Section." *American Concrete Institute Journal*, 8(63).
- Tang, M. (2004). "High Performance Concrete - Past, Present and Future." *International Symposium on Ultra High Performance Concrete*, Kassel, Germany, 3-9.
- Williams, E. M., Graham, S. S., Reed, P. A., and Rushing, T. S. (2009). *Concrete With and Without Steel Fibers Geotechnical and Structures Laboratory Concrete With and Without Steel Fibers*. Vicksburg, MS.
- Wu, C., Oehlers, D. J., Reberntrost, M., Leach, J., and Whittaker, a. S. (2009). "Blast testing of ultra-high performance fibre and FRP-retrofitted concrete slabs." *Engineering Structures*, Elsevier Ltd, 31(9), 2060-2069.
- Yudenfreud, M., Odler, I., and Brunauer, S. (1972). "Hardened Portland Cement Pastes of Low Porosity." *Cement and Concrete Research*, 2(3), 313-330.
- Zineddin, M. (2002). "Behavior of Structural Concrete Slabs Under Localized Impact." The Pennsylvania State University.

BIOGRAPHICAL SKETCH

Daniel Koch was born in 1985 in Vero Beach, Florida. After attending Vero Beach High School, he moved to Vermont and pursued his Bachelor of Science in civil engineering from the University of Vermont. Upon graduating in 2007, he spent a year working, studying and traveling in Israel, Europe and Asia.

He began graduate school at the University of Florida in 2008 as a non-thesis structural engineering student. In 2010, he began working on this thesis after receiving sponsorship from the Center for Infrastructure Protection and Physical Security (CIPPS) through the Defense Threat Reduction Agency. He received his M.E. from the University of Florida in the summer of 2012, with a certificate in Security Engineering from CIPPS.